Wetting and Phase-Change Phenomena on Micro/Nanostructures for Enhanced Heat Transfer

by

Rong Xiao

SUBMITTED TO THE DEPARTMENT OF MECHANICAL ENGINEERING IN PARTIAL FULFILLMENT OF THE REQUIREMENTS FOR THE DEGREE OF

Ph.D. in Mechanical Engineering
AT THE
MASSACHUSETTS INSTITUTE OF TECHNOLOGY

January 2013
[FEBRUARY 2013]

Signature of Author:_____
Department of Mechanical Engineering
January 15, 2013

Certified by:_____
Evelyn N. Wang
Associate Professor of Mechanical Engineering
Thesis Supervisor

Accepted by:_____
David Hardt
Professor of Mechanical Engineering
Chairman, Graduate Thesis Committee

To My Dear Parents

And

Dear Jing

Wetting and Phase-Change Phenomena on Micro/Nanostructures for Enhanced Heat Transfer

By

Rong Xiao

Submitted to the Department of Mechanical Engineering
On Jan. 15th, 2013 in partial fulfillment of the
Requirements for the Degree of Ph.D. in
Mechanical Engineering

Abstract

Micro/nanostructures have been extensively studied to amplify the intrinsic wettability of materials to create superhydrophilic or superhydrophobic surfaces. Such extreme wetting properties can influence the heat transfer performance during phase-change which is of great importance in a wide range of applications including thermal management, building environment, water harvesting and power production. In particular, superhydrophilic surfaces have been of interest to achieve thin film evaporation with high heat fluxes. Meanwhile, superhydrophobic surfaces with dropwise condensation promises higher heat transfer coefficients than typical filmwise condensation. My thesis work aims at improving fundamental understanding as well as demonstrating practical enhancements in these two areas.

A key challenge to realizing thin film evaporation is the ability to achieve efficient fluid transport using superhydrophilic surfaces. Accordingly, we developed a semi-analytical model based on the balance between capillary pressure and viscous resistance to predict the propagation rates in micropillar arrays with high aspect ratios. Our experimental results showed good agreement with the model, and design guidelines for optimal propagation rates were proposed. For micropillar arrays with low aspect ratio and large spacing between pillars, however, we identified that the microscopic sweeping of the liquid front becomes important. We studied this phenomenon, explained the effect of such microscale dynamics on the overall propagation behavior, and proposed a strategy to account for these dynamics.

While these propagation studies provide a means to deliver liquid to high heat flux regions, we investigated a different configuration using nanoporous membrane that decouples capillarity from the viscous resistance to demonstrate the potential heat dissipation capability. With nanoporous membranes with average pore diameters of 150 nm and thicknesses of 50 μm, we achieved interfacial heat fluxes as high as 96 W/cm^2 *via* evaporation with isopropyl alcohol. The

effect of membrane thickness was studied to offer designs that promise dissipation of 1000 W/cm^2. Meanwhile, we developed new metrology to measure transient heat transfer coefficients with a temporal resolution of 0.2 seconds during the evaporation process. Such a technique offers insight into the relationship between liquid morphology and heat transfer behavior.

Finally, for enhanced condensation, we demonstrated immersion condensation using a composite surface fabricated by infusing hydrophobic oil into micro/nanostructures with a heterogeneous coating. With this approach, three key attributes to maximize heat transfer coefficient, low departure radii, low contact angle, and high nucleation density, were achieved simultaneously. We specifically elucidated the mechanism for the increase in nucleation density and attribute it to the combined effect of reduced water-oil interfacial energy and local high surface energy sites. As a result, we demonstrated approximately 100% enhancement in heat transfer coefficient over state-of-the-art superhydrophobic surfaces with the presence of non-condensable gases.

This thesis presents improved fundamental understanding of wetting, evaporation, and condensation processes on micro/nanostructures as well as practical implementation of these structures for enhanced heat transfer. The insights gained demonstrate the potential of new nanostructure engineering approaches to improve the performance of various thermal management and energy production applications.

Thesis Committee Chair:

Prof. Evelyn N. Wang, Department of Mechanical Engineering, MIT

Thesis Committee Members:

Prof. Bora Mikic, Department of Mechanical Engineering, MIT
Prof. Jacopo Boungiorno, Department of Nuclear Engineering, MIT

Acknowledgement

I sincerely thank my advisor, Prof. Evelyn N. Wang, for her dedicated mentoring during my master and Ph.D. studies. Most my achievements during the past five years, if any, would not be possible without her guidance. Her vision, devotion to work, and enthusiasm to research have set an inspiring example for me. The lessons I learnt from her not only benefited me for my studies at MIT, but also would lead me for future career development.

I would also like to thank my committee members, Prof. Bora Mikic and Prof. Jacopo Buongiorno. Their insightful comments and guidance greatly improved the quality of my thesis and deepened my understanding of phase-change heat transfer.

During my studies, I have received significant help from my labmates at the Device Research Laboratory. I want to thank all of them, especially my buddy, Kuang-Han "Hank" Chu, who is also one of the earliest members of the group. We helped out each other during the tough early days in brotherhood.

I was also lucky enough to make many good friends at MIT. Their warm friendship is gratefully cherished.

Finally, I want to dedicate my special thanks to my family. My parents have supported me through all the years and I would not achieve anything without their support. I hope they can be proud of me. I also thank my loved Jing for the love, joy and happiness she brought to me during my final time at MIT.

Table of Contents

Chapter 1 Introduction and Literature Review

1.1 Wetting Phenomena on Micro/Nanostructures

Micro/nanostructures have long been recognized as able to magnify the intrinsic wetting properties to achieve superhydrophilic or superhydrophobic surfaces in combination with chemical modifications where static contact angle as from 0° to over 160° have been demonstrated [1-3]. Extensive efforts have been devoted to such surfaces to control the dynamic behavior of fluids. For example, on superhydrophilic surfaces, recent investigations have achieved anisotropic or uni-directional spreading where liquid prefers to spread in certain directions [4, 5]. Control of the liquid layer thickness during spreading has also been realized [6]. Meanwhile, on the superhydrophobic aspect, more recent studies have demonstrated using re-entrant micro features to achieve omniphobic surfaces which are resistant to even low surface tension liquids [7, 8]. These capabilities have great potential in a wide range of applications including DNA microarrays, digital lab-on-a-chip, anti-fogging and fog-harvesting, inkjet printing and drag-reduction [9-15].

In addition to the rich opportunity in modulating fluid dynamics, superhydrophilicity and superhydrophobicity can also influence the heat transfer performance of phase change processes, which is important in applications involving energy transport such as thermal management and power generation. In particular, superhydrophilic surfaces have been explored to achieve thin film evaporation with high heat fluxes [16-19]. Meanwhile, superhydrophobic surfaces have demonstrated dropwise condensation with higher heat transfer coefficient compared to typical filmwise condensation [20-25]. This thesis will aim at improving the fundamental understanding as well as demonstrating practical enhancement for these two areas.

1.2 Phase-Change Phenomena for Thermal Management of Electronic Devices

With the growing power consumption and decreasing size of modern integrated circuits (ICs), thermal management has become a significant bottleneck. For example, as shown in Figure 1-1 (adapted from [26]), as the heat flux of Central Processing Unit (CPU) increased to 100 W/cm^2, typical commercialized thermal management approaches were not able to dissipate such high fluxes and the industry has to adopt novel designs such as "multi-core" to reduce the heat flux. However, based on the prediction of the International Technology Roadmap for Semiconductors (ITRS), the heat flux for the next generation of ICs will be over 100 W/cm^2 by 2015 [27]. Meanwhile, more aggressive predictions expect heat fluxes on the order of 300~1000 W/cm^2 in the next few years [28, 29]. The need for thermal management schemes capable of dissipating such high heat fluxes with low temperature rises (~85 °C) has been well recognized.

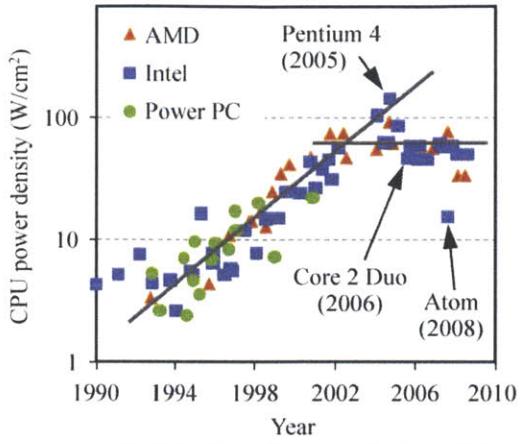

Figure 1-1. Recent trend in power density of CPUs. Heat fluxes as high as 100 W/cm^2 has been a major bottleneck for increasing integration level. (Adapted from [26])

Phase-change based cooling techniques, which utilize the large latent heat of evaporation, are considered as one of the most promising method to address those thermal management needs. A variety of phase change based approaches have been studied extensively, including pool boiling, flow boiling in microchannels, jet impingement and spray cooling.

Pool boiling is considered one of the simplest methods to achieve heat fluxes over 100 W/cm^2 as a passive method which doesn't require extra power input. However, the maximum heat transfer rate of pool boiling is limited by the critical heat flux (CHF), above which the transition from nucleate boiling to film boiling occurs, leading to a significant rise in thermal resistance or even burnout. A variety of models have been proposed to predict the CHF limit, such as Dhir and Liaw's model based on capillary pumping [30], Liter and Kaviany's model based on viscous drag [31], and Kandlikar's model based on the expansion dynamics of vapor bubble [32].While the detailed mechanism for CHF is still under investigation and debate, extensive work has focused on enhancing the CHF using micro/nanostructured superhydrophilic surfaces. CHF above 200 W/cm^2 has been reported on surfaces modified with micropillar arrays, nanowires, and porous nanoparticle coatings [33-36]. However, pool boiling usually has high working temperature and is sensitive to orientation, which limits the application in thermal management for electronic devices. Moreover, the heat transfer performance of pool boiling is dependent on the orientation of the heating surface relative to gravitational field, which also limits the practical application.

Flow boiling in channels has demonstrated promising potential for high flux cooling. Due to the large surface to volume ratio, flow boiling in microchannels has demonstrated thermal resistances as low as 0.1 K/W which is advantageous over its macroscale counterpart. However, microchannel boiling suffers from several challenges. In macrochannels, vapor bubbles are removed by inertia and buoyancy forces, which are insignificant at the microscale. As a result, the vapor bubbles tend to remain in the channel and expand to vapor slugs very rapidly, which

lead to local dry-out, non-uniform temperature distribution and flow instabilities or even flow reversal. With constrictors at the entrance of the channel to stabilize the flow, Kosar *et al.* achieved heat flux as high as 614 W/cm^2 by water flow boiling in microchannels [37]. While such constrictors are able to reduce the oscillation and flow reversal, the flow instabilities cannot be completely avoided.

In jet impingement cooling system, high-velocity jets from nozzles impinge on the hot surface and form a thin liquid layer under the jet. Previous work showed that the jet velocity and sub-cooling of the liquid have a pronounced effect on the heat flux [38]. Wang *et al.* achieved heat fluxes of 90 W/cm^2 with a temperature rise of 100 °C [39]. However, jet impingement schemes are difficult to implement, where only the local impingement region experiences high heat removal rates, and the flooding of the chambers lead to pool boiling which limits the cooling performance. Similar to jet impingement, spray cooling utilizes liquid droplets to impinge on the hot surface and form a very thin liquid layer. The evaporation of the thin layer removes a large amount of heat. Lin and Ponnappan reported a maximum heat flux of 500 W/cm^2 with water spray from eight nozzles [40]. However, ultra high pressure (hundreds of kPa) is required to create spray flow, which are typically not allowed in commercial packages. Researchers have also proposed using piezoelectric vibrators or inkjet printer technology to create sprays [41]. In addition to the ultra high pressure and power needed, another concern about spray cooling is the intricate flow patterns. Hall and Mudawar reported that identical spray nozzles from the same production batch failed to create identical spray flows [42].

Recent fundamental studies [16, 17] have suggested that evaporation in the thin film region, where liquid film thickness is on the order of 1 μm, is the key component in evaporative heat transfer approaches. Park et al. calculated that the maximum heat transfer coefficient at the thin film region in the meniscus can be as high as 100 MW/m^{2}K [43]. Similarly, Stephan and Busse carried out numerical simulations to show that the local heat flux at the thin film region in grooves can be over 5000 W/cm^2 [44]. However, on a flat surface, the area of thin film region is usually small (< 10% of total surface area) and therefore the total heat flux is limited.

1.3 Micro/Nanostructures for Thin Film Evaporation

Micro/nanostructures serve for two purposes in thin film evaporation. First, the micro/nanostructures could significantly increase the contact area so that the thin film region can be expanded. Second, hydrophilic micro/nanostructures could generate large capillary pressure to enhance liquid transport, where the micro/nanostructures are termed "wicks" conventionally for the ability of wicking fluids.

A wide variety of micro/nanostructures has been investigated for thin film evaporation such as grooves [45], metal meshes [46], sintered metal meshes with carbon nanotubes (CNTs) [47],

titanium nanopillars [48], and oxidized copper microposts [49]. Kim, Weibel and Garimella used sintered copper mesh coated with carbon nanotube as the wick structure in a vapor chamber and achieved maximum heat flux of 550 W/cm^2 and thermal resistance of 0.26 K/W [50]. Ding et al. used titanium nanopillars with titania coating as wick structure in a flat heat pipe to achieve effective thermal conductivity of 350 W/mK. The thermal resistance was 2.69 K/W under heat flux of 7.2 W/cm^2. In this work, the heat transfer was along the thickness direction of the plane, which contributes to higher thermal resistance [49]. Nam *et al.* demonstrated maximum heat flux over 200 W/cm^2 using evaporation from oxidized copper microposts as wick structures with heat transfer coefficient over 10 W/cm^{2}K [49].

In such systems, the rate of liquid transport plays a fundamental role in determining the heat transfer performance. Efforts have been devoted to enhance the liquid supply by introducing liquid supply arteries or bi-porosity in the design of the wicks. For example, Hwang *et al.* used sintered copper as wick structure with mini-arteries to enhance liquid supply in a flat vapor chamber to achieve maximum heat flux of 380 W/cm^2 with thermal resistance of 0.05 K/W [51]. Using silicon bi-porous wicks, Coso *et al.* achieved maximum heat flux of 277 W/cm^2 with heat transfer coefficient of 19.6 W/cm^{2}K in a mixed mode of boiling and evaporation. With evaporation dominant mode, the maximum heat flux was 119.6 W/cm^2 with heat transfer coefficient of 20.7 W/cm^{2}K [19]. Cai and Chen used carbon nanotube bi-porous wicks to achieve maximum heat flux of 600 W/cm^2 and heat transfer coefficient of 21 W/cm^{2}K [52]. These efforts, though effective in enhancing heat transfer performance, are mostly experience-based and qualitative without quantitative understanding of the dynamics of liquid propagation in microstructures. Further optimization in the design of the wicks is limited.

1.4 Condensation Heat Transfer Enhancement using Engineered Surfaces

Condensation is an essential process in a wide variety of industrial applications including building environment [53], power generation [54], and water harvesting systems [55]. Enhancing condensation heat transfer has the potential to significantly improve the efficiency and reduce the cost of these applications. In practice, filmwise condensation, where a thin liquid film covers the surface, is the most prevalent condensation mode due to the high wettability of common heat transfer materials. However, the heat transfer coefficient is limited by the thermal resistance associated with the condensate film which insulates the surface. Accordingly, efforts spanning over eight decades have been devoted to achieving dropwise condensation on non-wetting surfaces where shedding droplets clean the surface for re-nucleation, leading to enhanced heat transfer rates [21-25, 56-59]. One order of magnitude higher heat transfer coefficients compared to filmwise condensation have been reported using dropwise condensation [21, 25]. Recent investigations have focused on creating chemically modified micro/nanostructured surfaces to achieve superhydrophobicity with the aim to further reduce the departure radii of droplets [58-60]. However, this focus on increasing the apparent hydrophobicity is not sufficient to achieve

maximized condensation heat transfer rates. The high apparent contact angles of condensing droplets on superhydrophobic surfaces lead to an increase in the conduction resistance through the droplet, hindering the overall heat transfer performance [61]. Moreover, the hydrophobic surface chemistry increases the nucleation thermodynamic energy barrier, thus reducing the nucleation density and limiting the heat transfer coefficient. More recently, a composite surface has been proposed whereby a hydrophobic structured surface is infused with oil to simultaneously achieve easy droplet removal and low contact angles [62, 63]. While these works demonstrated significant potential for enhanced condensation surfaces, high nucleation densities are also desired along with these attributes for optimal heat transfer performance.

1.5 Scope and Content of the thesis

In Chapter 2 of this thesis, the dynamics of liquid spreading in micropillar arrays will be investigated and a predictive model of liquid propagation rate dependent on micropillar geometries will be presented. The model is based on the Washburn approach by balancing the capillary pressure and the viscous resistance. The effect of liquid meniscus will be incorporated by Surface Evolver (SE) simulations. Experiments were carried out to validate the model and design guidelines are proposed to achieve optimized design of wick structures within given geometry range where the pillars are not too short (height of pillars is not smaller than period of the array). In short and very sparse pillar arrays, the microscopic sweeping of liquid front between pillars becomes significant and such behavior will be studied in detail in Chapter 3. The effect of such microscopic sweeping on macroscale propagation rate will be quantified and validated with experiments.

The improved knowledge on the liquid propagation behavior revealed that an upper bound of heat dissipation exists due to the coupling of viscous resistance and capillary pressure. In order to overcome such limit, nanoporous membranes will be proposed as an alternative configuration to de-couple capillary pressure and viscous resistance in Chapter 4. Actual heat transfer performance will be examined using isopropyl alcohol (IPA) as a testing fluid. Future directions for heat fluxes over $1000 W/cm^2$ will be proposed based on proof of concept experimental results.

In Chapter 5, a new metrology approach, which is capable of measuring transient heat transfer coefficient with temporal resolution as good as 0.2 seconds, will be proposed and implemented. This approach utilizes short pulses to heat the sample and determines the instantaneous heat transfer coefficient using the transient response. Two sample systems, copper microwire and nanoporous membranes were tested to demonstrate the correlation between wetting morphology and heat transfer coefficient.

In Chapter 6, a new approach is presented to enhance condensation heat transfer using an oil-infused structured surface with heterogeneous surface chemistry. A heterogeneous coating

consisting of scattered high-surface-energy sites on a low-surface-energy background was deposited on micro/nanostructured surfaces. The surfaces were then infused with oil, which is stabilized by the surface structuring. During condensation, nucleation occurred on the high-surface-energy sites immersed within the oil phase, but near the oil/vapor interface. In contrast to the same surface not infused with oil, we demonstrated nucleation densities were one order of magnitude larger due to the combined effect of the high-surface-energy sites and the reduced oil-water interfacial energy which lower the thermodynamic energy barrier for stable nuclei formation. Furthermore, the contact angle hysteresis was as low as 3° and the droplet apparent contact angle was ≈110°. This immersion condensation mode allows near-ideal condensation heat transfer performance. Accordingly, we experimentally demonstrated that the heat transfer coefficient can be enhanced by over 100% compared to a dropwise condensation surface in the presence of non-condensable gases (NCG). Thus, these surfaces promise the development of a scalable approach for highly efficient heat transfer for industrial, building energy, electronics cooling, and water-harvesting applications.

Chapter 2 Liquid Propagation in Micropillar Arrays

2.1 Overview

As discussed in Chapter 1, liquid propagation in superhydrophilic micropillar arrays has received significant interest due to rich interfacial phenomena as well as broad applications in microfluidics for thermal management systems. However, utilization of such phenomena in practical systems requires detailed understanding of the complex liquid-solid interactions that determines the wetting and transport behavior. The first step is to obtain quantitative understanding of liquid dynamics on uniformly spaced micropillar arrays. In particular, the prediction and optimization of propagation rates will facilitate the design of high performance wick structures for thin film evaporation. Washburn first proposed a model to predict liquid propagation rates in capillary tubes that balances capillary pressure with viscous resistance [64]. Such a model has subsequently been adapted to micro/nanopillar arrays where the key challenges are quantifying the capillary pressure and viscous resistance. Recently, Nam *et al.* simulated the meniscus shape on hexagonal pillar arrays using Surface Evolver (SE) to predict the capillary pressure [65]. Hasimoto approximated the viscous resistance of pillar arrays by idealizing them as infinitely long cylinders [66]. Sangani and Acrivos studied the flow in planar (2-dimensional) circular pillar arrays using numerical method and determined the permeability of such planar arrays [67]. Srivastava *et al.* provided scaling analysis and performed finite element simulations to obtain the viscous resistance in micropillar arrays [68]. In addition, Ishino *et al.* also carried out scaling analysis and determined that the viscous resistance may be dominated by either the bottom surface or the pillars, depending on the pillar height compared to the period of the array [69]. While these studies have used various methods to quantify the capillary pressure and viscous resistance in micropillar arrays, a predictive model for both capillarity and viscous resistance is needed.

In this chapter, a semi-analytical model was developed to predict liquid propagation rates based on the diameter, height, and period of the micropillar arrays. The model follows the Washburn approach by balancing the capillary pressure and viscous resistance. First, the actual meniscus shape is studied to determine the driving capillary pressure for pillar arrays with a height-to-period ratio greater than 1. The viscous resistance was obtained by solving Brinkman's equation [70] for pillar arrays with a diameter-to-period ratio less than 0.57. Experiments were performed on various microfabricated silicon pillars to validate the developed model within the defined geometric range, which is most useful for large propagation rates.

2.2 Fabrication of Micropillar Arrays

The micropillars arrays used in the study ranged in diameters from 2 μm to 8 μm and period (center-to-center distance) from 8 μm to 15 μm, and were fabricated by contact lithography and deep reactive ion etching (DRIE). The fabrication process is shown in Fig. 2-1.

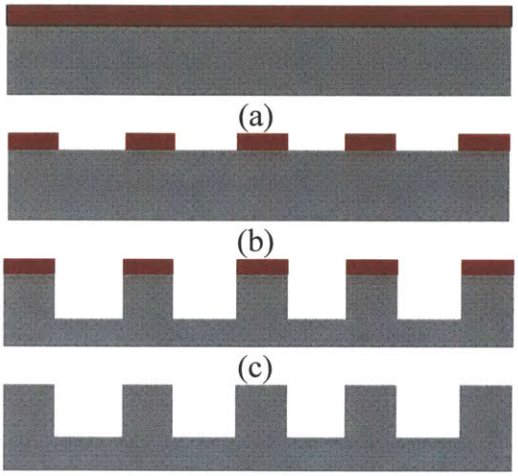

Fig. 2-1 The fabrication process of nanopillars. (a) Silicon wafer coated with photoresist. (b) Coated wafer exposed and developed to reveal the feature. (c) Silicon wafer etched to desired depth. (d) Photoresist was stripped to finish the fabrication.

The fabricated nanopillars are as shown in the scanning electron micrograph (SEM) in Fig. 2-2(a). Due to the alternating etch and passivation steps characteristic of DRIE, scallop features were formed on the sides of the pillars (Fig. 2-2(b)).

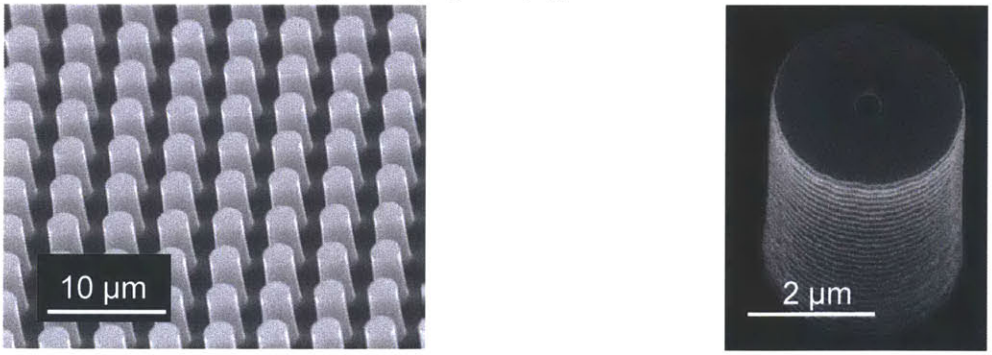

Fig. 2-2 Scanning electron micrograph (SEM) of a micropillar array. (a) Micropillars with diameters of 2.3 μm, pitches of 4.5 μm, and heights of 8.3 μm. (b) Magnified image of a single micropillar from (a) showing scalloped features on the sides from deep reactive ion etching (DRIE). [71]

2.3 Capillary Pressure in Micropillar Arrays

We determined the capillary pressure in the micropillar array using a thermodynamic approach minimizing interfacial free energy. The pressure is defined as the change in surface energy per unit volume,

$$P_{cap} = \Delta E / \Delta V \quad (2\text{-}1)$$

where ΔE is the decrease in surface energy as the liquid fills one unit cell and ΔV is the corresponding volume of the liquid filling one unit cell. To accurately predict the change in surface energy and volume, Surface Evolver (SE) was used to simulate the shape of the meniscus with minimum surface energy. A unit cell consisting of four quarter-pillars filled with water was defined as shown in Fig. 2-3(a). The effect of the scalloped features were included in the simulations as an effective surface energy where the scallops were approximated as a series of semi-circles with a roughness factor, $rf = \pi/2$. The intrinsic contact angle of de-ionized (DI) water on the silicon surface was measured by a goniometer to be $\theta = 38°$.
Gravitational effects were neglected due to the fact that for such length scales, the Bond number, defined as $Bo = \rho g l^2/\gamma$, is on the order of 10^{-5}.

Simultaneously, we used interference microscopy to examine the shape of the water meniscus in the microfabricated pillar arrays with diameters d ranging from 2.5 μm to 6.4 μm and periods l ranging from 8 μm to 30 μm. Fringes were generated by the interference of laser light (λ = 405 nm) reflected at the liquid surface and at the substrate (Fig. 2(b)). The shape of the water meniscus in the pillar arrays were obtained by examining the dark fringes, where each dark fringe corresponds to a λ/2n difference in the relative thickness of the liquid film, where n is the refractive index of the liquid and n=1.33 for water.

Figure 2-2 compares the simulated meniscus shape to experimental interference measurements on a micropillar array with diameter $d = 6.4$ μm and period $l = 15$ μm. Fig. 2(a) shows the three-dimensional meniscus shape obtained by SE and Fig. 2(b) shows the top-down view of the experimentally obtained interference patterns on the same pillar geometry. Close to the pillar sidewalls (< 1 μm), accurate data was difficult to obtain due to refraction. Fig. 2(c)-(e) compare the meniscus shape predicted by simulation and obtained experimentally along the horizontal (AB), diagonal (AD), and vertical (BC) directions, respectively. The error bars in the data were determined based on the width of the dark fringes. The experimental results were well-predicted by the simulation.

Experimental measurements on additional geometries were performed and exhibit similar agreements. For example, the comparisons between confocal measurements and SE simulation results of the menisci profiles on pillar arrays with diameter of 5.5 μm and period of 15 μm, and diameter of 10.2 μm and period of 15 μm are shown in Fig. 2-3 and 2-4, respectively.

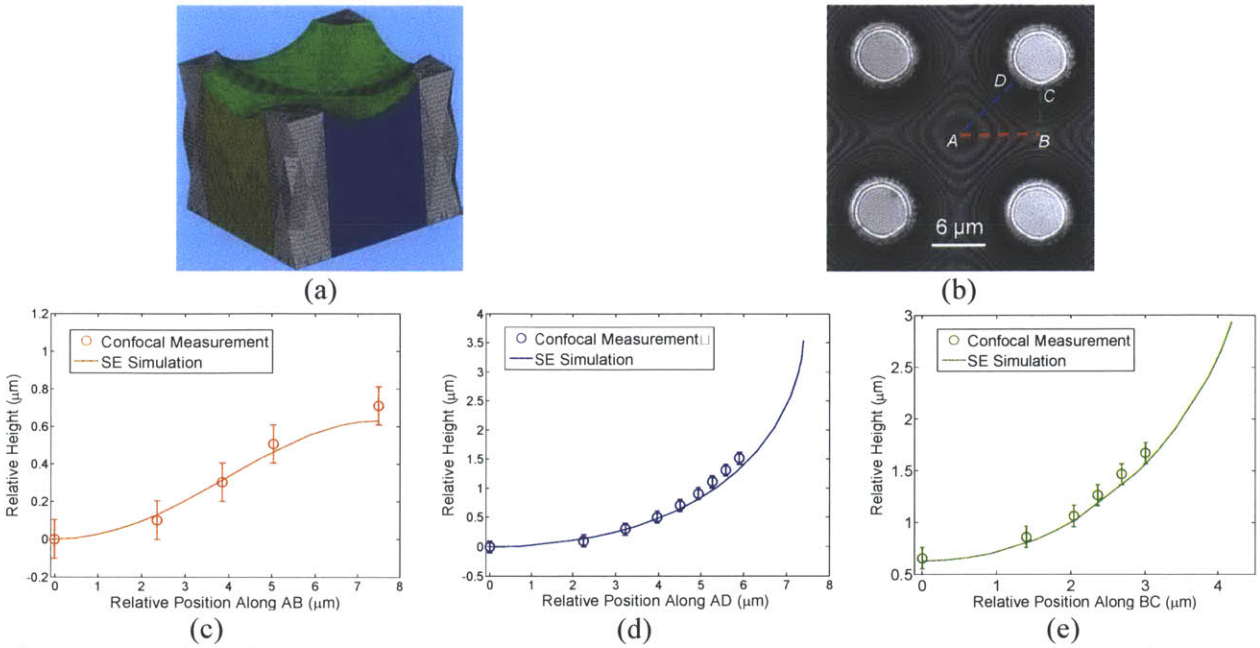

Fig.2-2 Comparison of water menisci shapes using simulations and experiments. (a) Simulated meniscus shape using Surface Evolver (SE). The pillar diameters are 6.4 μm and the pitches are 15 μm. (b) Image of the water meniscus obtained using interference microscopy in the same micropillar array as (a). Each dark fringe corresponds to a λ/2n difference in the relative thickness of the liquid film (λ=405 nm, n=1.33). Comparisons of the simulated and measured menisci along (c) the red line, AB, (d) the blue line, AD, and (e) the green line, BC. The ordinates correspond to heights relative to point A. [71]

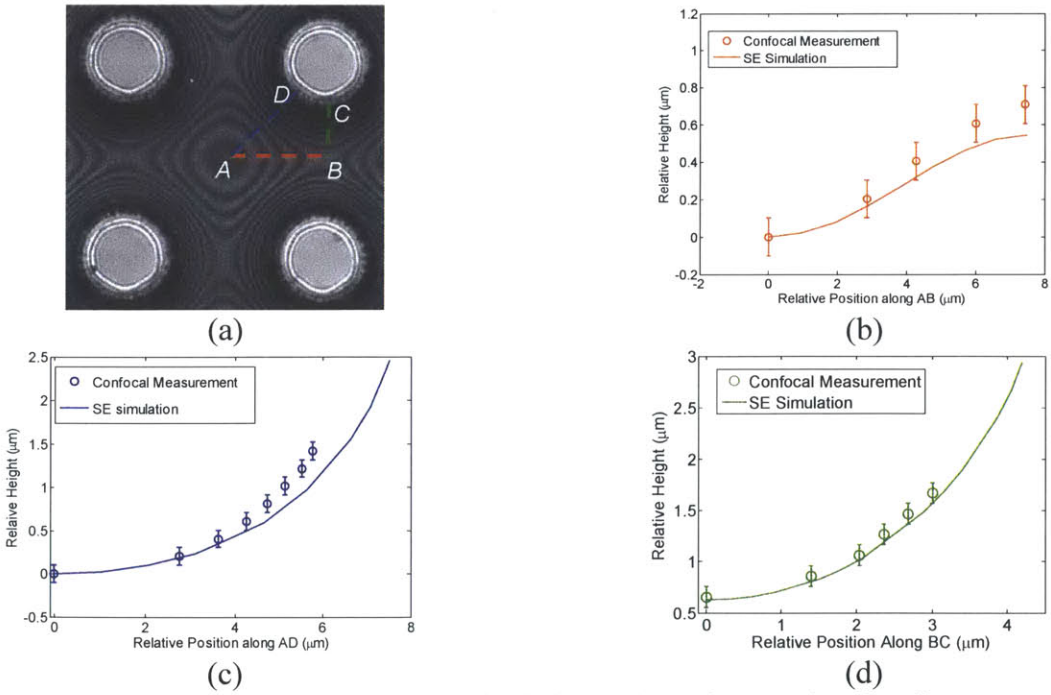

Fig. 2-3 Comparison of water menisci shapes using simulations and experiments. The pillar diameters are 5.5 μm and the periods are 15 μm. (a) Image of the water meniscus obtained using interference microscopy. Each dark fringe corresponds to a λ/2n difference in the relative thickness of the liquid film (λ=405 nm, n=1.33). Comparisons of the simulated and measured menisci along (c) the red line, AB, (d) the blue line, AD, and (e) the green line, BC. The ordinates correspond to heights relative to point A.

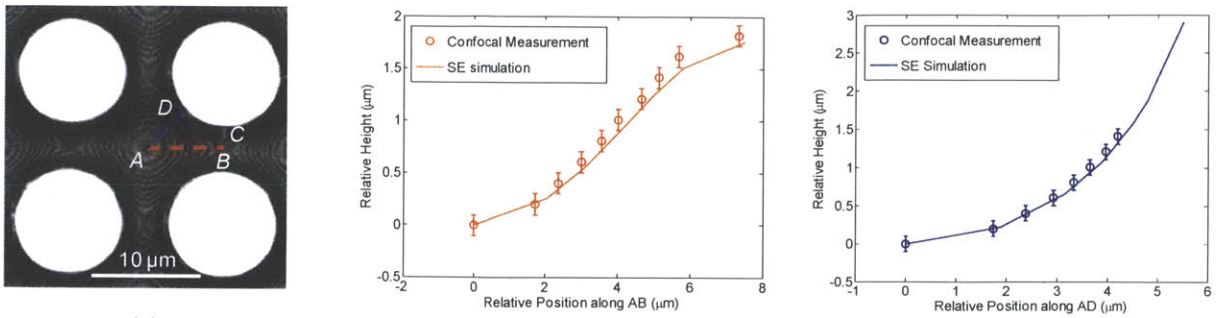

(a) (b) (c)

Fig. 2-4 Comparison of water menisci shapes using simulations and experiments. The pillar diameters are 10.2 μm and the periods are 15 μm. (a) Image of the water meniscus obtained using interference microscopy. Each dark fringe corresponds to a λ/2n difference in the relative thickness of the liquid film (λ=405 nm, n=1.33). Comparisons of the simulated and measured menisci along (c) the red line, AB, (d) the blue line, AD. The ordinates correspond to heights relative to point A. The meniscus profile along the green line, BC, cannot be measured due to strong reflection from the sidewall of the pillars

Based on the excellent agreement between simulations and experiments, SE was used to obtain general correlations for the volume of the liquid, ΔV, and the area of the menisci, A_m, by fitting the results from a large range of SE simulations on various geometries and $rf\cos\theta$ values, which is the surface energy change when a unit area on the sidewall of the pillars is wet. The fitting curves are given in Fig. 2-5.

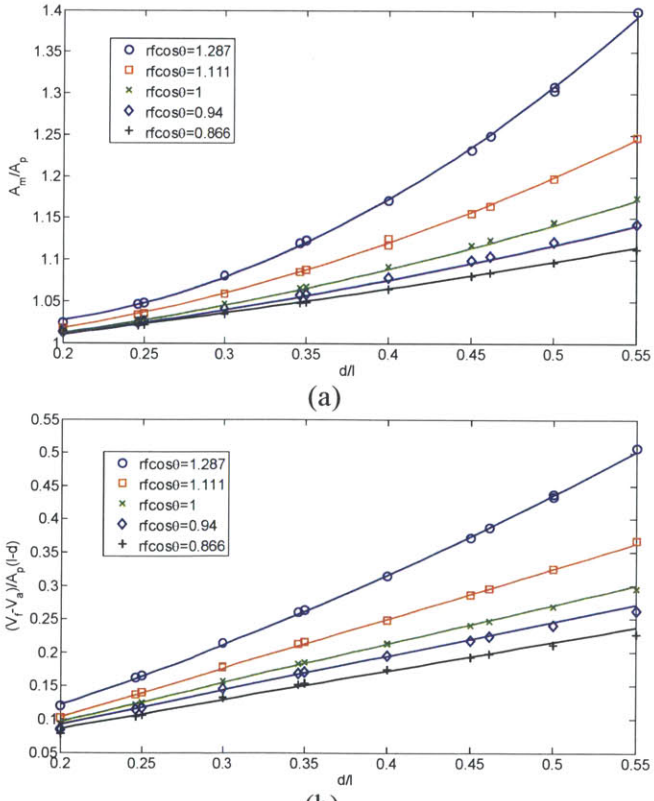

Fig. 2-5 Fitting curves for the (a) actual meniscus area (A_m) and (b) liquid volume (V_a) as functions of d/l ratio and $rf\cos\theta$. $A_P = l^2 - \frac{1}{4}\pi d^2$ is the projected area and $V_f = h(l^2 - \frac{1}{4}\pi d^2)$ is the full volume of one unit cell. [71]

Based on the fitting curves, the correlations can be determined as

$$\frac{A_m}{l^2-\frac{1}{4}\pi d^2} = 0.43 + 0.73rf\cos\theta + 3.76\left(\frac{d}{l}\right) - 0.046(rf\cos\theta)^2 - 5.53(rf\cos\theta)\left(\frac{d}{l}\right) - 4.05\left(\frac{d}{l}\right)^2 - 0.124(rf\cos\theta)^3 + 1.77(rf\cos\theta)^2\left(\frac{d}{l}\right) + 4.66(rf\cos\theta)\left(\frac{d}{l}\right)^2 \quad (2\text{-}2)$$

$$\frac{h\left(l^2-\frac{1}{4}\pi d^2\right)-\Delta V}{\left(l^2-\frac{1}{4}\pi d^2\right)(l-d)} = -0.175 - 0.345rf\cos\theta + 4.07\left(\frac{d}{l}\right) + 0.924(rf\cos\theta)^2 - 5.83(rf\cos\theta)\left(\frac{d}{l}\right) - 2.80\left(\frac{d}{l}\right)^2 - 0.439(rf\cos\theta)^3 + 2.41(rf\cos\theta)^2\left(\frac{d}{l}\right) + 2.71(rf\cos\theta)\left(\frac{d}{l}\right)^2 \quad (2\text{-}3)$$

Note that in previous studies using similar approach, the effect of the curvature in the meniscus was not considered, assuming the meniscus area is A_p and liquid volume is V_f. We demonstrate using SE simulation that such assumptions could lead to significant error. For example, on a surface where d = 2.5 μm, l = 5 μm, h = 5 μm, $rf = \pi/2$ and θ = 38°, the capillary pressure predicted by the corrected meniscus shape and liquid volume differs from a flat meniscus assumption by 15%.

With the prediction of meniscus shape, the capillary pressure can be obtained as

$$P_{cap} = \frac{\Delta E}{\Delta V} = \frac{\gamma \cdot rf\cos\theta \cdot \pi dh + \gamma\cos\theta\left(l^2-\frac{\pi d^2}{4}\right) - \gamma A_m}{\Delta V} \quad (2\text{-}4)$$

where γ is the surface tension of the liquid, θ is the intrinsic contact angle, and rf is the roughness factor on the sides of the pillars. The first and second term represent the energy change as the liquid wets the sides of the rough pillar and the smooth bottom surface of the unit cell, respectively. The third term corresponds to the energy change due to the formation of the meniscus. Using the Young-Laplace equation, the capillary pressure can be determined by the mean curvature of the meniscus. However, in such complex geometries, the mean curvature of the meniscus varies as a function of the position of the contact line, leading to a varying capillary pressure that is difficult to determine. The advantage of the thermodynamic approach is that an average driving pressure during the propagation process can be obtained without determining the shape of the meniscus at each instant in time. Meanwhile, this average pressure is only dependent on the difference in surface energy and volume between the states before and after the liquid filling the unit cell. The complex liquid meniscus at the front advances through each unit cell in a periodic manner, and therefore its contribution cancels out when calculating the change in surface energy. However, we observed in our experiments that two distinct time scales exist in the propagation process and vary as functions of the geometry. The time required for the liquid front to sweep from one pillar to the bottom of the next pillar is defined as τ_s and the time required for the liquid front to climb and wet the side of a pillar is defined as τ_p. Schematics

explaining the propagation process are shown in Fig 2-4. When $h \geq l$, τ_s and τ_p are comparable, such that the averaged approach described above to determine capillary pressure is accurate. On the other hand, when $h < l$, the two time scales start to deviate from each other where τ_s becomes dominant. In addition, slight variations in pillar diameter and local wettability become important. In such cases, Eqn (2-4) is no longer sufficient to describe the driving capillary pressure. The dynamics of the liquid front sweeping between pillars and its effect on the macroscale propagation will be discussed later in Chapter 3.

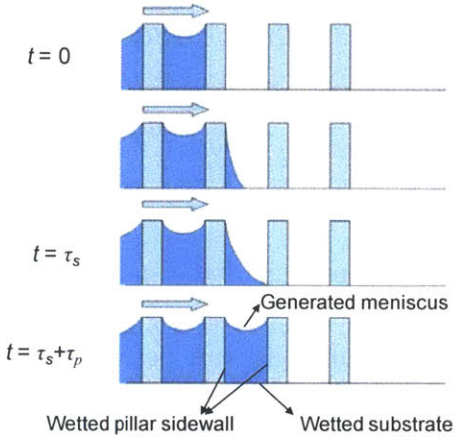

Fig. 2-6 Schematics representative of the propagation process. The meniscus in the propagation direction remains unchanged before and after the liquid wets one unit cell such that the change in surface energy is only generated by wetting the bottom and side of the pillars and formation of the top meniscus. [72]

2.4 Viscous Resistance in Micropillar Arrays

To determine the viscous resistance, previous works have used scaling and finite element analysis. We have used the one-dimensional form of Brinkman's equation to determine the viscous resistance, which is a modified form of the Navier-Stokes equation including a permeability term and is widely used in porous media studies,

$$\mu \frac{d^2u}{dy^2} - \frac{dP}{dx} - \mu\alpha^2 u = 0 \tag{2-5}$$

where u is the velocity, dP/dx is the pressure gradient necessary to drive the liquid flow, μ is the viscosity of the liquid, and α^{-2} is the permeability that accounts for the volumetric drag induced by the pillar array. In order to incorporate the friction from the bottom surface, the no slip boundary condition was applied at the bottom wall and a no shear boundary condition was applied at the liquid-air interface. Therefore, the velocity profile is determined as

$$u = Ae^{\alpha y} + Be^{-\alpha y} - \frac{1}{\alpha^2 \mu}\frac{dP}{dx} \tag{2-6}$$

where $= \frac{dP}{dx} e^{-\alpha h}/\alpha^2\mu(e^{\alpha h} + e^{-\alpha h})$, $B = \frac{dP}{dx} e^{\alpha h}/\alpha^2\mu(e^{\alpha h} + e^{-\alpha h})$ and h is the height of the pillars. The permeability of planar pillar arrays has been studied numerically by Sangani and Acrivos [67] and the following expression is given,

$$\alpha^{-2} = l^2 \frac{\ln c^{-1/2} - 0.738 + c - 0.887c^2 + 2.038c^3 + o(c^4)}{4\pi} \quad (2\text{-}7)$$

where $c = \pi d^2/4l^2$ is the solid fraction. Equation (2-7) is valid for arrays with $c < 0.25$, i.e., $d/l < 0.57$. Conveniently, pillar arrays with d/l greater than 0.57 are less commonly used in practice due to the large viscous losses associated with such densely packed arrays.
By inserting the permeability into Eqn (2-6), the viscous resistance, K, is now defined as the ratio of the pressure gradient,dP/dx, to the mean velocity, u_{mean},

$$K = \frac{(dP/dx)}{u_{mean}} = \frac{\Delta P_v}{x} \Big/ \frac{dx}{dt} \quad (2\text{-}8)$$

where ΔP_v is the pressure drop, x is the propagation distance, t is the propagation time.

To verify the model, finite element simulations were performed using COMSOL V3.4 (COMSOL Inc.) to obtain K for various pillar geometries. Comparisons between our semi-analytical model and numerical simulations show agreement to within 5%, as shown in Table 2-1.

d (μm)	h (μm)	l (μm)	K (x10^8 Pa·s/m^2, COMSOL)	K (x10^8 Pa·s/m^2, Brinkman's equation)	Discrepancy
2	5	8	4.15	4.03	2.89%
3.5	5	8	8.13	7.81	3.94%
3	5	8	6.20	5.95	4.03%
3	5	16	1.80	1.74	3.33%
3	14	10	2.27	2.38	4.85%

Table 2-1 Comparison of viscous resistance, K, from COMSOL simulations and Brinkman's equation on various geometries, where d, h, and l are the diameters, heights and periods of the pillar array, respectively. The discrepancies are within 5%.

2.5 Prediction of Propagation Rates and Experimental Validation

By combining the proposed capillary pressure and viscous resistance models described above, an overall model to predict the propagation distance as a function of time is obtained

$$P_{cap} = \Delta P_v = Kx\frac{dx}{dt}$$
$$x = \sqrt{2P_{cap}/Kt} = G\sqrt{t} \tag{2-9}$$

where P_{cap} is the capillary pressure determined from Eqn (2-1), and G is defined as the propagation coefficient.

Experiments were carried out on microfabricated pillar arrays with various geometries to validate the propagation model. The pillar diameters ranged from d = 1.3 - 6.4 μm, the periods ranged from l = 4.5 - 30 μm, and the heights ranged from h = 8.3 - 20 μm, yielding d/l ratios of 0.17 - 0.5 and h/d ratios of 4 - 8. The experimental setup is shown in Fig. 2-5(a), where a microfabricated surface was positioned vertically over a reservoir of de-ionized (DI) water. A thermocouple in the reservoir measured the water temperature to determine the viscosity and surface tension. The reservoir was translated upwards until it contacted the surface, resulting in one-dimensional propagation that was captured using a high speed camera (Phantom V7.1, Vision Research). Gravitational effects were neglected due to the short propagation distance (< 1 cm) such that ρgh << Pcap. Fig. 2-5(b) shows an image of an instant during the liquid propagation process with the liquid front highlighted by the black dashed line. Comparisons between the propagation distance as a function of time from our model and experiments are shown in Fig. 2-5(c) for d = 2.9 μm, l = 5.5 μm, and h = 8.3 μm, (d) for d = 2.82 μm, l = 8.1 μm, and h = 8.3 μm, and (e) for d = 1.8 μm, l = 7.7 μm, and h = 8.3 μm. Error bars were obtained by repeating experiments on each sample at least three times. Experiments were also performed on a variety of samples with d = 1.8 - 5.3 μm, l = 4.5 - 15 μm, and h = 8.3 - 25 μm. Fig. 2-5(f) summarizes the propagation coefficients, G, from experiments and compares with the model. Majority of the experimental results are in excellent agreement to within 5% except on a few samples, as highlighted in Fig. 2-5(f). These are the samples where $h < l$ and the two time scales mentioned in 2.3 start to separate. The propagation behavior on such samples will be investigated in Chapter 3.

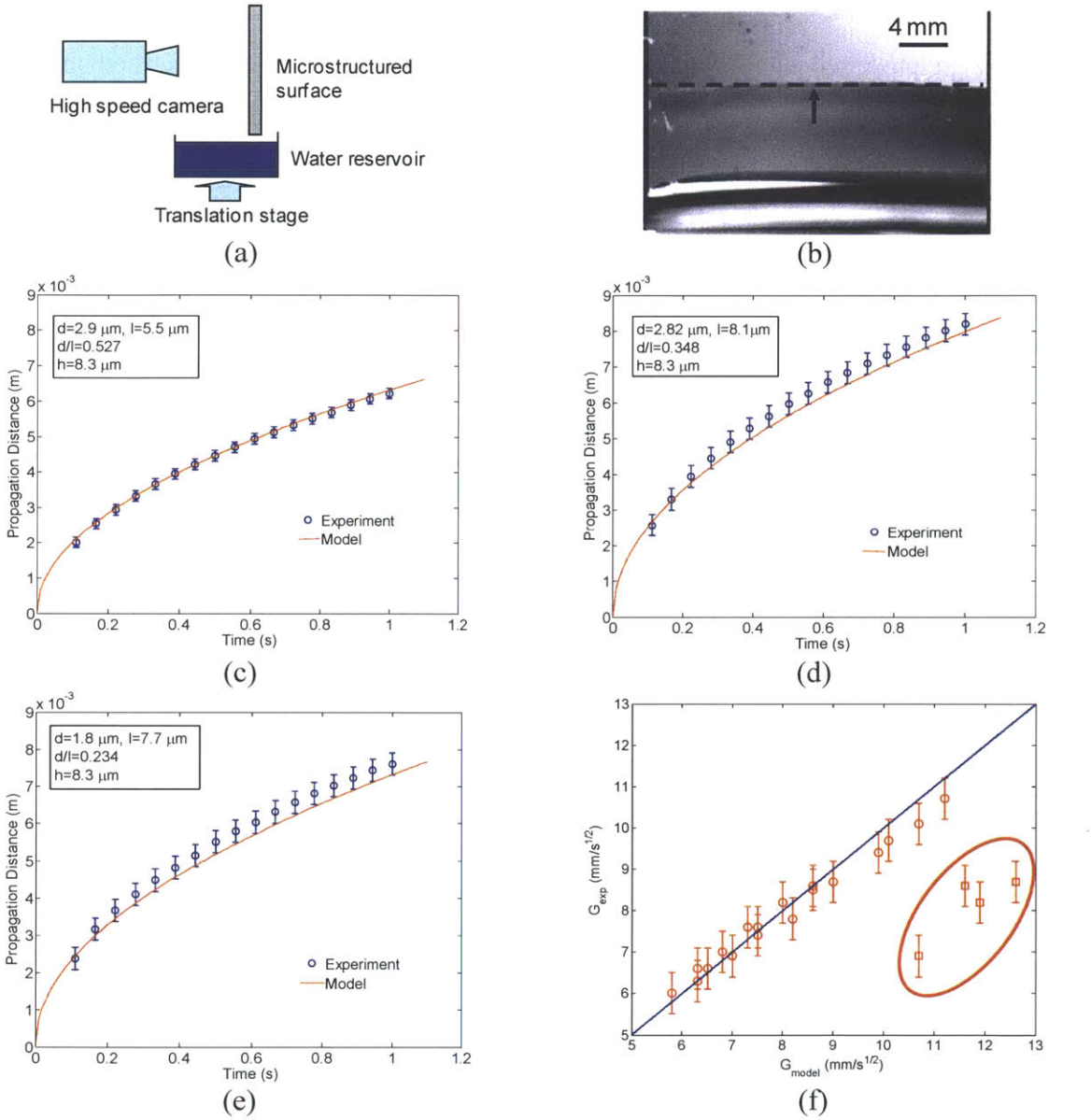

Fig. 2-7 Comparison of model and one-dimensional propagation experiments. (a) Schematic of experimental setup for liquid propagation studies. The microstructured surface placed vertically over a water reservoir that was translated upward until the water reached the surface and started to propagate. The propagation process was recorded with a high speed camera. (b) Image of liquid propagation on microstructured surface. The black dotted line shows the location of the liquid front. Comparison of the propagation distance as a function of time predicted by the model and experiments on pillars with (c) d=2.9 μm, l=5.5 μm, h=8.3 μm, (d) d=2.82 μm, l=8.1 μm, h=8.3 μm, and (e) d=1.8 μm, l=7.7 μm, and h=8.3 μm. (f) Summary of experimental propagation rates on a vareity of geometries and comparison with model results. The experimental results meet with model within 5% except on samples where $h < l$, which will be studied in Chapter 3. [71, 72]

2.6 Optimization of Pillar Geometries for Maximized Propagation Rates

Dimensionless analysis according to Buckingham Π-theory [73] was performed to simplify the previous modeling and derive optimization guidelines for pillar geometries. Six quantities (d, h, l, γ, μ, and G) were included in the model with three dimensions (length, time, and mass). Therefore, three dimensionless groups are expected (6 – 3 = 3). An effective propagation coefficient, $\mu G^2/\gamma l$, was obtained that is functionally dependent on only the dimensionless geometrical parameters h/d and d/l, where μ is the viscosity of the liquid, G is the propagation coefficient, and is the surface tension. Fig. 2-6(a) shows the relationship for water on silicon pillars with various d/l and h/d ratios. The relationship is valid with $h \geq l$ and $d/l < 0.57$. The effective propagation coefficient can be interpreted as a competition between the viscous resistance and the driving capillary pressure. As the ratio of h/d increases, the effective propagation coefficient increases and approaches an upper theoretical limit as $h \to \infty$. When the ratio of d/l increases, the viscous resistance and the capillary pressure both increase and a maximum effective propagation coefficient is reached. Beyond this limit, the viscous resistance increases faster than the capillary pressure, leading to a decrease in the effective propagation coefficient. The optimal d/l ratio and the corresponding maximum effective propagation coefficient for varying h/d ratios are shown in Fig. 2-6(b).

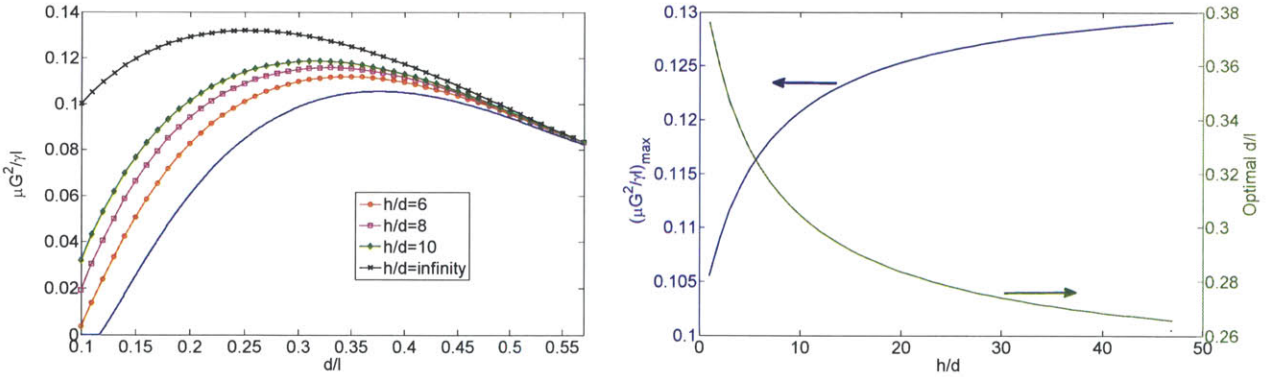

(a) (b)

Fig. 2-8 Design guidelines for the optimization of pillar array geometries for h ≥ l and d/l ≤ 0.57. (a) Effective propagation coefficients predicted by the model for varying d/l and h/d ratios. (b) Design guidelines for maximum effective propagation coefficients on micropillar arrays with various aspect ratios and the corresponding optimal d/l ratios. [71]

2.7 Conclusions

To summarize, we have presented a predictive liquid propagation model following Washburn dynamics for the case where $h/l \geq 1$ and $d/l < 0.57$. The complex shape of liquid meniscus was simulated using Surface Evolver (SE) based on surface energy minimization and validated with interference measurement of liquid thickness. The capillary pressure was determined as the rate

of change in surface energy per unit volume change using correlations based on SE simulations. The viscous resistance was determined using Brinkman's equation incorporating the effects of both the bottom surface. The propagation model was validated with one-dimensional propagation experiments, showing agreement to within 5% in the targeted geometry range. An effective propagation coefficient, obtained through dimensionless analysis, was determined to be only a function of the ratios h/d and d/l. Finally, design guidelines are provided to optimize micropillar geometries to enhance liquid transport for a variety of microfluidic applications.

For the case where $h < l$, the complex dynamics of liquid front sweeping between the pillars start to play a significant role therefore the averaged approach used in this chapter to determine the capillary driving force is no longer accurate. Such behaviors will be discussed in Chapter 3.

Chapter 3 Microscopic Sweeping of Liquid Front and the Effect on Macro Propagation

3.1 Overview

Chapter 2 derived a predictive model for overall propagation rate in micropillar arrays using an average capillary driving force targeted for tall, dense pillar arrays. This approach provides guidelines for optimization of pillar geometries where maximized propagation rates are desired. However, significant overpredictions in the propagation coefficients by our previous model were observed in sparse pillar arrays (Fig. 2-5(f)). Ishino *et al.* similarly identified these two distinct propagation behaviors in dense and sparse pillars [69], which were qualitatively attributed to different dominant length scales affecting the viscous resistance. Meanwhile, previous investigations indicate the presence of complex "microscopic" behavior of the liquid which occurs between individual pillars as a possible mechanism leading to the disparity in propagation coefficients. One example of such microscopic behavior is "zipping" identified by Sbragaglia *et al.* [74] and Pirat *et al.* [75] Once the liquid front reaches a single pillar in a subsequent column, the liquid immediately propagates perpendicular to the spreading direction at a higher rate compared to the liquid front moving towards the next column. While these studies provide increased insight, understanding the microscopic behavior of the liquid front along the propagation direction is lacking but needed, which can significantly contribute to the macroscopic liquid dynamics.

In this chapter, we investigated the microscopic dynamics of liquid front along the spreading direction. Highly localized sweeping behavior of the liquid front was captured and modeled using an integral approach. The effect of such microscopic behavior on macroscopic propagation rates will be quantified, which show good agreement with experimental validations.

3.2 Imaging of Sweeping Liquid Front

A series of time lapse images of the microscopic sweeping behavior of the liquid front between columns of pillars is shown in Fig. 3-1(a) where the liquid propagates from left to right. "Zipping" [74, 75] can be clearly observed such that the liquid front first wets the upper pillars and propagates downwards to wet lower ones in the column, which leads to a slanted liquid front. However, the sweeping behavior along the spreading direction is unaffected by the zipping perpendicular to the spreading direction. Once the liquid front reaches and wets a single pillar, the liquid front starts to sweep locally from left to right. Meanwhile, the zipping continues towards the bottom of the image where the zipping only determines when the liquid front starts

to move. As a result, the sweeping distance of the liquid front can be measured locally and investigated independently of the zipping behavior.

Silicon micropillar arrays of two geometries with diameters d=8 μm and 9 μm, periods l=25 μm and 20 μm, and heights h=17 μm, were investigated with both water and isopropyl alcohol. A 5 μL droplet of liquid was deposited and propagated on the substrate. During this process, images of the microscopic spreading behavior was captured with a white light microscope (Eclipse LV-100, Nikon) with a magnification of 100x (NA=0.70) and high-speed camera (Phantom V7.1, Vision Research) at a frame rate of 2000 fps. The sweeping distance of the liquid, s, was measured as a function of time, t, at a specific y-location (Fig. 3-1(b) and (c)). Droplets were placed at two different locations on the sample with l=20 μm. In all cases, the sweeping distance was determined to be proportional to $t^{1/5}$, which is independent of geometry, propagation distance, and the liquid.

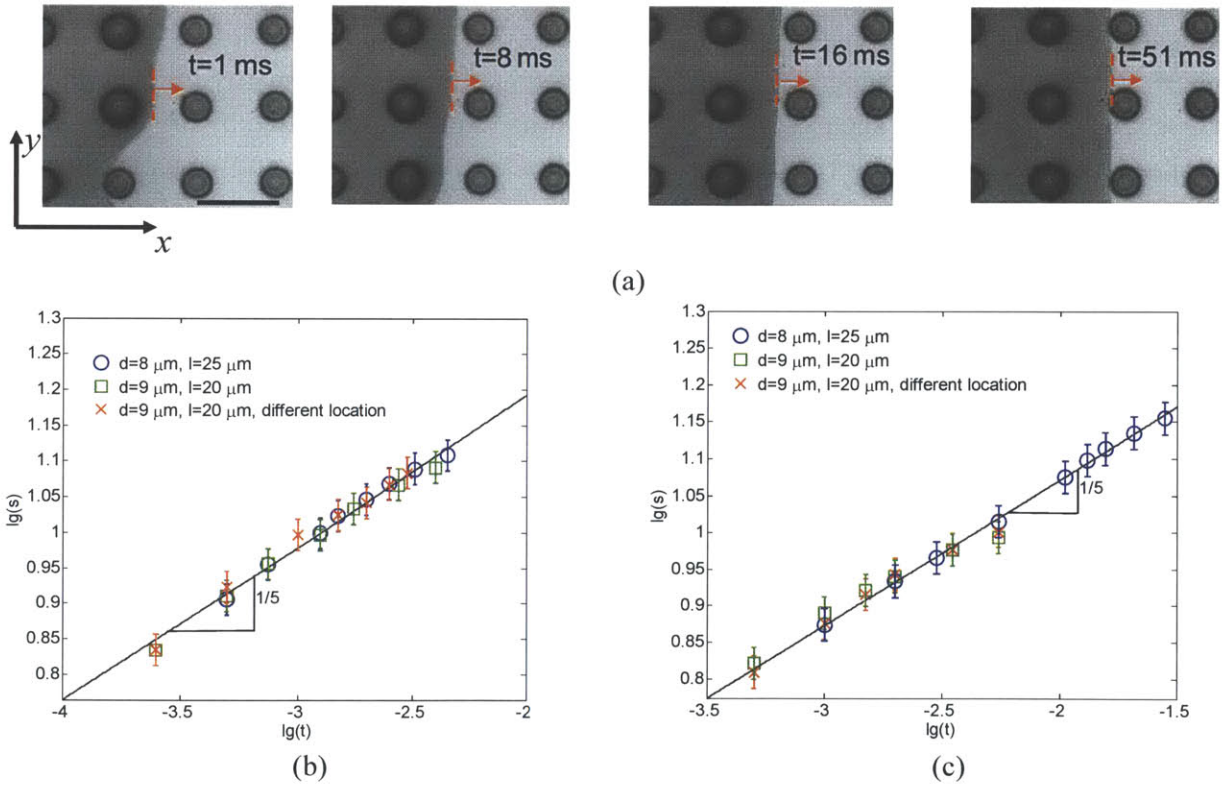

Fig. 3-1(a) Time lapse images of the liquid front represented by the red dotted line sweeping between columns of pillars with the white dotted line as the reference location. Scale bar is 25 μm. The sweeping distance of the liquid front, s, scales with $t^{1/5}$ for both (b) water and (c) isopropyl alcohol, which is independent of geometry and location. Error bars were determined based on the uncertainty in the imaging. [72]

3.3 Modeling of Sweeping Dynamics

To understand the t1/5 scaling, the liquid front which determines the local pressure gradient was investigated using interference microscopy. The results suggest that the liquid profile can be approximated by a second order polynomial function $= ax^2 + bx + c$. Fig. 2-2(a) shows a representative interference pattern of the liquid front on a pillar array with d = 5.9 μm, l = 15 μm, and h = 3 μm acquired by a confocal microscope system (VThawk, Visitech International) with a laser source (λ = 532 nm). Each dark fringe corresponds to a λ/2n difference in the thickness of the liquid, where n is the index of refraction of the liquid (n = 1.33 for water). The meniscus profiles along two different locations, AB and A'B' in Fig. 3-2(a), are shown in Fig. 3-2(b).

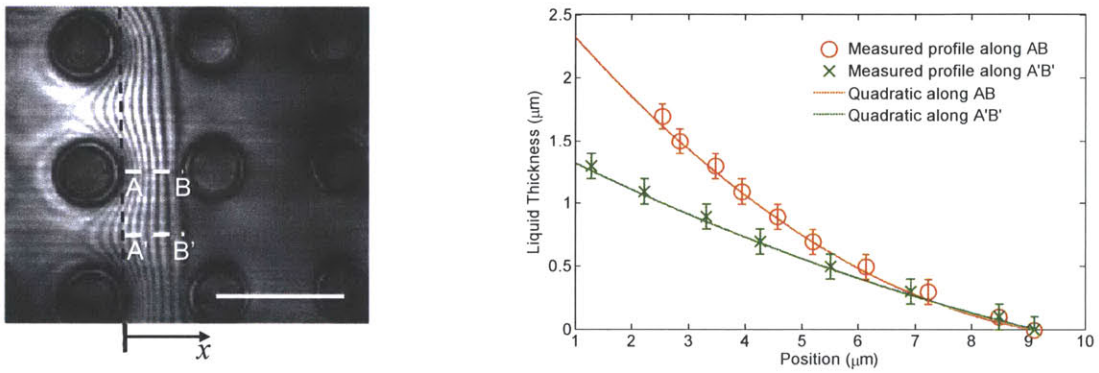

(a) (b)

Fig. 3-2 Profile of the propagating meniscus. (a) Interference microscopy image of the liquid meniscus sweeping between pillars (laser wavelength λ=532 nm). The diameter, period, and height of the pillar array are d = 5.1 μm, l = 15 μm, and h = 3 μm, respectively. Each dark fringe corresponds to a λ/2n difference in the liquid thickness. Scale bar is 15 μm. (b) Measured meniscus profiles along two locations, AB and A'B'. The profiles are well-captured by quadratic functions at both locations. Error bars were defined by the maximum possible height difference within one dark fringe (λ/2n).[72]

To understand the $t^{1/5}$ scaling, the liquid front which determines the local pressure gradient was investigated using interference microscopy. The results suggest that the liquid profile can be approximated by a second order polynomial function $y = ax^2 + bx + c$. Fig. 3(a) shows a representative interference pattern of the liquid front on a pillar array with d = 5.9 μm, l = 15 μm, and h = 3 μm acquired by a confocal microscope system (VThawk, Visitech International) with a laser source (λ = 532 nm). Each dark fringe corresponds to a $\lambda/2n$ difference in the thickness of the liquid, where n is the index of refraction of the liquid (n = 1.33 for water). The meniscus profiles along two different locations, AB and $A'B'$ in Fig. 3-2(a), are shown in Fig. 3-2(b). To determine the coefficients a, b, and c, three boundary conditions are needed. From the measured meniscus profile, we determined that

$$y(0) = h \tag{1a}$$

$$y(s) = 0 \tag{1b}$$

$$\left(\frac{dy}{dx}\right)_{x=s} = -\tan\theta \tag{1c}$$

where s is the sweeping distance, h is the liquid thickness at x=0, and θ is the contact angle at the liquid front. We obtain the coefficients as

$$a = \frac{h - s\tan\theta}{s^2} \tag{2a}$$

$$b = \frac{s\tan\theta - 2h}{s} \tag{2b}$$

$$c = h \tag{2c}$$

Therefore, the curvature of the profile is

$$\Lambda = \frac{y''}{(1+y'^2)^{3/2}} = \frac{2a}{(1+4a^2x^2+4abx+b^2)^{3/2}} \tag{3}$$

According to Young-Laplace equation, the capillary pressure P_{cap} is proportional to the curvature Λ. As a result, the pressure gradient is proportional to the gradient of the curvature

$$\frac{dP_{cap}}{dx} \propto \frac{d\Lambda}{dx} \tag{4}$$

where

$$\frac{d\Lambda}{dx} = -\frac{3}{2}\cdot 2a\cdot(1+4a^2x^2+4abx+b^2)^{-5/2}\cdot(8a^2x+4ab) \tag{5}$$

By considering the liquid front at $x = s$ and substituting a, b, and c by their values determined from Eqn 2a-c, the gradient of the curvature with known quantities at the liquid front is given as

$$\begin{aligned}
&\left.\frac{d\Lambda}{dx}\right|_{x=s} = -\frac{3}{2}\cdot 2a\cdot(4a^2x^2+4abx+b^2+1)^{-5/2}\cdot(8a^2x+4ab)\\
&= -3a\cdot\left[\frac{4(h-s\tan\theta)^2}{s^4}x^2+\frac{4(h-s\tan\theta)(s\tan\theta-2h)}{s^3}x+\frac{4(s\tan\theta-2h)^2}{s^2}+1\right]^{-5/2}\\
&\cdot\left[\frac{8(h-s\tan\theta)^2}{s^4}x+\frac{4(h-s\tan\theta)(s\tan\theta-2h)}{s^3}\right]\\
&= -3a\cdot\left[\frac{4(h-s\tan\theta)^2+4(h-s\tan\theta)(s\tan\theta-2h)+4(s\tan\theta-2h)^2+s^2}{s^2}\right]^{-5/2}\\
&\cdot\frac{8(h-s\tan\theta)^2+4(h-s\tan\theta)(s\tan\theta-2h)}{s^3}\\
&= -3\frac{h-s\tan\theta}{s^2}\left(\frac{s^2+s^2\tan^2\theta}{s^2}\right)^{-5/2}\frac{4s\tan\theta(s\tan\theta-h)}{s^3}\\
&= 3(1+\tan^2\theta)^{-5/2}\frac{4\tan\theta(h-s\tan\theta)^2}{s^4}
\end{aligned} \tag{6}$$

Therefore,

$$\frac{dP_{cap}}{dx} \propto \frac{4\tan\theta(h - s\tan\theta)^2}{s^4} \tag{7}$$

For a wetting liquid, the angle θ is small, so that h-$s$tan$\theta \approx h$, such that the pressure gradient scales with s^{-4},

$$\frac{dP_{cap}}{dx} \propto \frac{1}{s^4} \tag{8}$$

Moreover, for a pressure driven flow, the average velocity of the liquid is proportional to the pressure gradient

$$U = \frac{ds}{dt} \propto \frac{dP}{dx} \propto s^{-4} \tag{9}$$

such that s is proportional to $t^{1/5}$

$$s \propto t^{1/5} \tag{10}$$

The model results match the experimental results well (Fig. 3-1(b) and (c)). Note that this scaling is distinct from that obtained from Tanner's law [76]. While Tanner also examined the sweeping of the liquid front driven by capillary pressure, the thickness of the liquid, h, decreases. In micropillar arrays, the liquid pins at the top of the pillars and maintains a constant h [69, 77]. Therefore the sweeping distance is proportional to the 1/5th power of time in pillar arrays compared to the 1/7th power in Tanner's case.

3.4 Effect of Sweeping on Macroscale Propagation

With an increased understanding of the microscopic dynamics of the propagating liquid front, we investigated the effect of this microscopic behavior on the macroscopic propagation. From a macroscopic perspective, the propagation distance is proportional to $t^{1/2}$, which suggests that the macroscale propagation is determined by the balance between the viscous resistance and the capillary pressure. However, the microscopic sweeping behavior affects the propagation coefficient by influencing the capillary pressure, which is generated by wetting a hydrophilic surface. Two time scales are involved in the overall propagation process as shown in Fig 2-3(a) associated with: 1) the local sweeping behavior to reach the next column of pillars, from state 1 to state 2 (Fig. 2-3(a)) and 2) after the sweeping, the capillary pressure to bring liquid from the reservoir to fill the unit cell and initiate the sweeping in the next unit cell, from state 2 to state 3 (Fig. 2-3(a)). During the sweeping process, the bottom surface wets but this part of the interfacial energy is dissipated immediately by viscous effects (Re ~ 10^{-2}). Therefore, the amount of the interfacial energy to generate the capillary pressure to fill the unit cell is reduced. When the pillars are sparse, the dissipated part of the interfacial energy becomes more significant, resulting

in the deviation between model prediction and experiments in sparse pillar arrays observed previously.

To validate this theory, we developed an energy-based model to determine the capillary pressure in micropillar arrays and compared the results to experiments. As shown in Fig. 3-2(b), the liquid profile is assumed to be a second order polynomial $y(x)$ determined based on Eqn(1). After the microscopic sweeping process (state 2), the area of the liquid-air interface is determined as

$$S_{LV} = l\int_0^l \sqrt{1+y'^2(x)}dx \tag{11}$$

where l is the period of the array and h is the height of the pillars. As the liquid is drawn from the reservoir to fill the unit cell, the new area of liquid-air interface at state 3 is

$$S'_{LV} = A_m + hl \tag{12}$$

where A_m is the top surface area of the meniscus after the unit cell is filled, which can be determined by the previous model [6]. Therefore, the change in the area of liquid-air interface can be determined as

$$\Delta S_{LV} = A_m + hl - l\int_0^l \sqrt{1+y'^2(x)}dx \tag{13}$$

During the process, the area of the solid-liquid interface is increased by

$$\Delta S_{SL} = r_f \pi dh \tag{14}$$

where r_f is the roughness factor of the pillar sidewall. As a result, the interfacial energy difference from state 2 to state 3 can be determined as

$$\begin{aligned}\Delta E &= -\gamma \Delta S_{LV} + \gamma \cos\theta \Delta S_{SL} \\ &= \gamma\left[l\int_0^l \sqrt{1+y'^2(x)}dx - A_m - hl\right] + \gamma\cos\theta\left(r_f \pi dh\right)\end{aligned} \tag{15}$$

where γ is the surface tension of the liquid and θ is the intrinsic contact angle on the substrate. When the microscopic sweeping process is not considered, the interfacial energy difference from state 1 directly to state 3 is determined as

$$\Delta E' = \gamma\left(l^2 - \frac{\pi}{4}d^2 + r_f \pi dh\right)\cos\theta - \gamma A_m \tag{16}$$

The variation between the two energy differences is the part of interfacial energy difference dissipated by viscosity in the microscopic sweeping process. We define an overestimation factor that compares the capillary pressure excluding the sweeping process to that including the

sweeping process. Meanwhile, the capillary pressure is determined as the change in interfacial energy per unit volume [71]. The volume of liquid filling one unit cell is fixed by the geometry, without or with considering the sweeping process. Therefore, the ratio of capillary pressures can be determined as the ratio of the interfacial energy differences

$$OF = \frac{\Delta E'}{\Delta E} = \frac{\left(l^2 - \frac{\pi}{4}d^2 + r_f \pi dh\right)\cos\theta - A_m}{\left[l\int_0^l \sqrt{1+y'^2(x)}dx - A_m - hl\right] + \cos\theta\left(r_f \pi dh\right)} \tag{17}$$

The overestimation factor as a function of *h/(l-d)* is plotted as the solid red line in Fig. 3-3(b). While the actual meniscus shape during the sweeping process is complicated such that calculating the exact surface energy is challenging, the overestimation factor facilitates a comparison with the experiments, as described below.

In the experiments, micropillar arrays with d=5 μm, l=12.5 μm - 30 μm, and h=17 and 25 μm were investigated. The viscous resistances are calculated from the known geometries[71] and the actual propagation rates are measured experimentally. Therefore the actual capillary pressure can be determined. To make a reasonable comparison with the model results, the overestimation factor for the experiments is defined by a ratio of the capillary pressure determined from the previous model [71], where the sweeping process is not considered, to the experimentally determined capillary pressure, where the sweeping process is present, as shown with the blue circles. Note that as the pillars become sparse, the overestimation factor from the experiments becomes significantly larger than 1, which is also well-captured by the model. The results indicate that the reduction in interfacial energy by the microscopic sweeping is the mechanism for the overestimation of propagation rates. Therefore, to predict the macroscopic propagation rates, the capillary pressure should be modified according to the overestimation factor.

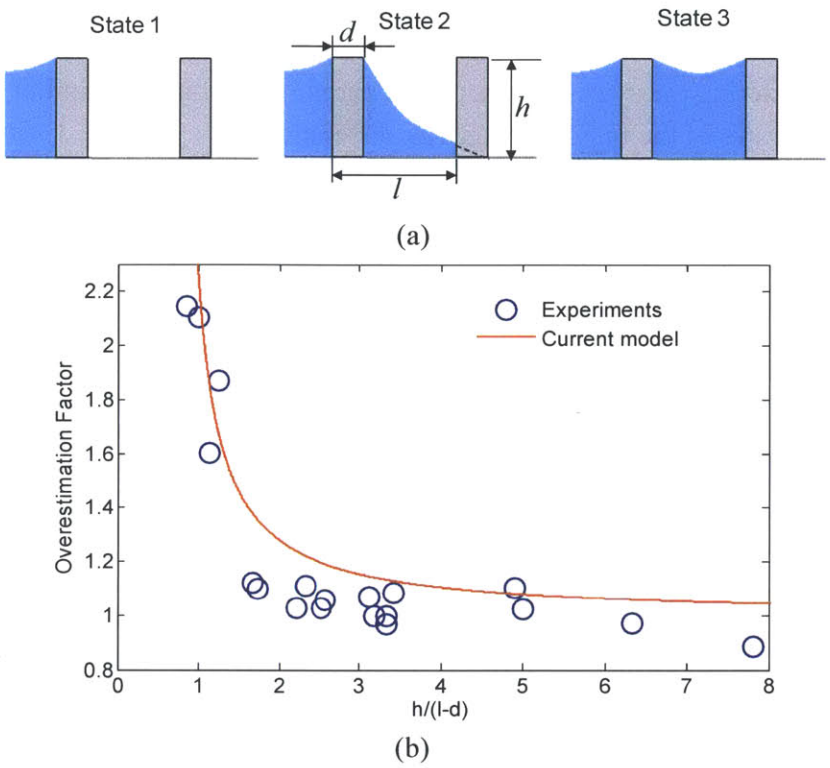

Fig. 3-3 Effect of the microscopic sweeping process on the macroscale propagation. (a) Schematics approximating the microscopic sweeping process, which reduces the interfacial energy to generate the capillary pressure. (b) Overestimation factors (OF) determined from previous experiments and current model represented by the circles and solid line, respectively, on various geometries. The model matches the experiments well, showing that the sweeping behavior explains the overprediction of capillary pressure and propagation coefficient. [72]

3.5 Complexities in Microscopic Sweeping

Above the discussions investigated the microscopic sweeping process in the simplified case where the sweeping liquid front can be approximated as a second order polynomial. However, more complicated liquid dynamics can be observed when the liquid completely wets the surface and the spacing between the pillars is very large. In such scenarios, the liquid front can extend to form a thin film where complex behaviors can come into effect. One example is shown in Fig. 3-4 where acetone is propagating in a micropillar array with diameter of 5 μm, height of 15 μm, and period of 25 μm. Liquid "bumps", represented by the circular droplets moving at the liquid front, were observed propagating at the front. This phenomenon could be related to the instability and rupture of the liquid front induced by the periodic pillar array but the detailed mechanism is still unclear. Future efforts could utilize pillar arrays with different periods and liquids with different combinations of viscosity and surface tension to investigate this phenomenon. The potential application can be accurate dispense of small amount of fluid with volume on the order of femtolitres.

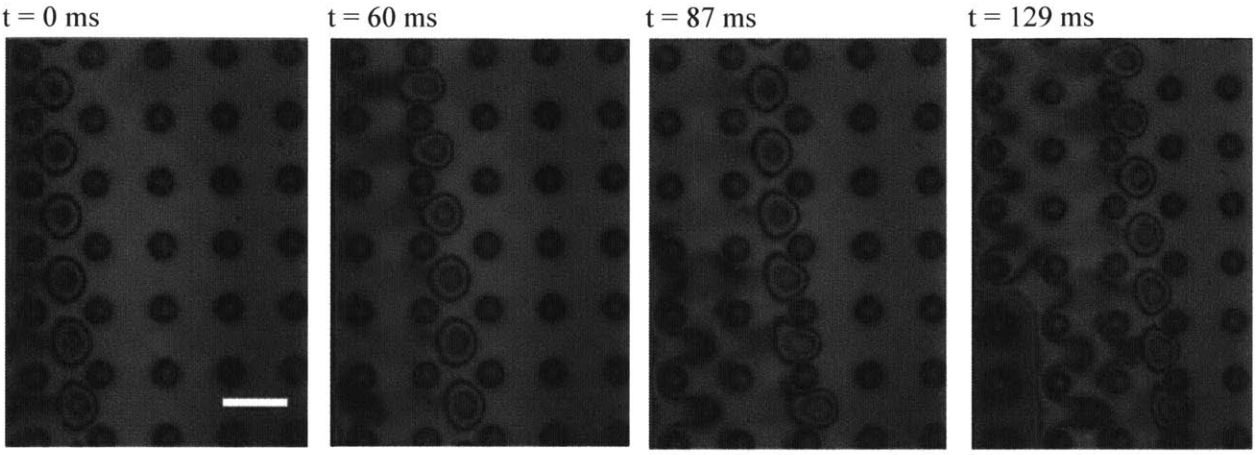

Fig. 3-4 Time lapse images of acetone propagation in a micropillar array with diameters of 5 μm, height of 15 μm, and period of 25 μm. Liquid "bumps" formed at the front and led the propagation. The fringes in the liquid were generated by the interference of laser source. The wavelength of the laser is 405 nm. The scale bar is 25 μm.

3.6 Conclusions

In summary, we investigated the microscopic sweeping behavior of liquids in micropillar arrays and determined the sweeping distance of the liquid front scales with $t^{1/5}$, which is explained with a simplified model capturing the capillary pressure gradient at the liquid front. We also showed through modeling and experiments that the sweeping behavior reduces the capillary pressure, which leads to the decrease in macroscopic propagation rate. This work offers important insights into explaining the role of microscopic dynamics in the prediction of macroscopic liquid propagation rates. Moreover, the local sweeping process can be utilized to achieve complex spreading behavior in microstructures, which promises exciting opportunities for various applications such as ultra-small volume liquid dispensing or nanoscale thermal management.

Chapter 4 Thin Film Evaporation from Nanoporous Membranes

4.1 Overview

In Chapter 2, a predictive model was developed for liquid propagation in micropillar arrays such that the geometries of the array can be optimized to enhance propagation rates. However, from Fig. 4-1(a) (same as Fig. 2-8(a)), an upper limit in propagation rates can be inferred. This upper limit is due to the balance between the capillary pressure and the viscous resistance. With a higher density of the pillars, the capillary pressure can be increased but the viscous resistance increases as well, and *vice versa*. Such an upper limit in propagation rates determines the maximum heat fluxes that can be dissipated via evaporation based on energy conservation. As shown in Fig. 4-1(b), using isopropyl alcohol as the working fluid and assuming the desired cooling length is 5 mm, the maximum heat fluxes that can be dissipated on micropillar arrays is on the order of 10 W/cm^2.

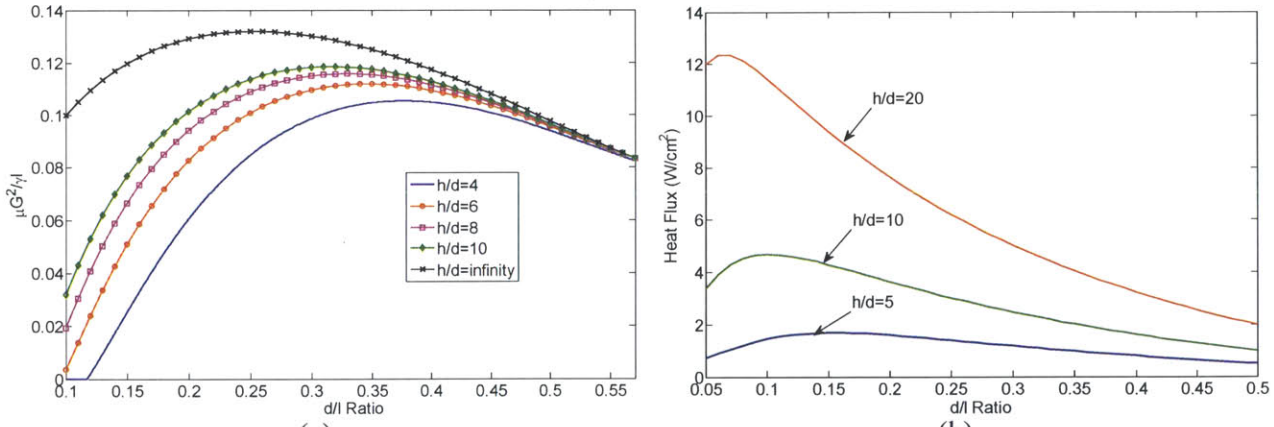

Fig. 4-1 Heat fluxes as a function of micropillar geometries. (a) Prediction of non-dimensional propagation rates as a function of micropillar geometries based on the balance between capillary pressure and viscous resistance. (b) Heat fluxes as a function of micropillar geometries based on energy conservation. The pillar diameters are assumed to be 5 μm and the cooling length is 5 mm. The working fluid is isopropyl alcohol.

Various approaches have been proposed to overcome such limits. Bi-porous wicks, for example, have been previously investigated where wide fluid paths between patches of dense micro/nanostructures were introduced to reduce the viscous resistance and enhance liquid transport. Using silicon bi-porous wicks, Coso *et al.* demonstrated maximum heat flux of 277 W/cm^2 with heat transfer coefficient of 19.6 W/cm^{2}K in a mixed mode of boiling and evaporation. With an evaporation dominant mode, the maximum heat flux was 119.6 W/cm^2 with heat transfer coefficient of 20.7 W/cm^{2}K [19]. Cai and Chen used carbon nanotube bi-porous wicks to achieve maximum heat flux of 600 W/cm2 and heat transfer coefficient of 21 W/cm^{2}K [52]. Such methods could significantly enhance the transport of fluid and increase the allowed heat flux. However, in such modified structures, the capillary pressure and the viscous

resistance are still coupled and determined by the same characteristic lengths, which will inevitably lead to a limit in the heat fluxes.

A new configuration for evaporative heat transfer is proposed as shown in Fig. 4-2(a). In the new configuration, evaporation occurs from nanopores with pore diameters of ~100 nm in a thin membrane. The small pore size enables the generation of large capillary pressures. The membrane will be supported by microscale ridges which also serve to conduct heat from the substrate to the membrane. The liquid flows in the wide channels between the ridges. In such a configuration, the capillary pressure, which is determined by the pore size, can be decoupled from the viscous resistance, which is determined by the spacing between the ridges.

The monolithic devices as shown in Fig. 4-2(a) would require extensive fabrication efforts. Before pursuing such complicated devices, we seek first to demonstrate a proof of concept for the configuration as shown in Fig. 4-2(b) in this chapter. A suspended membrane will be tested with liquid supplied from the bottom. The heat flux will be provided by a metal layer deposited at the top of the membrane. Membranes with varied thickness will be tested. Maximum interfacial heat fluxes of 96 W/cm^2 will be demonstrated using isopropyl alcohol as the working fluid, which is significantly higher than the critical heat flux of pool boiling. The effect of the membrane thickness on the interfacial heat fluxes will be explored to demonstrate an avenue to achieving heat fluxes over 1000 W/cm^2 for thermal management of next generation of electronic devices.

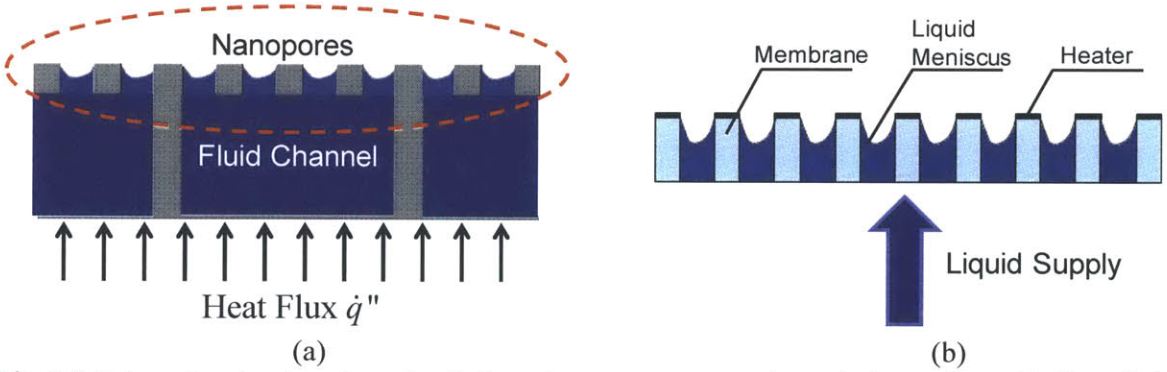

Fig. 4-2. Schematics showing alternative design using nanoporous membrane to de-couple capillarity and viscous resistance. (a) Schematic of the proposed thermal management device. (b) Schematic showing the proof of concept experiment in this chapter.

4.2 Experimental Setup

The nanoporous membranes used in our experiment was anodized aluminum oxide membranes (Unikera, Synkera Inc.) with diameter of 13 mm. The average pore diameter was 150 nm. A 35 nm thick platinum layer was deposited on top of the membrane by sputtering, which was used as resistance heater as well as temperature sensor. The liquid was driven by capillary pressure as well as disjoining pressure through the pores to form the menisci. An example macroscale image and SEM image of the membrane after metal deposition are shown in Fig. 4-2(a) and (b),

respectively. Note that the average pore diameter of 150 nm and porosity of 32% is based on manufacturer's specifications. Based on image analysis of the SEM image after metal deposition, the porosity of this membrane is reduced to 14% by the metal layer. Later, we show that the porosity after metal deposition ranges and needs to be quantified for every batch of fabricated membranes.

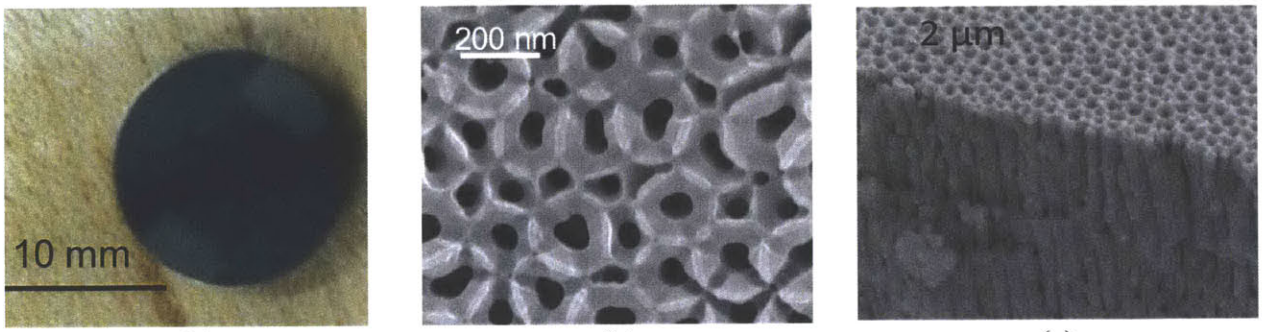

(a) (b) (c)

Fig 4-2 (a) Macroscale image of the membrane after metal deposition. (b) and (c) SEM image of the membrane after metal deposition. The porosity for this specific membrane was reduced to 14%.

During the experiment, the temperature was measured by the change in the resistance of the metal layer. However, due to the nanoscale geometry of the platinum layer and the sputtering fabrication process, the electrical property of the metal layer is different from that of the bulk material. Therefore, the temperature coefficient of resistivity was calibrated by an oven and a RTD thermal probe. The result of the calibration is shown in Fig. 4-3. The temperature coefficient of resistance was found to be 0.00143 K^{-1}.

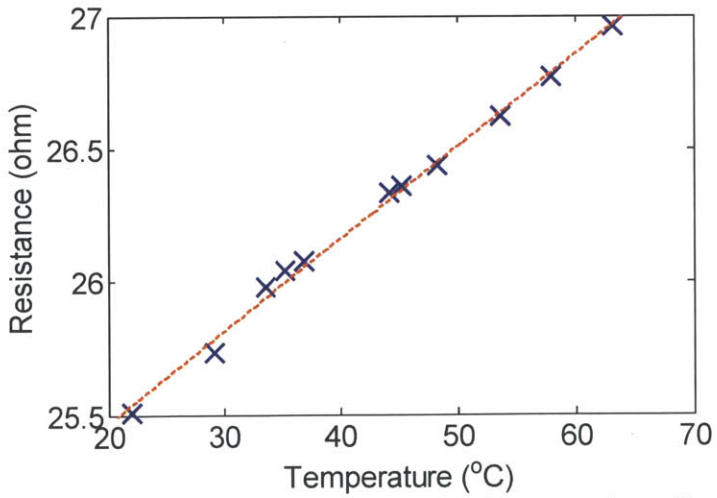

Fig. 4-3 Calibration of the temperature coefficient of resistivity for the sputtered metal layer. The temperature coefficient was found to be 0.00143 K^{-1}.

In the experiment, the membrane was attached to a liquid feed column with the edge of the membrane sealed by vacuum epoxy (Torr Seal, Varian Inc.) to ensure that liquid can only transport through the nanopores in the membrane, as shown in Fig. 4-4(a). The area that can be

wetted by the fluid in the membrane is 0.5 cm^2. Considering the porosity of 14%, the actual interfacial area available for evaporation is 0.07 cm^2. The liquid feed column is placed in a vacuum chamber (Kurt J. Lesker). A vacuum pump removes the vapor generated during evaporation to eliminate the thermal resistance associated with vapor transport. The pressure of the chamber is monitored by a pressure transducer. The bottom of the liquid feed column is connected to a liquid reservoir outside the vacuum chamber at atmosphere. A voltage was supplied to the metal layer to provide the heat fluxes. The voltage and current was measured by multimeters (Multimeter 2001, Keithley) and recorded by a computer using LabView (National Instruments) program such that the total heating power and temperature can be recorded. The data was acquired at a frequency of 1 Hz. The schematic and actual image of the setup is shown in Fig. 4-4(b) and (c), respectively. At each heating power, the membrane is allowed to reach steady state where the temperature variation is typically lower than 2 degrees over 100 seconds. After that, the heating power is varied to gather more data points.

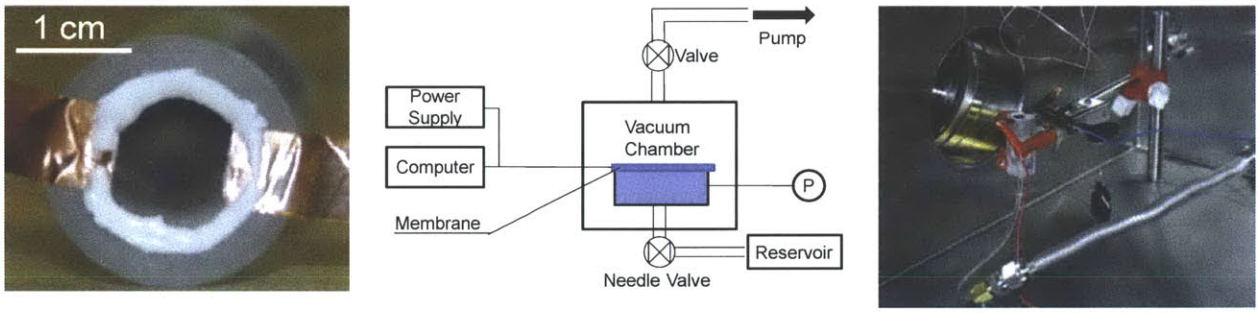

(a) (b) (c)

Fig. 4-4 Experimental setup (a) Image of the membrane attached to the liquid feed column. (b) Schematic showing the experimental setup. (c) Image of the experimental setup placed in the vacuum chamber.

In the experiments, the heat was dissipated by evaporation, conduction through the fixture, and convection through the liquid. The conduction heat loss through the fixture can be determined by measuring the temperature change as a function of heating power without liquid supply, as shown in Fig. 4-5. In the test, the chamber was pumped down the actual experiment condition (~60 Pa). The heat loss through the fixture was found to be around 0.01 W/K.

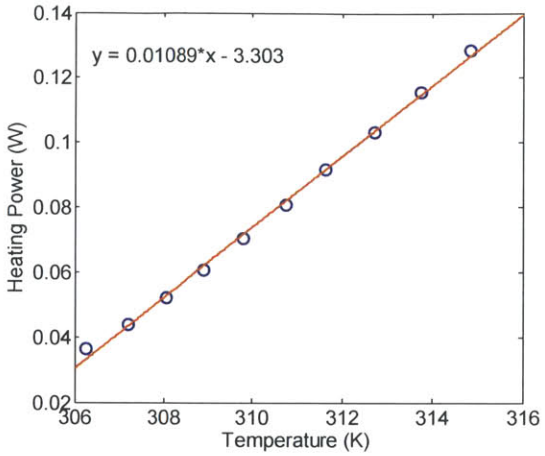

Fig. 4-5 Temperature of the membrane as a function of heating power without liquid supply. The conduction loss through the fixture was found to be around 0.01 W/K.

The heat loss through convection through the liquid is estimated using the correlation given by Kadambi and Drake for external natural convection of a heated horizontal plate facing down [78]

$$Nu_L = 0.82 Ra_L^{1/5} \tag{4-1}$$

where Ra_L is the Rayleigh number determined by

$$Ra_L = \frac{g\beta}{\nu\alpha}\Delta T L^3 \tag{4-2}$$

Given the fluid properties of isopropyl alcohol, the heat loss due to convection can be estimated to be

$$(hA) = 0.006\, W/K \tag{4-3}$$

Note that the correlation used here is for external natural convection where the fluid is not confined compared to the practical experiment fixture where the fluid is confined in the feed column. Therefore the calculated heat loss should be an overestimation compared to the actual case.

The typical temperature rise during the experiment is around 30-50 K. Therefore, the maximum total heat loss will be <0.8 W, which is very small compared to the applied heating power.

4.3 Experimental Results and Analysis

The variation of the steady state temperature of the membrane with the increase in heat flux is shown in Fig. 4-6(a). Different symbols indicate different tests, where good consistency was observed. Data was acquired using isopropyl alcohol (IPA) as the coolant. We used IPA instead of water due to the low surface tension of IPA, which allows wetting of the membrane even when the membrane gets contaminated and become less hydrophilic. Future effort will be focused on fabricating surfaces with robust hydrophilicity. As shown in Fig. 4-6(a), the initial heat transfer coefficient was relatively low with low heat flux. This result is because at the early stage, the liquid flow driven by the pressure difference applied by the vacuum pumping is higher than the evaporation rate. The top surface of the membrane was flooded by the excessive amount

of liquid, which introduced a large thermal resistance. As the heat flux was increased, the evaporation rate became higher than the flow rate driven by pressure difference and the excessive amount of liquid on the surface on the membrane evaporated. The heat transfer coefficient increased significantly as the liquid menisci receded back into the pores and formed thin film regions. With further increase in the heat flux, the menisci shape yielded larger thin film regions resulting in the continuous increase of the heat transfer coefficient. At this stage with higher heat transfer coefficient, the liquid was driven through the pores by a combination of the vacuum pumping pressure, the capillary pressure and the disjoining pressure. However, with further increase in the heat flux, the total driving pressure was no longer able to supply enough liquid for evaporation, and the membrane started to dry out with significant rise of the membrane temperature. The images showing the flooding and the thin film evaporation states of the membrane are shown in Fig. 4-6(b) and (c), respectively. The heat transfer coefficient of thin film evaporation can be determined as 1.3 W/cm^{2}K using the slope of the data points in the thin film operating state (dashed line in Fig. 4-6(a)). Before the drying out occurs, the maximum interfacial heat flux was ~50 W/cm^2 based on the actual interfacial area of 0.07 cm^2 at the working temperature of 345 K.

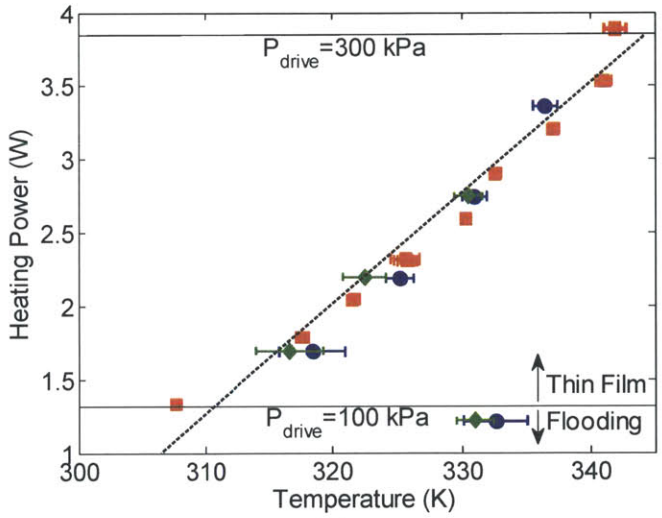

(a)

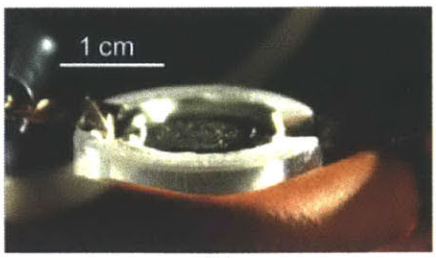

(b)

(c)

Fig. 4-6 Experimental results on 100 μm membranes. (a) Relation between total dissipated power and temperature. A drop in the temperature was observed at the transition between "flooding" and thin film regime. The heat transfer coefficient was determined to be 1.3 W/cm^{2}K and the maximum interfacial heat flux was 50 W/cm^2 based on the actual pore area of 0.07 cm^2. (b) Image of "flooding" of the membrane. Large droplets were observed on top of the membrane which limits the heat transfer coefficient. (c) Image of the thin film regime of the membrane. The droplets disappeared.

The transition between flooding and thin film evaporation occurred at a heating power of approximately 1.2~1.3 W, where the fluid transport through the nanopores is purely driven by the pressure difference (atmospheric pressure, ~100kPa) across the membrane. While at the dry-out point (~3.9 W), the fluid is driven by the combination of atmospheric pressure and capillary pressure. Based on energy conservation, the flow rate before the dry-out should be 3.9/1.3=3 times as large compared to the flow rate at the transition point between flooding and thin film evaporation. Therefore, the total driving pressure including atmospheric pressure and capillary pressure should be ~300 kPa. As a result, the fluid near the meniscus is in negative pressure (~-200 kPa). This negative pressure is allowed by nanoscale confinement of the pores which prevents the cavitation of fluid [79]. Using Young-Laplace equation, the maximum capillary pressure can be estimated as

$$P_{cap} = \frac{2\sigma}{r} = 746\ kPa \tag{4-4}$$

where σ is the surface tension of the liquid (~0.019 at 345K) and r is the average radius of the pores (~50 nm after metal deposition).

The actual demonstrated capillary pressure is significantly lower than the theoretical limit due to a few reasons. First of all, Young-Laplace equation assumes a circular pore while the actual pores in the membrane are not circular and have a distribution in the pore size, as can be seen in the SEM. Secondly, the fluid used in the experiment is only 99% pure. Significant contamination was observed after the experiment, as shown in Fig. 4-7(a) and (b). Such contamination reduces the capillary pressure available to drive the liquid transport.

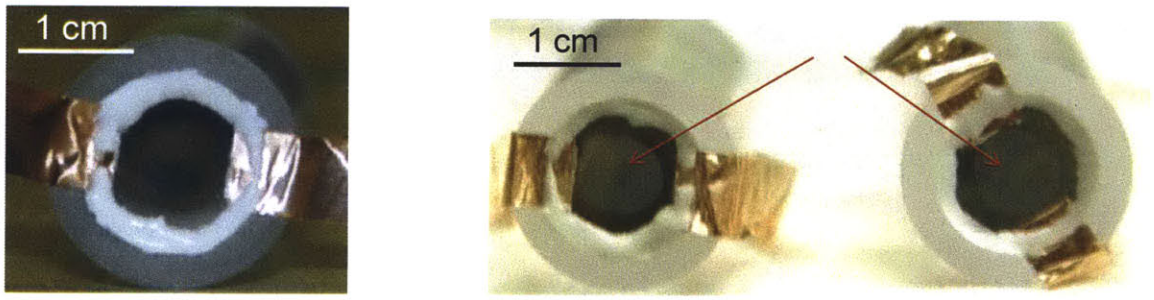

(a) (b)

Fig. 4-7 Contamination of membranes during evaporation. (a) Image of the membrane before experiments. (b) Image of membranes after the experiments. The arrows highlight the contaminated marks.

In order to evaluate the demonstrated interfacial heat flux of 50 W/cm^2, the critical heat flux (CHF) of IPA in pool boiling was estimated using Kandlikar's model for a benchmark comparison [32]. The CHF is dependent on the orientation of the heated surface and ranges from 39 W/cm^2 (vertical surface) to 73 W/cm^2 (horizontal surface). The demonstrated heat flux is comparable with CHF of pool boiling. The major limitation in the heat flux is the supply of fluid. Due to the relatively large thickness (100 μm) of the membrane, the viscous resistance of liquid flow through the nanopores is significant. However, assuming a constant driving capillary pressure of 200 kPa and same pore geometries, the maximum heat flux would be inversely proportional to the thickness of the membrane. Therefore, the decoupling between capillarity and

viscous resistance and significantly higher heat fluxes can be achieved by reducing the thickness of the membrane.

In order to validate the scaling, experiments using thinner membranes were performed. The thickness of the new membrane is reduced to 50 μm. SEM image of the pore geometries is shown in Fig. 4-8 (a), by which the porosity after the deposition was determined as 24% and the total pore area is 0.12 cm^2. The results are summarized in Fig. 4-8(b). The pressure in the chamber during the experiment is around 200-300 Pa. Due to the reduced thickness and higher porosity, a much larger amount of fluid can be pushed through the membrane at low heating power to form a liquid pool on top of the membrane where nucleation was observed in contrast to the liquid droplets observed on the 100 μm thick membranes. As a result, significant temperature fluctuation was seen at low heating power which prohibits recording accurate data. Meanwhile, with increased heating power, the flooding can be removed and the temperature becomes stabilized. The comparison between low heating power and high heating power is shown in Fig. 4-8(b). Therefore, in these experiments, the data points at low heating power are not shown. The transition from flooding and thin film evaporation is determined as the point where the fluctuation in temperature starts to diminish, which is around 2.9 W.

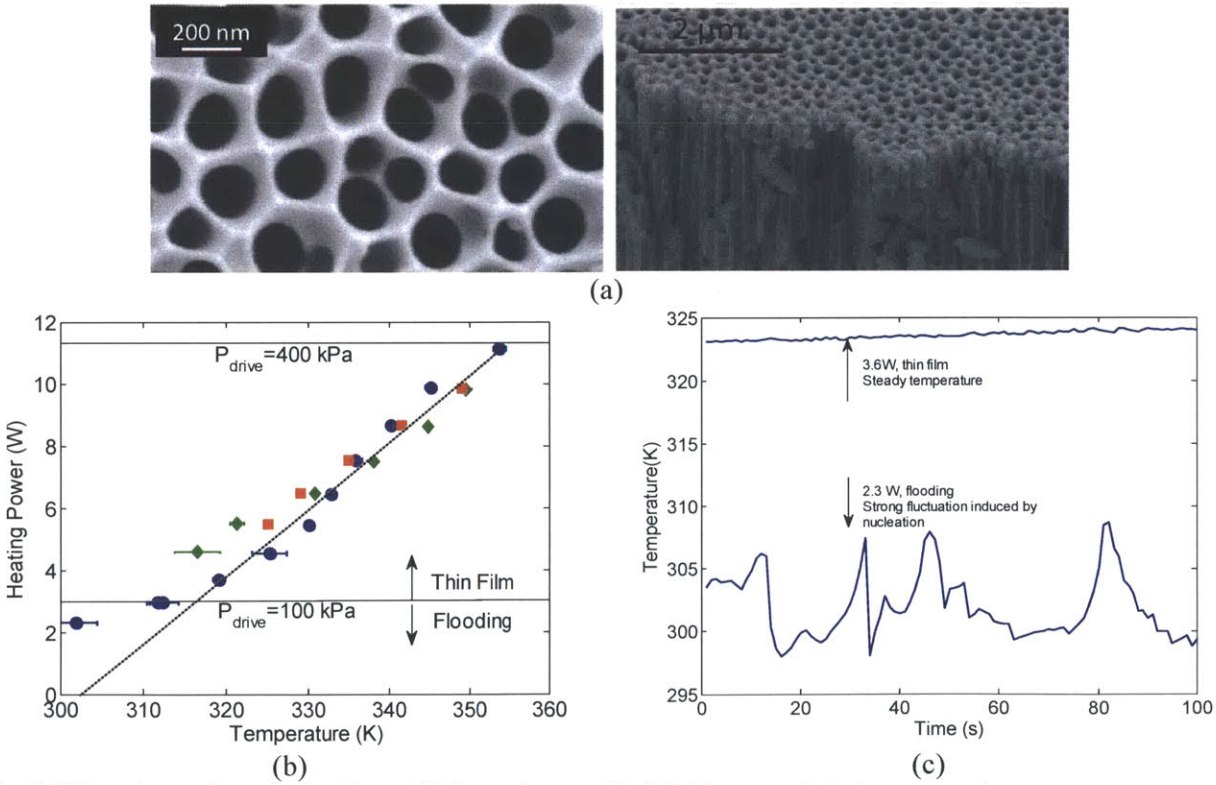

Fig. 4-8 Experimental results on 50 μm thick membranes. (a) SEM images of platinum coated nanoprous membranes with porosity of 24% and thickness of 50 μm. (b) Relation between dissipated power and temperature. The heat transfer coefficient was determined to be 1.8 W/cm^2K and the maximum interfacial heat flux was 96 W/cm^2. (c) Typical area-averaged temperature responses of flooding and thin film evaporation regimes over 100 seconds. The temperature fluctuations were large during flooding (≈15 K) with 2.3 W heating (bottom) and small (≈1 K) during thin film evaporation with ≈3.6 W heating (top)

Using the slope of the data points in the thin film region, the heat transfer coefficient can be determined as 1.8 W/cm^{2}K. Meanwhile, the maximum heating power before dry-out occurs is 11.6 W, yielding an interfacial heat flux of 11.6/0.12=96 W/cm^2. Therefore the maximum capillary pressure in the nanopores can be determined as ~300 kPa using the similar analysis as on 100 μm membranes. The pressure in the liquid near the menisci is ~-300 kPa. Note that the overall heat flux before dry-out is only ~23 W/cm^2 due to the porosity of 24%.

Note that during the experiments, the pressure in the chamber was kept very low (60 Pa~200 Pa) for efficient removal of the vapor to eliminate the thermal resistance associated with vapor transport. Such pressures are significantly lower than the saturation pressure based on the temperature of the membrane. Therefore, the liquid will evaporate due to the low pressure even without heating, called "flashing". The contribution of flashing can be estimated as follows.

For 100 μm thick membranes, the mass flux driven by the pressure difference without heating will be

$$\dot{m} = \frac{\dot{q}}{h_{fg}} = \frac{1.2}{7.33 \times 10^5} = 1.63 \times 10^{-6}\ kg/s \tag{4-5}$$

A fraction of this liquid flux will be evaporated while the other part will be cooled from the original temperature of the reservoir (22 °C) to the saturation temperature (-20 °C) corresponding to the chamber pressure (60 Pa). The sensible cooling of the liquid will provide the latent heat required for evaporation. As a result, the evaporation mass flux, m_{evp}, will satisfy

$$7.33 \times 10^5 m_{evp} = (22 + 20)(\dot{m} - m_{evp})C_p \tag{4-6}$$

where C_p is the specific heat of IPA. Therefore

$$m_{evp} = 2.5 \times 10^{-7} kg/s$$

The corresponding heat flux driven by flashing will be

$$\dot{q_{flh}} = 2.62\ W/cm^2$$

which is ~ 5% of the total maximum interfacial heat flux with heating.

For the 50 μm thick membranes, using a similar calculation method, the heat flux driven by flashing will be determined as $\dot{q_{flh}} = 5.92\ W/cm^2$, which is still ~ 5% of the maximum interfacial heat flux. In addition to modeling, a baseline experiment was performed where a graduated cylinder containing IPA is placed in the chamber pumped down to 60 Pa. The liquid will evaporate with decreasing rate as it cools down and eventually stops evaporating at the saturation temperature of -20 °C. At the beginning of the process, the fastest evaporation rate was found to be ~ 1mL/min with the opening area of the cylinder measured to be 6.4 cm^2. The evaporative heat flux was determined as 733×0.786/60/6.4=1.5 W/cm^2, which is on the same order with model estimations. Therefore, we can conclude the flashing of the liquid is not significant in contributing to the heat transfer of the total evaporation process.

To place the experimental results in context, we also developed a model based on energy conservation to demonstrate the potential of our proposed configuration to achieve high heat fluxes shown in Fig. 4-9. The permeability of the membranes, α, can be determined based on the

heating power and driving pressure at the transition between the flooding and the thin film regimes in the experiments: $\alpha = (\Delta P/L)/(q''/\rho h_{fg})$, where ΔP is the pressure difference across the membrane, L is the thickness of the membrane, $\dot{q}$ is the interfacial heat flux, ρ is the liquid density, and h_{fg} is the latent heat of the fluid. Therefore, the maximum interfacial heat flux is inversely proportional to the thickness of the membrane, $q'' = \rho h_{fg}\Delta P/\alpha L$, (solid lines in Fig.4). Using the experimentally determined permeabilities and capillary pressures of the 100 μm and 50 μm thick membranes, an upper and lower bound on the maximum interfacial heat fluxes were used due to the inevitable variability of the pore geometry during fabrication. The experimental results (diamond symbols) show good agreement with the model. If membrane thicknesses on the order of 1 μm were used, the maximum interfacial heat fluxes could be as high as 5000 W/cm^2 with overall heat fluxes over 1000 W/cm^2 even with membrane porosities of ≈24%.

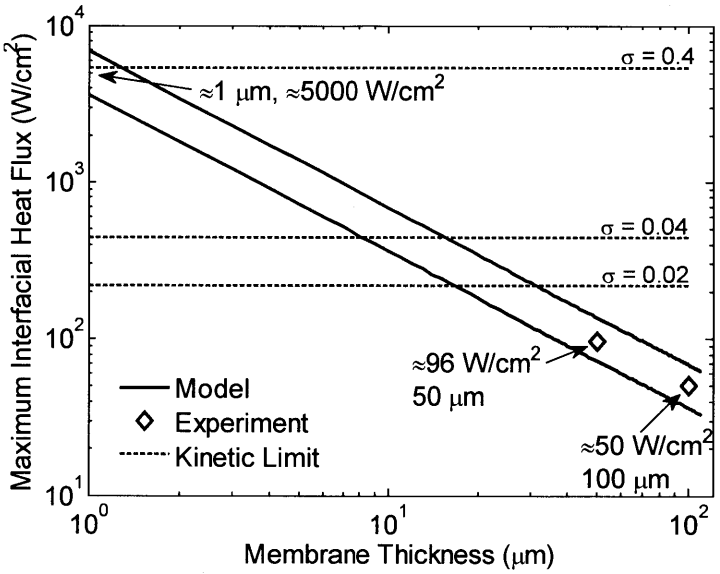

Fig. 4-9 Maximum interfacial heat fluxes dependent on both membrane thickness and accommodation coefficient. The inverse proportional relation between heat fluxes and thickness was validated by experimental results on 100 and 50 μm membranes. By reducing the thickness and choosing fluid with higher accommodation coefficient, interfacial heat fluxes as high as 5000 W/cm^2 could be achieved.

In previous experiments, the maximum heat fluxes are only limited by the supply of the fluid, which is true in relatively lower heat fluxes. Under very high heat fluxes, however, kinetic theory needs to be considered in determining the maximum allowed heat flux [80]. Based on kinetic theory, the maximum heat flux across the interface can be determined as

$$q_i'' = \frac{2\hat{\sigma}}{2-\hat{\sigma}} h_{fg} \sqrt{\frac{M}{2\pi R}} \left(\frac{p_{l,corr}}{\sqrt{T_l}} - \frac{p_v}{\sqrt{T_v}} \right) \quad (4\text{-}7)$$

where $p_{l,corr}$ is the corrected liquid pressure based on Kelvin's equation where the curvature of the meniscus is accounted for

$$p_{l,corr} = p_l \exp\left(-\frac{2\gamma_{lv} M}{r_p R \rho_l} \right) \quad (4\text{-}8)$$

and $\hat{\sigma}$ is the accommodation coefficient which describes the probability of a liquid molecule actually evaporates in contrast to reflect back to liquid phase. The value of the accommodation coefficient is highly sensitive to the purity of the system as well as the dynamic property of the fluid. For polar fluids such as ethanol, methanol, n-propyl alcohol, and water, the reported values of $\hat{\sigma}$ are typically 0.02 to 0.04. For very pure non-polar fluids, such as benzene or carbon tetrachloride, $\hat{\sigma}$ can be very close to 1 [81].

As shown in Fig. 4-9 with the membranes tested in previous experiments (50 μm and 100 μm thick), the interfacial heat fluxes were determined by the transport of liquid in the nanopores. The maximum demonstrated interfacial heat flux of 96 W/cm^2 is still well below the kinetic limit given accommodation coefficients in the range from 0.02 to 0.04. The results using the two kinds of membranes demonstrate the idea that the interfacial heat fluxes can be significantly enhanced by scaling down the membrane thickness. Considering the porosity of 24%, to dissipate heat flux over 1000 W/cm^2 would require interfacial heat fluxes as high as 5000 W/cm^2. Under such high heat fluxes, kinetic limit must be considered where ultra pure non-polar fluid with accommodation coefficients larger than 0.4 will be required as well as membrane thickness ~ 1 μm. However, aluminium oxide membranes with thickness smaller than 50 μm are very flimsy and cannot sustain the large pressure difference in the experiments. Future actual devices targeting heat fluxes above 1000W/cm^2 would need supporting structures to enhance the mechanical integrity of the thin membranes, as will be discussed in Chapter 7.

4.4 Conclusions

In this chapter, a novel configuration using thin film evaporation for high heat flux thermal management was proposed where liquid evaporates from nanopores in a thin membrane. In the proposed configuration, the capillary pressure is generated in the nanopores to drive the liquid supply while the viscous resistance is determined by supporting wicks with much large characteristic length. Such a design is able to overcome the limit of traditional microstructures used for thin film evaporation where capillary pressure and viscous resistance were determined by the same characteristic length scale.

Proof of concept experiments were performed to validate the proposed approach using nanoporous anodized aluminum oxide (AAO) membranes with thickness of 100 and 50 μm. Interfacial heat fluxes of 50 W/cm^2 and 96 W/cm^2 were demonstrated. Such heat fluxes are still below the prediction of kinetic theory and limited by liquid transport through the thick membranes. Approximately 300 kPa of capillary pressure was generated by the nanopores and a negative pressure of -300 kPa was achieved in the fluid near the meniscus. The maximum heat flux was found to be inversely proportional to the thickness of the membrane. By further scaling down the thickness of the membrane and using fluids with higher accommodation coefficients, heat fluxes on the order of 1000W/cm^2 can be achieved. Such systems hold significant potential in addressing thermal management challenges for advanced electronic devices.

In the experiments, there are a few technical challenges that need special care. First, the electrical contacts were realized by attaching thin copper foils to the metal layer *via* silver epoxy. With only 30 nm thick metal layer, the contact quality was not ideal. To address this problem, contact pads with metal thicknesses of 300 nm were deposited at the edge of the membrane. The copper foils were attached to those contact pads for better electrical properties. Secondly, after the pumping down process, the pressure difference between the chamber and the reservoir is very high. Therefore, the needle valve in the liquid feeding line needs to be opened slowly so that the working fluid could gradually fill the backside column and gently wet the membrane. Otherwise, the membrane could be broken by the water hammer effect.

Chapter 5 Pulsed Evaporative Transient Thermometry for Transient Heat Transfer Coefficient Measurement

5.1 Overview

The increase in power dissipation and reduction in size has proposed challenges in thermal management for a variety of semiconductor devices, including integrated circuits, laser diodes, and power electronic devices.[26, 27, 29] While several phase-change based cooling techniques, including microchannel flow boiling,[82-84] spray,[40, 41, 85] and jet-impingement,[39, 85, 86] have been investigated to address such challenges, thin film evaporation with liquid film thicknesses of $\approx$1 μm, is considered one of the most promising approaches to meet future demands.[16, 17, 87] Previous studies have showed that the heat transfer performance of thin film evaporation is highly dependent on the microscale liquid film morphology. For example, Rajan *et al.* have utilized various modeling tools to simulate and compare the heat transfer performance of different microstructures for thin film evaporation [88]. Various experimental approaches have been investigated to study the relation between meniscus shape and heat transfer behavior, such as IR camera imaging [89], and interference imaging [90]. However, those previous experimental investigations are generally steady state or slowly varying measurement where a constant heat flux was supplied and a steady temperature was measured. The average heat transfer coefficient was determined over a long period of time and compared with the imaging result. Such approaches are of practical merit where the actual application might desire steady state performance. But to fundamentally understand the correlation between the heat transfer coefficient and the configuration of liquid film, temporally resolved measurement of heat transfer coefficient during the whole evaporation process is of significant interest. In this paper, we present a metrology approach called Pulsed Evaporative Transient Thermometry (PETT) where the liquid is evaporated from micro/nanostructures by heat pulses. By analyzing the transient thermal response based on a lump system model, instantaneous thermal properties including heat capacity and heat transfer conductance (which is defined as the multiplication of heat transfer coefficient and surface area) can be determined. We applied this technique for the evaporation processes on two kinds of sample systems: copper microwires and nanoporous alumina membranes. For copper microwires, transient heat transfer conductance with a temporal resolution of 1 second was demonstrated. Distinctive heat transfer behaviors between oxidized and unoxidized surfaces were observed and compared with microscopic imaging. For nanoporous membranes, transient heat transfer coefficient of 0.2 seconds was demonstrated. A peak in heat transfer coefficient during the evaporation process was recorded which corresponds to the thin film evaporation state. This technique would be valuable for fundamental studies to relate wetting morphology and heat transfer behavior.

5.2 Experimental Setup and Modeling

The experimental setup for the PETT measurement is shown in Fig. 5-1a. The test micro device (microwire or nanoporous membrane) is connected to a reference resistor, which is stable against temperature change, and a function generator, which can provide electrical pulses with duration of 0.1~0.5 seconds and magnitude of 0.2~1 V. A small amount of liquid is applied to the test device. After the liquid deposition, the test device is heated up by the pulses and the thermal response causes a change in the voltage across the sample, which is recorded by a DAQ card (NI 6062E, National Instruments). The response of the samples is dependent on the heat capacity of the system and the heat transfer conductance, as shown by the model below.

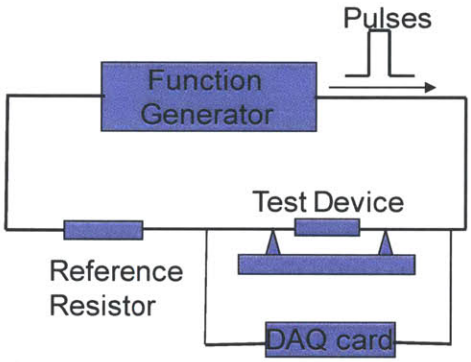

Fig. 5-1 Schematic showing the experimental setup for the PETT measurement. A small amount of liquid was deposited onto the surface of the test device, which is later heated by electrical pulses. The transient thermal response of the test device causes a change in the voltage across it, which is recorded by a DAQ card.

Given the small characteristic length scale of the micro devices, the system can be modeled as a lump system. When heated by a pulse, the response of the system is determined by

$$\frac{d(\Delta T)}{dt} + \frac{hA}{C}\Delta T = \frac{P}{C} \tag{5-1}$$

where h is the heat transfer coefficient, A is the surface area, hA is the heat transfer conductance, C is the heat capacitance of the micro device, and P is the heating power.
By solving Eqn (5-1), the temperature difference ΔT, as a function of time, t, is determined as

$$\Delta T = \frac{P}{hA}[1 - e^{-\frac{hA}{C}t}] \tag{5-2}$$

The resistance of the wire increases linearly with temperature as

$$\Delta R = \frac{\alpha P}{hA}[1 - e^{-\frac{hA}{C}t}] \tag{5-3}$$

where α is the temperature coefficient of resistivity.

Therefore, the temporal responses in the resistance of the micro devices are determined by the heat transfer conductance, hA, together with heat capacity, C. Figure 5-2a shows two typical responses. However, at the early stage of the resistance response (assuming $t \to 0$), the change in the resistance can be determined as

$$\Delta R \approx \frac{\alpha P}{hA} \cdot \frac{hA}{C} t = \frac{\alpha P}{C} t \tag{5-4}$$

The change in the resistance is approximately linear with time and the slope indicates the heat capacity, as shown in Fig. 5-2b.

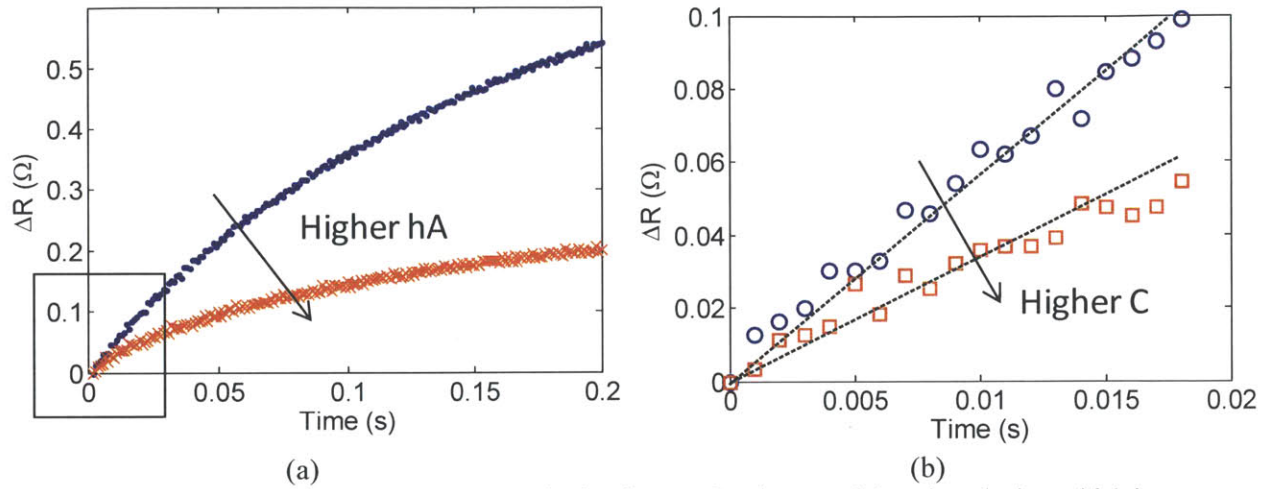

Fig. 5-2 Modeling of PETT. (a) Typical responses in the change of resistance of the micro device, which is determined by the heat transfer coefficient and the surface area. (b) Close look to the early stage of the response highlighted by the box in (a), where the heat capacity of the system can be inferred from the slope of the resistance increase.

Note that in the modeling, the heating power was assumed to be constant. In the actual experimental setup, a constant total voltage was applied on the reference resistance and the micro device. As the resistance of the device changes with temperature, the heating power changes slightly as well. The variation in the heating power can be estimated as

$$\frac{dP}{dT} = \frac{d}{dT}\left[\left(\frac{U}{R_f + R}\right)^2 R\right] = \frac{dR}{dT}\frac{1}{\left(R_f + R\right)^2}\left(1 - \frac{2R}{R_f + R}\right) \tag{5-5}$$

where R_f is the reference resistance and U is the total voltage. By choosing $R_f \approx R$, the variation in the heating power is negligible and the previous model stands for actual experiments.

5.3 Sample System I – Copper Microwires

We applied the PETT technique using thin copper wires as the first model system. Copper wires with diameter of 76 μm and length of about 3 inches (McMaster Carr) were used as the raw material. The copper wire was etched by iron(III) chloride solution so that the diameter is reduced to around 20 μm. After the etching, the copper microwire was surface oxidized by an oxidizer recipe which was demonstrated by Nam *et al.* to be capable of effectively increase the hydrophilicity of copper surface [91]. The scanning electron microscope (SEM) images of the oxidized surfaces are shown in Fig. 5-3a. From the SEM images, we can see that the oxidation

process significantly enhances both the micro and nanoscale roughness of the microwire surface.

The microwires are placed into the experimental setup in Fig. 5-1 and wetted by water. After the liquid deposition, a representative evaporation process on the oxidized wires was captured by a camera (Phantom V7.1, Vision Research Inc.) at a frame rate of 10 frames per second through a white light microscope (Eclipse LV-100, Nikon) with a 20x objective (NA = 0.60). The time lapse images are shown in Fig. 5-3b.

From the images we can see that the liquid droplet is pinned due to the enhanced roughness and hydrophilicity. The thickness of the droplet decreases during the evaporation process. Therefore, at the late stage of the evaporation, thin liquid films can be formed, as highlighted by the circle in Fig. 5-3b at the time t=12.5s. A peak in heat transfer conductance is expected corresponding to this thin film stage. The PETT measurement during the evaporation process is shown in Fig. 2c. Each heating pulse lasting for 0.2 seconds and there was 0.8 seconds time between pulses so that the sample could cool to the ambient temperature. As a result, the overall temporal resolution was 1 second. The heat capacity of the device decreases as liquid evaporated until a steady dry value was reached at the end of the experiment. The heat transfer conductance, hA, increased initially to reach a peak value and then decreased to the dry value towards the end of experiment, as expected.

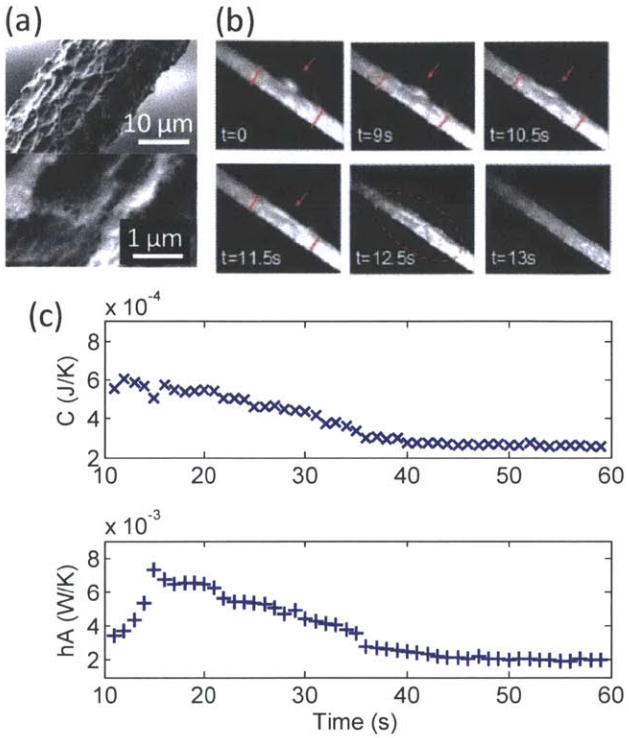

Fig. 5-3 PETT measurements on an oxidized copper wire system. (a) Scanning electron microscope (SEM) images of a typical oxidized copper wire. High roughness was observed. (b) White-light microscope image of typical evaporation process of a liquid droplet on the oxidized wire. Strong pinning of the droplet was observed, resulting a thin liquid film covering the surface at the late stage of evaporation (t=12.5s in this figure, bright reflection highlighted by the circle). (c) PETT measurement demonstrated time-resolved heat capacity (C) and heat transfer conductance (hA) on a wetted wire with temporal resolution of 1 second. A peak in the heat transfer rate was observed corresponding to the thin film stage.

For comparison, experiments were also carried out on copper microwires without surface oxidation. The SEM images of the un-oxidized copper wires are shown in Fig. 5-4a. The surfaces are smoother compared to the oxidized wires. Time lapse images of a representative evaporation process on the un-oxidized wires are shown in Fig. 5-4b. Due to the reduced roughness and consequently less pinning of droplets, the base area of droplets shrinks continuously during the evaporation process. We did not observe thin film stage. Accordingly, the time-resolved measurement of heat capacity and heat transfer conductance are shown in Fig. 5-4c. Similar with the oxidized wires, the heat capacity gradually decreased as water evaporated. However, the heat transfer conductance also decreased gradually and no peak was observed. The heat transfer behavior was distinctly different between the evaporation processes on oxidized and un-oxidized copper wires due to the difference in surface property and the liquid morphology.

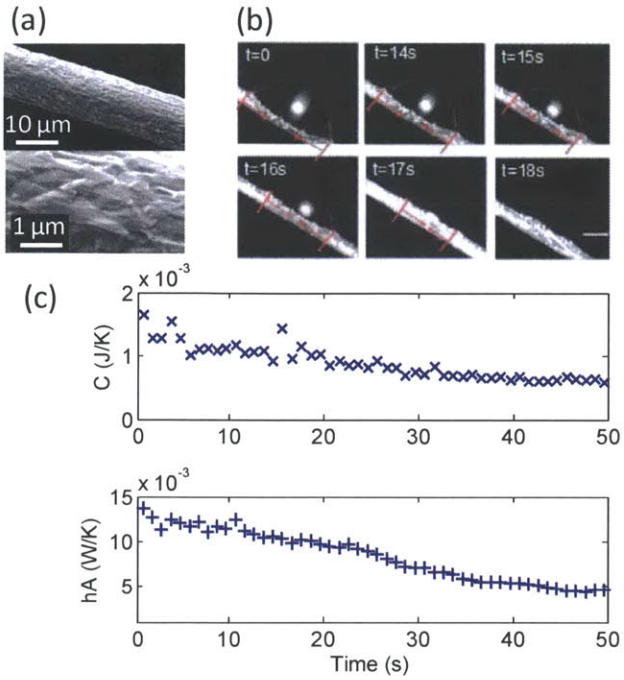

Fig. 5-4 PETT measurements on an unoxidized copper wire system. (a) Scanning electron microscope (SEM) images of a typical unoxidized copper wire. Smoother surface was observed compared to the oxidized surface. (b) White-light microscope image of typical evaporation process of a liquid droplet on the unoxidized wire. The wetted area shrinks gradually during the evaporation process. (c) PETT measurement demonstrated time-resolved heat capacity (C) and heat transfer conductance (hA) on a wetted wire with temporal resolution of 1 second. No peak in the heat transfer rate was observed without the thin film stage.

5.4 Sample System II – Nanoporous Aluminum Oxide Membranes

The PETT technique was demonstrated on alumina nanoporous membranes (Synkera Inc.) as the second model system. The average pore diameter of the membrane is 150 nm and thickness is 100 µm. A 30 nm thick layer of platinum was sputtered onto the membrane surface, which served as both the heater and an area-averaged temperature sensor. Images of the coated membrane are shown in Fig.5-5a. The membrane was wetted by isopropyl alcohol at the beginning of the experiments. A higher temporal resolution of 0.2 seconds was aimed using such membranes, where the heating lasted for 0.1 seconds and the cooling period between the pulses was also 0.1 seconds. With significantly shorter cooling period for this system, the temperature rise at the end of the heating pulse should be kept low to make sure the temperature of the membrane could drop to ambient at the beginning of next pulse. Typical responses to two pulses with different heat transfer conductance are shown in Fig. 5-5b, where noise are very strong compared to desired signal due to the low temperature rise. The noise mainly came from the data acquisition system. However, even with strong noise, distinctly different responses in the resistance were still observed for different heat transfer conductance.

The time-resolved heat transfer conductance measured by PETT is shown in Fig. 5-5c. Initially when the membrane was completely wetted and flooded with IPA, the heat transfer conductance was steady and low. As the evaporation occurred, a clear peak in heat transfer conductance was observed prior to dry-out which corresponds to the stage where the membrane was wetted by a liquid thin film. Later, as the thin liquid film was evaporated, the heat transfer coefficient decreases again, where natural convection and conduction loss through electrical contact became the only available heat transfer mode.

The maximum heat transfer conductance recorded was 3.6 W/K. However, as can be seen in Fig. 5-5b, with very high heat transfer coefficients at the thin film evaporation regime, the measured resistance change in the membrane was completely concealed by the noise in the DAQ acquisition. Therefore, the results of curve fitting are significantly influenced by the noise. Even though we were able to identify a peak in heat transfer conductance, the uncertainty is large and the peak value may not be reliable. Future work will be focused on improving the signal to noise ratio in the DAQ system to reduce the uncertainty so that the peak heat transfer conductance through thin film evaporation can be accurately captured.

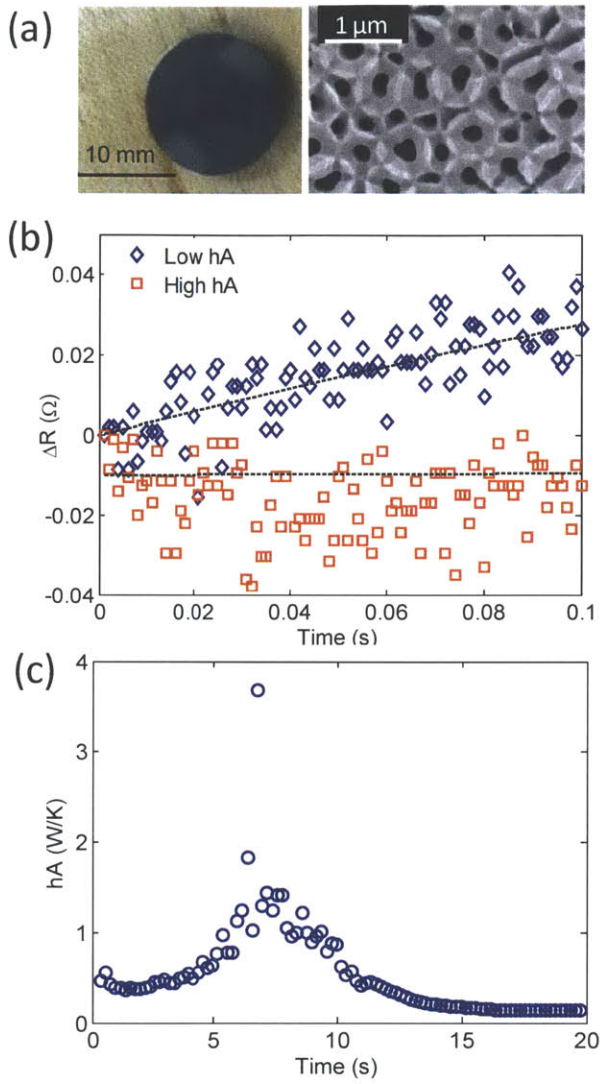

Fig. 5-5 PETT measurements on a nanoporous membrane system with temporal resolution of 0.2 seconds. (a) Imaging characterizations of the nanoporous membrane. The average pore diameter was 150 nm and a 40 nm thick platinum layer was deposited on the membrane. (b) Two example resistance change in response to the electrical pulses at low and high heat transfer conductance. The increase in the resistance was much smaller than the micro wire system due to the low heating power and short pulses. Noise in data acquisition caused high uncertainty. However, clear distinction in the responses can be observed between the two cases with different heat transfer conductance. (c) Time resolved heat transfer conductance. A strong peak was observed corresponding to the thin film stage during evaporation.

5.5 Conclusions

In this chapter, a new metrology technique, Pulsed Evaporative Transient Thermometry (PETT), was proposed where the transient thermal behavior can be measured. This technique utilizes short pulses to heat the sample and determines the instant thermal properties, including heat

capacity and heat transfer conductance by the transient response. We demonstrated the capability of this new approach to two sample systems: copper microwires with different surface treatment and nanoporous membranes. Distinct heat transfer behaviors were observed with temporal resolution of 1 second in combination with microscopic imaging on copper microwires. On nanoporous membranes, transient heat transfer coefficient with temporal resolution of 0.2 seconds was captured where a peak in heat transfer conductance was observed in the thin film evaporation stage. This approach can be extended to a variety of microstructures to improve the understanding of phase change heat transfer processes.

Chapter 6 Immersion Condensation on Oil-infused Heterogeneous Surfaces for Enhanced Heat Transfer

6.1 Overview

As discussed in Chapter 1, condensation plays an essential role in a wide variety of industrial applications including building environment [53], power generation [54], and water harvesting systems [55]. Enhancing condensation heat transfer has the potential to significantly improve the efficiency and reduce the cost of these applications. In order to maximize the heat transfer coefficient, however, an ideal condensation surface should simultaneously achieve three properties: low contact angle hysteresis to minimize droplet departure radii, low contact angle to reduce the conduction resistance of the droplet, and high nucleation density [61], as shown in Fig. 6-1. The model to quantify the effects of the three attributes was developed by Miljkovic et al. and can be referred in [61].

In practice, filmwise condensation, where a thin liquid film covers the surface, is the most prevalent condensation mode due to the high wettability of common heat transfer materials. However, the heat transfer coefficient is limited by the thermal resistance associated with the condensate film which insulates the surface [78]. Accordingly, efforts spanning eight decades have been devoted to achieving dropwise condensation on non-wetting surfaces where shedding droplets clean the surface for re-nucleation, leading to enhanced heat transfer rates [21, 22, 56-59]. One order of magnitude higher heat transfer coefficients compared to filmwise condensation have been reported using dropwise condensation [21, 57, 92]. Recent investigations have focused on creating chemically modified micro/nanostructured surfaces to achieve superhydrophobicity with the aim to further reduce the departure radii of droplets (Fig. 6-1(a)) [58, 59]. However, this focus on increasing the apparent hydrophobicity does not necessarily address the other two aspects influencing condensation heat transfer rates. The high apparent contact angles of condensing droplets on superhydrophobic surfaces lead to an increase in the conduction resistance through the droplet [20], hindering the overall heat transfer performance (Fig. 6-1(b)). Moreover, the hydrophobic surface chemistry increases the nucleation thermodynamic energy barrier, thus reducing the nucleation density and limiting the heat transfer coefficient (Fig. 6-1(c)) [93]. More recently, a composite surface has been proposed whereby a hydrophobic structured surface was infused with oil to simultaneously achieve easy droplet removal and low contact angles [62, 63]. While these works demonstrated significant potential for enhanced condensation surfaces, high nucleation densities are also desired along with these attributes to maximize heat transfer coefficients.

In this chapter, we will present a new approach to enhance condensation heat transfer using oil-infused structured surfaces with heterogeneous surface chemistry where droplets are allowed to nucleate immersed in the oil phase. The fabrication process of such a composite surface using

silicon micropillar arrays will be described first and then condensation experiments will be performed to show that nucleation density can be improved by over an order of magnitude compared to superhydrophobic surfaces without oil-infusion. Such increase will be explained as a combined effect of high-surface-energy sites in the heterogeneous coating and the reduced oil-water interfacial energy. After that, copper oxide nanostructured surfaces will be demonstrated as a scalable way to fabricate such composite surfaces and actual heat transfer coefficient will be measured to find approximately 100% enhancement compared to a dropwise condensation surface in the presence of non-condensable gases (NCG). Thus, these surfaces promise the development of a scalable approach for highly efficient condensation heat transfer for industrial, building energy, electronics cooling, and water-harvesting applications.

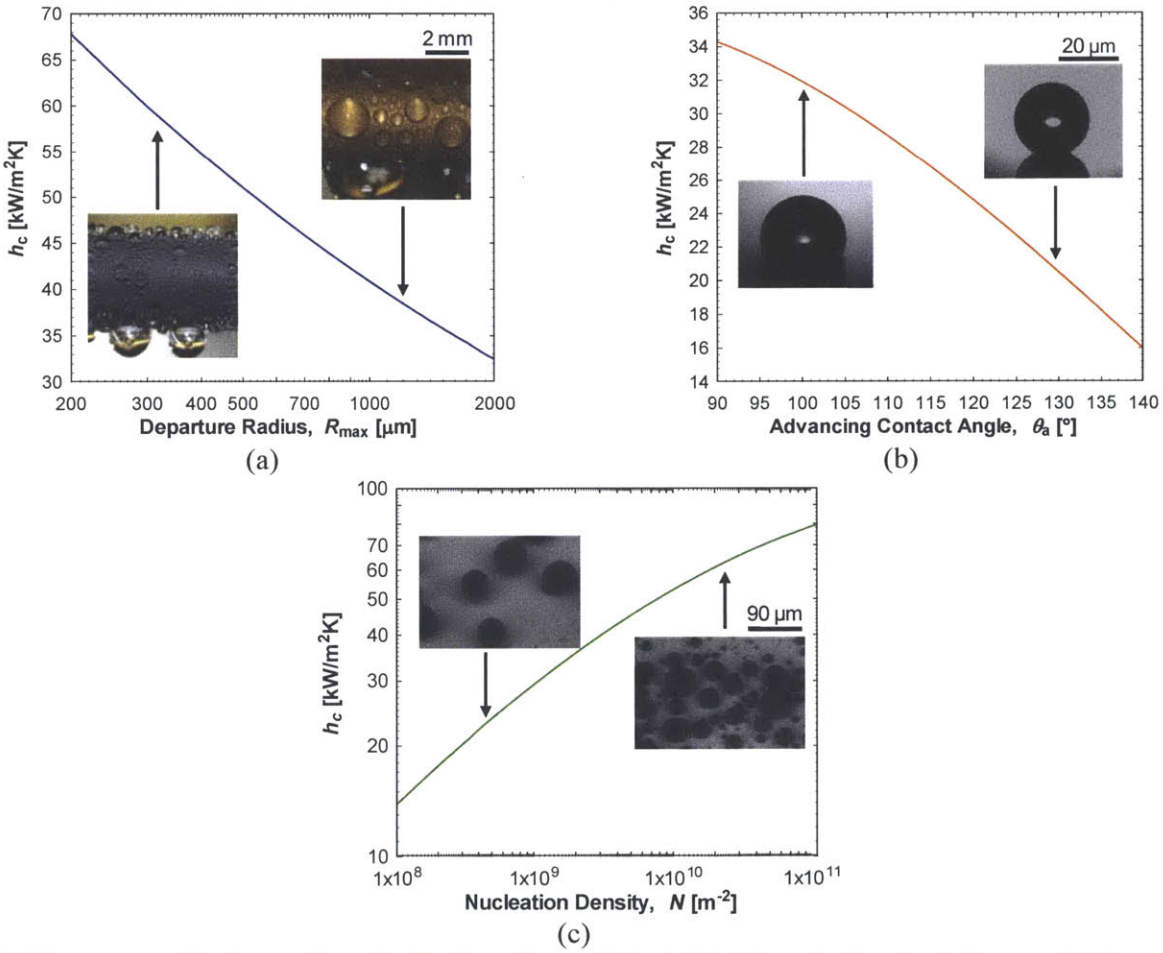

Fig. 6-1 Parameters affecting condensation heat transfer coefficient. Model results showing influence of: (a) departure radius with advancing contact angle θa = 110° and nucleation density N = 10^{10} m^{-2}, (b) advancing contact angle with nucleation density N = 10^{10} m^{-2} and departure radius Rmax = 800 μm, and (c) nucleation density with θa = 110° and Rmax = 800 μm. The results assume a vapor pressure of 2700 Pa and surface temperature of 20 °C.

6.2 Fabrication of Oil-infused Composite Surface

We first explain the key physics underlying immersion condensation using well-defined microstructured surfaces. To create the heterogeneous surfaces, we deposited a self-assembled coating (SAC) of (tridecafluoro-1,1,2,2-tetrahydrooctyl)-1-trichlorosilane (TFTS) from the vapor phase. The self-assembled coatings (SAC) were formed using a vapor deposition process. First, the silicon surface was cleaned using a Piranha solution (H2O2:H2SO4 = 1:3) to remove possible organic contamination and to create a large number of –OH bonds on the surface, which enables the bonding between silane molecules and the silicon surface. The samples were then placed in a desiccator (Cole-Palmer) together with a small petri dish containing ≈1 mL of the silane liquid. The desiccator was pumped down to ≈10 Pa. The pump was then shut off and the valve was closed so that the silane liquid could evaporate in the low-pressure environment of the desiccator and attach to the surfaces to form the SAC via the following reaction,

$$Si\text{-}OH + R\text{-}Si\text{-}Cl \rightarrow Si\text{-}O\text{-}Si\text{-}R + HCl$$

After 30 minutes of reaction, the desiccator was vented and the samples were rinsed using de-ionized (DI) water. The SAC coating method is capable of forming heterogeneity by agglomeration, as previously reported [94]. We chose the SAC method due to its simplicity and scalability, but alternative methods are also available to generate heterogeneity at the appropriate length scale, e.g., block copolymer or nano-imprinting [95, 96]. Height and phase atomic force microscope (AFM) images of the TFTS coating on a smooth silicon surface were obtained and are shown in Fig. 6-2(a) & (b), respectively, where the white spots are the nanoscale agglomerates of TFTS (≈200-500 nm in diameter). The phase angle of the agglomerates is significantly higher than that of the background, indicating that the agglomerates have higher surface energy [97]. We determined the local contact angle of the high-surface-energy agglomerates to be 60°± 1.5° by measuring the advancing and receding contact angle of a water droplet on the smooth, coated surface (θ_a/ θ_r = 122° ± 1.3°/78° ± 1.3°) and interpreting the data using a modified Cassie-Baxter model that incorporates the effect of local contact line deformation [98].

We fabricated silicon micropillar arrays with diameters, d, ranging from 0.4 μm to 5 μm, periods, l, ranging from 4 μm to 25 μm, and heights, h, ranging from 10 μm to 25 μm using contact lithography and deep reactive ion etching (DRIE) processes. The geometries were chosen to satisfy the imbibition condition to enable oil spreading [14] and stabilize the oil film. The pillar surfaces were subsequently functionalized with the TFTS SAC, and infused with a fluorinated oil, Krytox GPL 100. The low surface tension of Krytox oil (≈17-19 mN/m) allowed it to spread on the surface and form a stable film via capillarity. A dry N2 stream was used to assist spreading and remove excess oil. Typical scanning electron microscope (SEM) images of the coated pillar

arrays without and with the oil-infusion are shown in Fig. 6-2(c) & (d), respectively. On these TFTS-coated pillar arrays, the advancing and receding contact angles without oil-infusion were $\theta_a/\theta_r = 139° \pm 3°/128° \pm 3°$, whereas those with oil-infusion were $\theta_a/\theta_r = 110° \pm 2°/107° \pm 2°$ (Fig. 6-2(e) & (f)). Such low contact angle hysteresis is a key attribute allowing droplets to be removed with a small departure radius under the action of gravity during condensation [62, 63, 99].

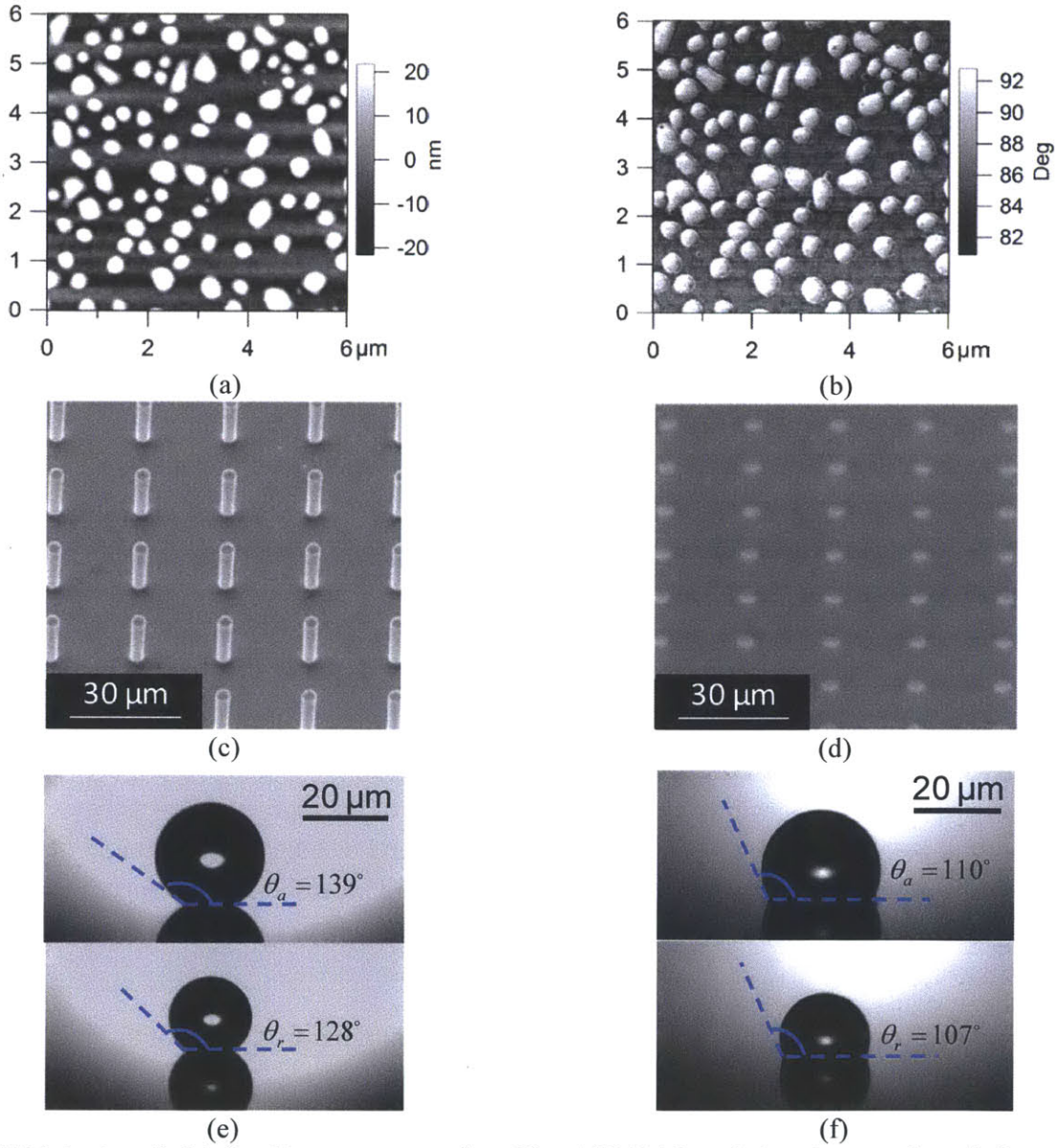

Fig. 6-2 Fabrication of oil-infused heterogneous surface. (a) and (b) Height and phase images of atomic force microscope (AFM) images of TFTS ((Tridecafluoro-1,1,2,2-tetrahydrooctyl)-1-trichlorosilane) coating. The higher phase angle at the nanoagglomerates indicates local higher surface energy. (c) and (d) Scanning electron microscope (SEM) images of TFTS-coated micropillar arrays before and after the oil-infusion. (e) and (f) Contact angle hysteresis on a superhydrophobic surface without and with oil-infusion. The hysteresis is ≈3° on the oil-infused surface with contact angle ≈110°. The microstructure geometries were the same on both surfaces, with diameter of 5 μm, height of 20 μm, and period of 15 μm.

6.3 Increased Nucleation Density on Composite Surface

We investigated the nucleation behavior on the surfaces with and without the oil under white light optical microscopy (OM). The samples were horizontally mounted on a thermal stage [Instec Inc.] inside an enclosure and cooled to $T_w = 283.1 \pm 0.1$ K in a dry nitrogen atmosphere. Following thermal equilibration (~ 5 min), nucleation was initiated by flowing water-saturated nitrogen into the enclosure. The supersaturation, defined as the ratio of the vapor pressure to the saturation pressure at the stage temperature (p_v/p_w), was controlled by the temperature of the water reservoir through which the nitrogen carrier gas was sparged and measured using a humidity probe (Hygroclip, Rotronic) located ~1 cm above the sample. Typical values of the supersaturation were around $S \approx 1.6$. The nucleation density and subsequent growth behavior was recorded at a frame rate of 30 fps using a CMOS camera (Phantom V7.1, Vision Research) attached to the optical microscope. As shown in Fig. 6-3(a) and (b), nucleation was not observed on the surface without oil-infusion but seen on almost every tip of the pillars after oil-infusion (nucleation density $N = l^{-2} = 4.4\times10^9$ m^{-2}). Nucleation in the space between the pillars was not observed due to the large thickness of oil coverage that limits water vapor diffusion to the SAC. Meanwhile, nucleation on the oil/vapor interface did not occur due to the low surface energy compared to the high-surface-energy sites in the SAC.

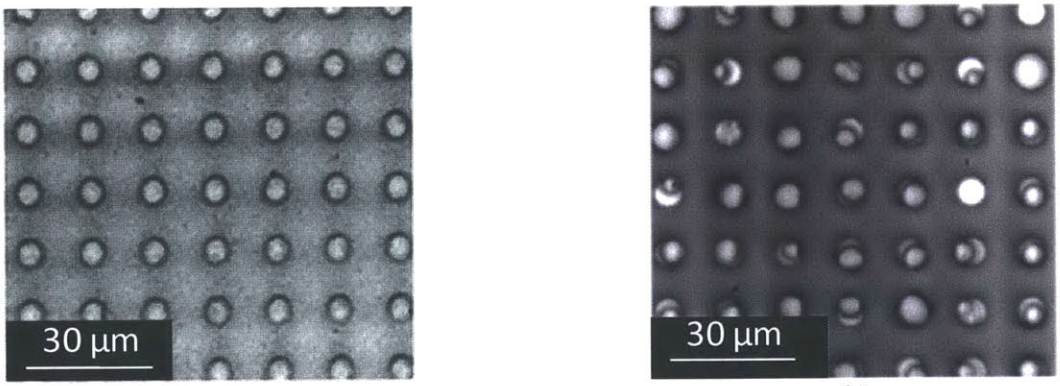

(a) (b)

Fig. 6-3 White-light optical microscope images of condensation on micropillar arrays (a) before and (b) after oil-infusion. The micropillar geometries were the same as in Fig. 6-2 (e) and (f). The supersaturation in the experiments was $S = 1.6$.

The increase in nucleation density observed on the oil-infused TFTS surfaces was achieved *via* the combination of the high-surface-energy sites and lower water-oil interfacial energy. The nucleation rate, J, can be determined by classical nucleation theory (CNT) as [93]

$$J = zf^* \exp(-G^*) \tag{6-1}$$

In Eqn. (S13), z is the Zeldovich factor and G^* is the dimensionless energy barrier, given by

$$z = (kT \ln S)^2 / 8\pi v_o \sqrt{kT\psi(\theta)\gamma^3} \tag{6-2}$$

$$G^* = 16\pi\psi(\theta)v_o^2\gamma^3/3(kT)^2\,(\ln S)^2 \quad (6\text{-}3)$$

where S is the supersaturation and $\psi(\theta)$ is the activity that accounts for the effect of contact angle. f^* is the frequency of monomer attachment to the critical droplet nucleus dependent on the nature of the nucleus growth. The main modes of growth during heterogeneous nucleation are limited *via* direct impingement of monomers to the nucleus or surface diffusion [100, 101].

The frequency of monomer attachment due to direct vapor impingement is given by

$$f^*_i = \gamma_n[(1-\cos(\theta_w))/2\psi^{2/3}(\theta)](36\pi v_o^2)^{1/3}In^{2/3} \quad (6\text{-}4)$$

where γ_n is the sticking coefficient ($0 < \gamma_n < 1$), I is the classical Hertz-Knudsen impingement rate ($I = P/\sqrt{2\pi m_o kT}$), n is the number of molecules in the nucleated cluster, and v_o is the volume of an individual water molecule ($v_o = 3 \times 10^{-29}$ m^3). To determine an upper bound on the nucleation rate, a sticking coefficient of one was assumed ($\gamma_n = 1$).

The frequency of monomer attachment due to surface diffusion is given by

$$f^*_{sd} = \gamma_n c^* \lambda_s^{\,2} I \quad (6\text{-}5)$$

where c^* is the capture number due to surface diffusion ($1 < c^* < 5$), and λ_s is the mean surface diffusion distance of an adsorbed monomer on the substrate. The capture number c^* is size independent and approximately equal to 1.9 for heterogeneous condensation of water vapor [102]. The mean surface diffusion distance is dependent on the wettability of the substrate and is given by $\lambda_s = \sqrt{D_{sd}\tau_d}$ where D_{sd} is the surface diffusion coefficient ($D_{sd} = d_s^{\,2}\nu_s \exp[-E_{sd}/kT]$), τ_d is the desorption time ($\tau_d = (1/\nu_s)\exp[-E_{des}/kT]$), ν_s is the adsorbed molecule vibration frequency determined using the Debye approximation ($\nu_s = V_D a/2$), d_s is the length of a molecular jump along the substrate surface approximated by the lattice constant of the substrate ($d_s = 5.4$ Å) [103] and V_D is the speed of sound in the substrate ($V_D = 8433$ m/s). The desorption and surface diffusion energies are given by $E_{des} = E_1 + \sigma_{sv}a_o$ and $E_{sd} = 0.5E_{des}$ [104], respectively, where E_1 is the binding energy of an $n = 1$ sized cluster, σ_{sv} is the solid-vapor interfacial energy and a_o is the water molecule surface area ($a_o = 4.67 \times 10^{-19}$ m^2). The calculated energies of desorption show excellent agreement with that of the experiments and molecular dynamics simulations ($E_{des,SiO2} = 0.9$ eV) [105, 106].

By adding the nucleation rate from the two mechanisms together, the nucleation rate, J, can be determined as a function of the contact angle and interfacial energy of the condensate at given supersaturations.

On the oil-infused surface, the tips of the pillars were covered by oil due to its low surface tension. However, the tips were still visible in the SEM images (Figures 6-2c and d) because of the small thickness of the oil film. In these regions, with a supersaturation of $S = 1.6$, the water vapor is able to diffuse through the thin oil layer and form nuclei *immersed* in the oil layer on the high-surface-energy sites. Nucleation is thermodynamically favored in this configuration due the

reduced interfacial energy between water and oil (≈49 mJ/m^2) compared to that between water and vapor (≈72 mJ/m^2). Note that the contact angle of 60° ± 1.5° was determined without the introduction of oil. The actual contact angle of nuclei on the high-surface-energy domains with the existence of oil can be bounded in the range from 43° to 67° using Young's equation, as follows. As shown in Fig. 6-4(a), on a high-surface-energy domain of the TFTS coating without oil-infusion, the local contact angle of a water droplet on a surface, $\theta_{ws(v)}$, can be determined using Young's equation as

$$cos\theta_{ws(v)} = \frac{\sigma_{vs} - \sigma_{ws}}{\sigma_{wv}} \tag{6-6}$$

where σ_{vs} is the interfacial energy between the surface and vapor, σ_{ws} is the interfacial energy between water and the surface, and σ_{wv} is the interfacial energy between water and vapor, which is 72 mJ/m^2.

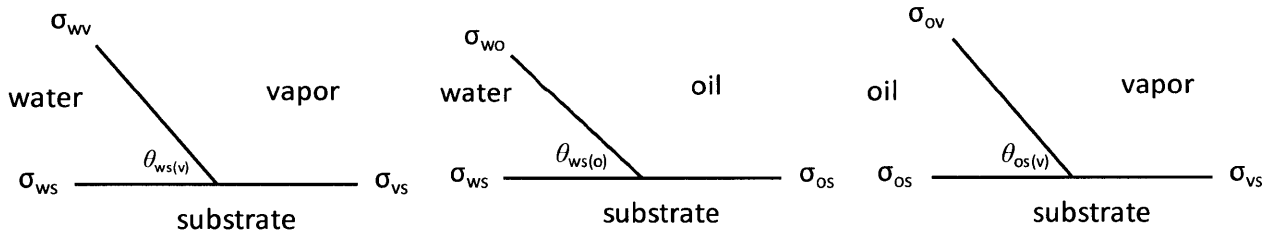

(a) (b) (c)

Fig. 6-4 Schematics showing the relations between interfacial energies and contact angle using Young's equation for (a) water-vapor-substrate, (b) water-oil-substrate, and (c) oil-vapor-substrate systems.

Similarly, with the introduction of oil which surrounds the water droplet on a surface, the local contact angle, $\theta_{ws(o)}$, can be determined as

$$cos\theta_{ws(o)} = \frac{\sigma_{os} - \sigma_{ws}}{\sigma_{wo}} = \frac{\sigma_{os} - \sigma_{vs} + \sigma_{vs} - \sigma_{ws}}{\sigma_{wo}} \tag{6-7}$$

where σ_{os} is the interfacial energy between the surface and oil, σ_{ws} is the interfacial energy between water and the surface, and σ_{wo} is the interfacial energy between water and oil, which is 49 mJ/m^2.[62]

Since σ_{os} is experimentally difficult to obtain for our system, we provide bounds for the local contact angle for the water-oil-substrate system, $\theta_{ws(o)}$, as follows. We consider the contact angle of oil on the high-surface-energy domain using

$$cos\theta_{os(v)} = \frac{\sigma_{vs} - \sigma_{os}}{\sigma_{ov}} \tag{6-8}$$

where σ_{ov} is the interfacial energy between vapor and oil, which is 17 mJ/m^2. Since the oil wets the TFTS-coated surface, which means $\theta_{os(v)}$<90°. Therefore, we can determine that $0<\sigma_{vs} - \sigma_{os}<17$ mJ/m^2.

As a result, the local contact angle of the water droplet on a surface surrounded by oil can be bounded as

$$cos\theta_{ws(o)} = \frac{\sigma_{os} - \sigma_{vs} + \sigma_{vs} - \sigma_{ws}}{\sigma_{wo}} \in \left(\frac{-17+36}{49}, \frac{0+36}{49}\right) \quad (6\text{-}9)$$

$$\therefore \theta_{ws(o)} \in (43°, 67°)$$

Accordingly, as shown in Fig. 6-5, assuming a local contact angle lower than 67°, the predicted nucleation rate increases from 0.2 $m^{-2}s^{-1}$ to greater than 10^{14} $m^{-2}s^{-1}$ due to the encapsulating oil phase in comparison with the same surface without oil-infusion. The predicted nucleation rate is orders of magnitude larger than the density of the high-surface energy domains. As a result, multiple nuclei could form on each tip of the pillars where the oil layer is thin enough for effective vapor diffusion but they grow and coalesce into a single droplet large enough to be visualized under a microscope. Therefore, we only observed an order of magnitude increase in the total nucleation density, which is equal to the density of the pillars, as shown in Fig. 6-3(b).

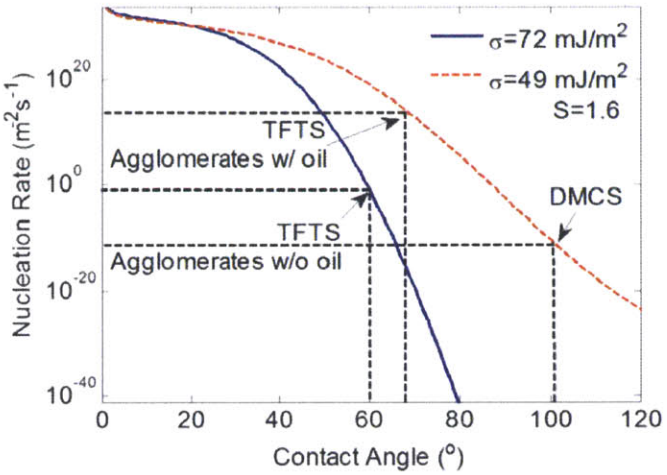

Fig. 6-5 Nucleation rates predicted as a function of contact angle and interfacial energy. At supersaturation of 1.6, the reduction in oil-water interfacial energy and contact angle below 67° increase the nucleation rate to 10^{14} $m^{-2}s^{-1}$. With only reduced interfacial energy, the nucleation rate is predicted to be lower than 10^{-20} $m^{-2}s^{-1}$ on homogeneous hydrophobic coatings. With contact angle around 60° without oil-infusion, the nucleation rate is predicted to be 0.2 $m^{-2}s^{-1}$.

In order to further validate our theory, we performed control experiments on various surface coatings. Two homogeneous hydrophobic coatings: Dimethyldicholorosilane (DMCS) and Poly(1H, 1H, 2H, 2H-perfluorodecyl acrylate) (PFDA) were studied in our control experiments. DMCS can be deposited on silicon surfaces using the vapor deposition process as described in the Methods section. PFDA was deposited using an initiated chemical vapor deposition process (iCVD) [107]. The thickness of the PFDA polymer is around 35 nm.

Atomic force microscope (AFM) images of flat silicon surfaces coated by DMCS and PFDA are shown in Fig. 6-6a & b, respectively. The DMCS and PFDA coatings were found to be homogeneous. The advancing and receding contact angles on DMCS and PFDA coated surface were measured to be $\theta_a/\ \theta_r$ = 103.8° ± 0.5°/102.7° ± 0.4° and $\theta_a/\ \theta_r$ = 121.1° ± 2.2°/106.3° ± 2.4°, respectively. The hysteresis was significantly lower compared to TFTS-coated surfaces, which also indicates the homogeneity of DMCS and PFDA coatings.

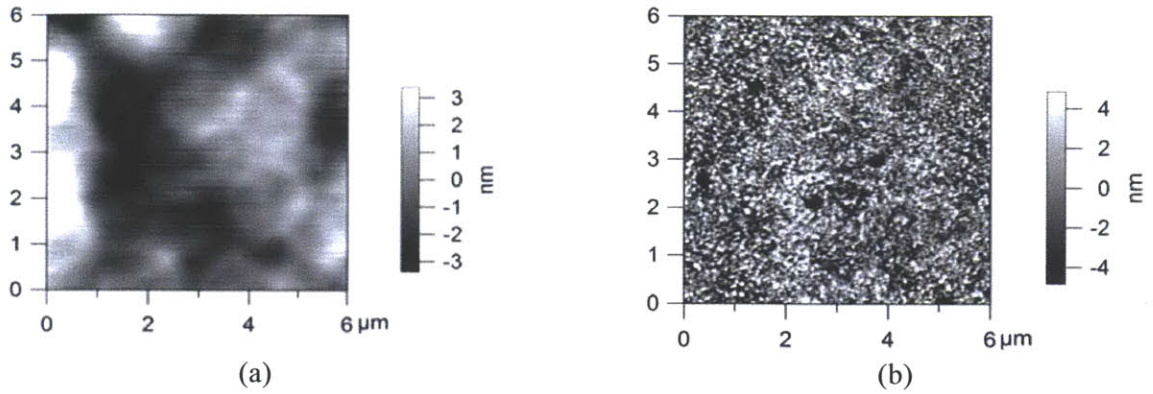

Fig. 6-6 AFM images of (a) DMCS and (b) PFDA coatings on a flat silicon surface. The surfaces were found to be homogeneous.

Condensation experiments were performed on micropillar arrays coated with DMCS and PFDA with and without oil-infusion using the same experimental setup as described in the Methods section. The results are summarized and compared to the TFTS-coated surface in Fig. 6-7. The nucleation density was normalized against the density of pillars for a fair comparison between different geometries. The nucleation density increase was not observed on DMCS and PFDA coated surfaces even after oil-infusion, as predicted by classical nucleation theory. Note that classical theory predicted nucleation rates as low as 0.2 $m^{-2}s^{-1}$ on TFTS-coated surfaces without oil-infusion. However, in our experiments, we observed some nucleation as shown in Figure 6-6. Repeated condensation experiments showed that nuclei formation and droplet pinning occurred on identical spots for each subsequent test, indicating that the spots are defects in the SAC coating where the hydrophilic silicon oxide surface (contact angel $\theta = 38°$) was exposed. Such defects, while limited in number, act as nucleation sites for condensation.

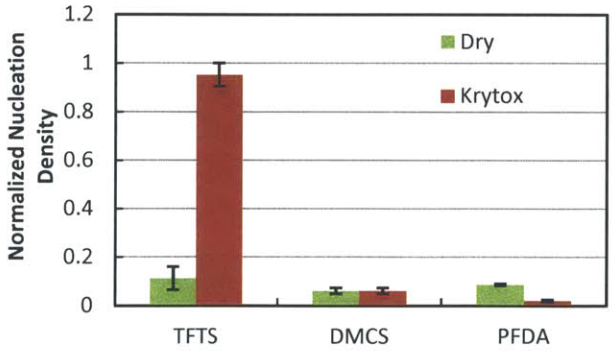

Fig. 6-7 Summary of nucleation density on various surfaces. The increase in nucleation density was only observed on oil-infused surfaces with TFTS coatings. The nucleation densities were normalized against pillar density for a fair comparison across different sample geometries.

An additional silane coating, 3-(trimethoxysilyl)propyl methacrylate (3-TMPM), was also tested. The advancing and receding contact angle of water on a smooth silicon surface coated with 3-TMPM are 65° ± 1.5° and 53°± 1.1°, respectively. The contact angle is in the range where the nucleation rate will be almost zero with a surface tension of 72 mN/m and nucleation should occur on every tip of pillars with an interfacial tension of 49 mN/m. Optical images of the

condensation experiments are as shown in Fig. 6-8. Similar to the behavior of TFTS-coated surface, a significant increase in nucleation density was observed with the addition of Krytox oil as expected. This result supports well our hypothesis related to the role of the hydrophilic nanoagglomerates in the droplet nucleation process.

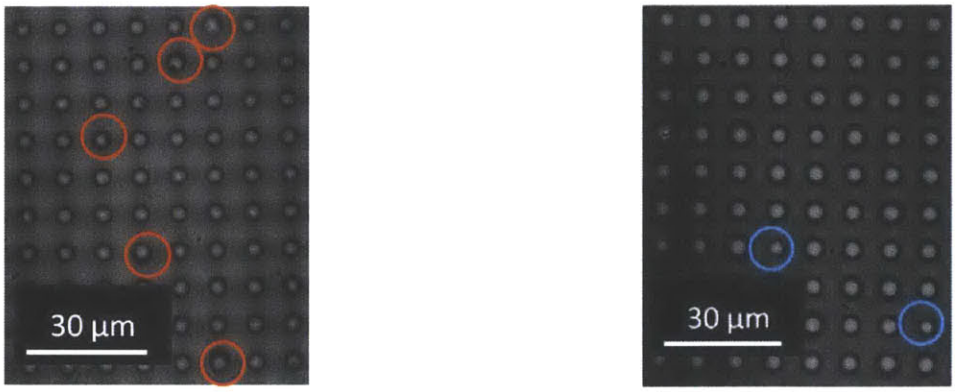

(a) (b)

Fig. 6-8 Condensation behaviors on 3-TMPM coated micropillar arrays (a) without and (b) with Krytox oil-infusion. The nucleation density was low in (a) as highlighted by the red circles. Meanwhile, nucleation occurred on almost every tip of the pillars in (b), where pillar tips *without* nucleation were highlighted by blue circles.

6.4 Heat Transfer Enhancement on Composite Surface

With the physical insights gained from these studies, we performed experiments to demonstrate heat transfer enhancement on scalable surfaces for practical applications. We investigated oil-infused copper oxide (CuO) nanostructures functionalized with TFTS, which promises a scalable, low cost platform for condensation surfaces. We used commercially available oxygen-free Cu tubes (99.9 % purity) with outer diameters, D_{OD} = 6.35 mm, inner diameters, D_{ID} = 3.56 mm, and lengths L = 131 mm as the test samples for the experiments. Each Cu tube was cleaned in an ultrasonic bath with acetone for 10 minutes and rinsed with ethanol, isopropyl alcohol and de-ionized (DI) water. The tubes were then dipped into a 2.0 M hydrochloric acid solution for 10 minutes to remove the native oxide film on the surface, then triple-rinsed with DI water, and dried with clean nitrogen gas.

Nanostructured CuO films were formed by immersing the cleaned tubes into a hot (96 ± 3 °C) alkaline solution composed of $NaClO_2$, NaOH, $Na_3PO_4 \cdot 12H_2O$, and DI water (3.75 : 5 : 10 : 100 wt.%). During the oxidation process, a thin (< 200 nm) Cu_2O layer was formed that then re-oxidized to form sharp, knife-like CuO oxide structures with heights of $h \approx 1$ μm, solid fraction[108] $\varphi \approx 0.023$ and roughness factor[108] $r \approx 10$. To verify the independence of oxide thickness on chemical oxidation time,[109] four separate samples were made using oxidation times, τ = 5, 10, 20, and 45 minutes.SEM images of representative copper oxide nanostructures without and with Krytox oil-infusion are shown in Figure 6-9a and b, respectively. Condensation experiments were performed on the CuO surfaces without and with oil-infusion in an environmental SEM. Figures 6-9c & d show an order of magnitude increase in nucleation density

on the oil-infused surface, as observed on the silicon-based microstructures. To capture the condensation heat transfer behavior, we formed the oil-infused heterogeneous CuO surfaces on copper tubes. Figures 6-9e and f show condensation on a typical hydrophobic surface and an oil-infused heterogeneous surface, respectively. Significantly higher droplet density was observed on the oil-infused surface while a low departure radius of approximately 0.5 mm was maintained.

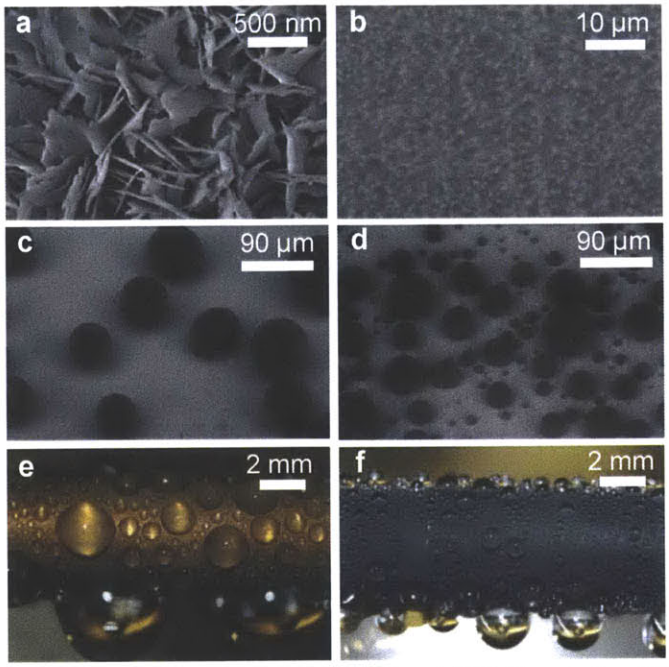

Fig. 6-9 Copper oxide (CuO) surfaces for immersion condensation. (a) Field emission SEM (FESEM) image of CuO nanostructures. (b) Environmental SEM (ESEM) image of CuO nanostructures infused with Krytox oil. (c) ESEM image of nucleation on TFTS-coated CuO surface. (d) ESEM image of oil-infused TFTS-coated CuO surface. An order of magnitude higher nucleation density was observed compared to (c). (e) Image of dropwise condensation on a hydrophobic copper tube surface. (f) Image of condensation on an oil-infused TFTS-coated CuO surface. Significantly higher droplet density was observed on the oil-infused surface while a low departure radius of approximately 0.5 mm was maintained.

Overall heat transfer coefficients were measured to evaluate the performance on the different CuO-based surfaces (Figure 6-10). We introduced non-condensable gases (NCGs) in the experiments to emulate practical applications, where NCGs inevitably exist and significantly affect the condensation heat transfer performance. NCG (air) with a partial pressure of 30 Pa was supplied into the test chamber with vapor pressures ranging from 2 to 3 kPa ($1 < S < 1.6$). Three kinds of surfaces were tested in these conditions: a hydrophobic surface for typical dropwise condensation (DHP), a superhydrophobic TFTS-coated copper oxide surface (SHP), and a Krytox oil-infused, TFTS-coated CuO surface. The test samples, 6.35 mm diameter tubes with different surface treatments, were placed in an environmental chamber (Kurt J. Lesker) for the heat transfer measurements. A water reservoir, which was connected to the chamber *via* a vapor valve, was heated to > 95°C to produce steam. The vapor valve was opened to allow steam to flow into the chamber after the chamber was pumped down to the targeted non-condensable pressure (≈30 Pa). Chilled water flowed along the inside of the tube where the inlet temperature

and outlet temperature were both measured by thermocouples so that the heat flux could be determined by the temperature rise. The temperature difference, ΔT was determined as the log-mean temperature difference (LMTD) between the vapor and the chilled water. Each data point in Figure 6-9 was determined over 10 minutes of steady state operation. The vapor inflow valve was then adjusted to change the vapor pressure in the chamber. While the SHP surface is more hydrophobic than the DHP surface, flooding and strong pinning of condensate was observed, leading to similar heat transfer coefficients with the DHP surfaces. On the Krytox oil-infused TFTS-coated CuO surface, approximately 100% improvement in heat transfer coefficient was demonstrated over the entire range of supersaturations tested. This result highlights the collective role of enhanced nucleation density, more frequent droplet removal, and lower droplet contact angle (Figure 6-1).

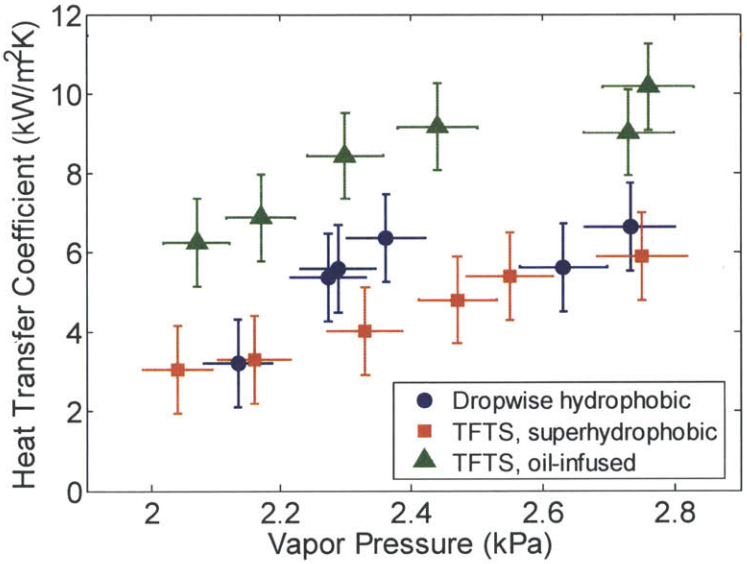

Fig. 6-10 Comparison of overall heat transfer coefficient during condensation on a hydrophobic surface, a TFTS-coated superhydrophobic surface, and an oil-infused composite surface with 30 Pa of non-condensable gases. The supersaturation was varied in the range $1<S<1.6$. The heat transfer coefficient on the oil-infused surface increased by approximately 100% compared to the dropwise and superhydrophobic surfaces.

6.5 Conclusions

In summary, we observed over an order of magnitude increase in the nucleation density on hydrophobic silicon pillar arrays coated with a long-chain silane molecule when hydrophobic oil was introduced on the surface. AFM imaging revealed the existence of locally hydrophilic agglomerates despite the overall hydrophobicity of the silane self-assembled coating (SAC). The increased nucleation density is explained in the context of classical nucleation theory as the combined effect of the hydrophilic sites and the reduction in interfacial energy between water and oil. Control experiments on silicon pillar arrays with hydrophobic coatings without micelles and hydrophilic coatings were performed to support our findings. Approximately 100% enhancement in heat transfer coefficient was demonstrated on oil-infused copper oxide surfaces. This work shows new possibilities in heat transfer enhancement using immersion condensation.

For practical implementation of this approach, however, further work is needed in tailoring oil and coating properties, as well as surface geometry to minimize oil loss during operation and maximize condensing surface area. With continued development, immersion condensation promises to be a near-ideal condensation mode for a variety of heat transfer and resource conserving applications.

Chapter 7 Conclusions and Outlook

7.1. Summary of Work

Micro/nanostructures have long been recognized as able to enhance heat transfer performance in phase-change processes by achieving extreme wetting properties. This thesis focused on two areas involving such capability of micro/nanostructures: thin film evaporation using superhydrophilic surfaces and immersion condensation on superhydrophobic surfaces.

On superhydrophilic surfaces, we first discussed the liquid transport driven by capillarity in micropillar arrays as a model system, which is essential in thin film evaporation processes. The propagation rates were determined based on the balance between capillary pressure and viscous resistance. We simulated the shape of meniscus, which was corroborated with interference measurements, to accurately obtain the capillary pressure as a function of the pillar geometries. The viscous resistance was determined using Brinkman's equation which incorporates the effect of the substrate and the sidewall of the pillars. Propagation experiments were carried out to validate the model where good agreement was observed on pillar arrays with high aspect ratios. Design guidelines were proposed for optimized pillar geometries to achieve maximized propagation rates.

On pillar arrays with smaller aspect ratio and large spacing between pillars, however, the propagation rates deviated from model prediction. Two distinct time scales were observed in such geometries where the liquid front sweeps between the pillars before filling a unit cell in the array, which significantly decreases the overall propagation rate. The sweeping distance scales with $1/5^{th}$ power of time and such scaling was explained by approximating the liquid front with a second order polynomial. The effect of the sweeping process on the overall propagation rate was quantified and validated with experiments.

With improved understanding of the liquid transport across the microstructured surface, we proposed a new configuration using nanoporous membranes for thin film evaporation to achieve high heat fluxes by decoupling the capillarity and viscous resistance. We used anodized aluminum oxide (Al_2O_3) membranes with average pore diameter of 150 nm and thicknesses of 50 and 100 μm to demonstrate the concept. A 30 nm thick layer of platinum was deposited on the surface of the membrane as heater and temperature sensor. Isopropyl alcohol as a coolant was supplied from the bottom and driven through the membrane by capillarity. Maximum interfacial heat fluxes over 90 W/cm^2 was achieved with a heat transfer coefficient of 1.8 W/cm^2K on a 50 μm thick membrane. Meanwhile, negative pressures as low as -300 kPa was demonstrated in the nanopores. An inverse proportional relationship between maximum interfacial heat fluxes and membrane thickness was obtained due to the limit in fluid transport. An approach to achieve heat fluxes over 1000 W/cm^2 was proposed by creating nanoporous membranes with thicknesses on the order of 1 μm.

To better understand the relation between heat transfer behavior and the liquid morphology, we developed a new metrology technique capable of measuring the transient heat transfer coefficient during evaporation processes. The micro/nanostructured test sample was first wetted by the coolant and subsequently heated by a series of pulses in contrast to a constant heat flux. By assuming a lumped system, the response of the sample is expected to be an exponential function. Accordingly, the time constant of the response indicated the transient heat transfer coefficient and heat capacity, which can be determined by curve fitting. Two sample systems were tested using this approach: surface oxidized copper microwires and nanoporous membranes. Combined with microscopic imaging, the heat transfer behavior was found to be dependent on the surface roughness of the copper microwires. Meanwhile, a clear peak in transient heat transfer coefficient was identified during the drying process of the nanoporous membrane, which corresponds to the thin film evaporation regime. This technique is valuable for the fundamental understanding of the correlation between wetting properties and phase change heat transfer performance.

On the superhydrophobic surfaces for enhanced condensation, three properties including small departure radius, low contact angle, and high nucleation densities are all desired but have yet to be achieved. To simultaneously achieve these three properties, we presented a new approach to enhance condensation heat transfer using oil-infused structured surfaces with heterogeneous surface chemistry. A heterogeneous coating consisting of scattered high-surface-energy sites on a low-surface-energy background was deposited on micro/nanostructured surfaces. The surfaces were then infused with oil, which is stabilized by the surface structuring. During condensation, nucleation occurred on the high-surface-energy sites immersed within the oil phase, but near the oil/vapor interface. In contrast to the same surface not infused with oil, nucleation densities were one order of magnitude larger due to the combined effect of the high-surface-energy sites and the reduced oil-water interfacial energy which lower the thermodynamic energy barrier for stable nuclei formation. Furthermore, the contact angle hysteresis was as low as 3° and the droplet apparent contact angle was ≈110°. This immersion condensation mode allows near-ideal condensation heat transfer performance. Accordingly, we experimentally demonstrated that the heat transfer coefficient can be enhanced by approximately 100% compared to a dropwise condensation surface in the presence of non-condensable gases (NCG). Thus, these surfaces promise the development of a scalable approach for highly efficient condensation heat transfer for industrial, building energy, electronics cooling, and water-harvesting applications.

7.2. Future Work

The effort in this thesis could be further extended in the future in three aspects.

First of all, we proposed a path to achieve heat fluxes over 1000 W/cm^2 by reducing membrane thickness to the order of 1 μm in the thesis. However, the mechanical strength of the aluminum oxide membranes used in the proof of concept experiment was too low to allow such small thicknesses. Moreover, the pore size of the aluminum oxide membranes was not uniform, which

increased the uncertainty of the heat flux. In the future, a silicon based porous memebrane is proposed to address these problems and demonstrate heat fluxes over 1000 W/cm^2. The fabrication process is shown in Fig. 7-1.

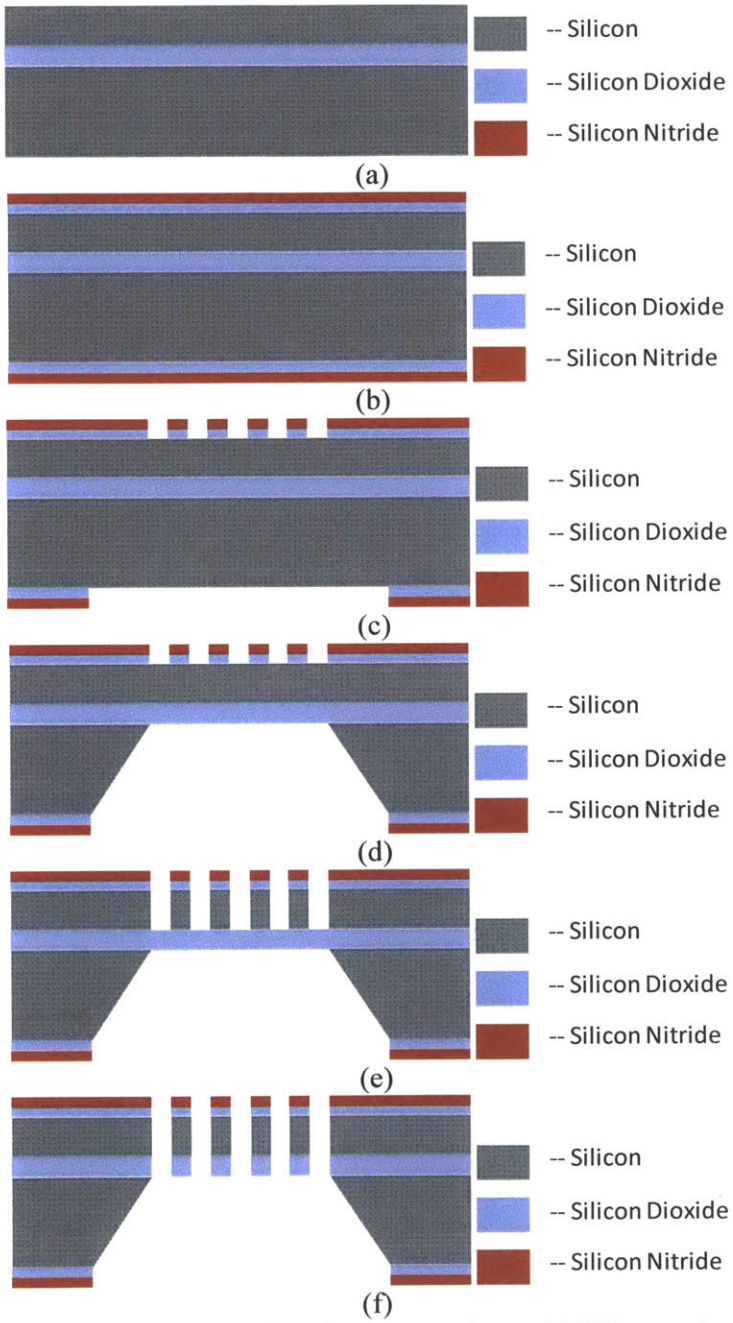

Fig. 7-1 Proposed fabrication process of silicon-based porous membrane. (a) Silicon on insulator (SOI) wafer. (b) Growth of silicon dioxide and silicon nitride on both sides of the wafer. (c) Lithrography and etch of silicon oxide and nitride to create the mask. (d) KOH wet etching of the back side of the wafer with front side protected. (e) Dry etching from front side to create pores. (f) Etch through oxide layer to finish the pores.

The fabrication process will start with a silicon on insulator (SOI) wafer. Silicon dioxide and silicon nitride will be grown on both sides of the wafer. Standard contact lithography and reactive ion etching processes will be used to fabricate desired features in the nitride and oxide layer. KOH wet etching will be performed at the backside of the wafer, after which dry etching will be performed at the frontside to open up micro to nanoscale pores. Finally, the insulator layer will be etched through. With the proposed process, micro to nanoscale pore arrays in silicon membrane can be created with uniform pore size and porosity. The thickness of the membrane can be conveniently controlled by controlling the thickness of the silicon layer ("device layer") on the front side of the SOI wafer. Commercially available SOI wafers have device layers with thicknesses ranging from 2-50 μm, which could well-satisfy our needs. The ridges on the backside of the wafer created by KOH etching serves as the supporting structure for the thin membrane.

For transient heat transfer coefficient measurements, a key component is the relationship between heat transfer coefficients and micro/nanoscale imaging to understand the correlation between fluid morphology and heat transfer behavior. Future work could involve using environmental scanning electron microscope (ESEM) for the imaging of the phase change process. For example, Miljkovic *et al.* have captured the liquid shape on a superhydrophilic nanopillar array, as shown in Fig. 7-2 [110]. It would be an interesting study to apply heat pulses to record the instantaneous heat transfer coefficients at the same time with imaging.

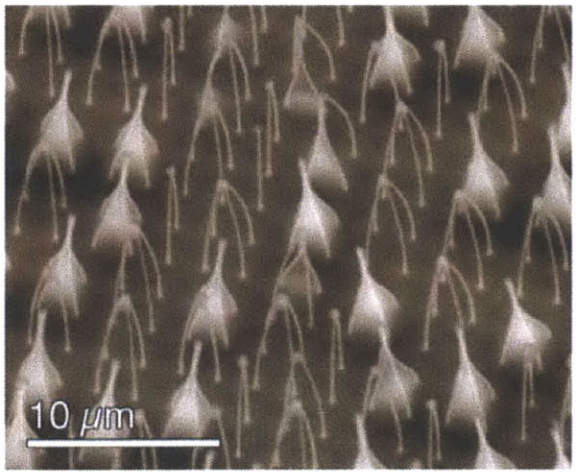

Fig. 7-2 ESEM image of liquid wetting a nanopillar array by Miljkovic *et al.*[110]

Finally, for the immersion condensation work on oil-infused surface, further work should be focused on tailoring oil and coating properties, as well as surface geometry. Ideally, the oil should have a lower surface tension such that it stays on the microstructured surface. Moreover, the viscosity of the oil needs to be low therefore as the water droplet grows, the oil coverage on the droplet could drain and breaks up, avoiding oil loss as water droplet is shed away from the surface. The diffusivity of water vapor in the oil should be as high as possible to allow easy diffusion through the oil coverage. For the surface structuring, the space between the structures

will not be useful for condensation. As a result, the structure density should be high to maximize the condensing area.

7.3. Broader Perspectives

Using micro/nanostructures to enhance phase change heat transfer has been an active area for a long time due to the significance in both practical applications and fundamental physics.

From a practical point of view, the power densities of electronic devices vary significantly depending on the applications. Mobile devices typically dissipate heat fluxes on the order of 10 W/cm^2, where weight, size and power consumption become the key issue. Complex phase change processes are not commonly used for such applications. Currently, commercial desktop computers usually require thermal management capability of 100 W/cm^2 which can be well addressed with traditional heat pipes. However, the development of next generation of power electronic devices would require heat fluxes over 1000 W/cm^2. Such high heat fluxes cannot be dissipated using single phase approaches and phase change processes becomes the only viable approach. As discussed in Chapter 1, a large variety of phase change processes have been previously studied with various limitations while thin film evaporation is the most promising avenue to overcome those limitations. The investigation of this thesis on thin film evaporation aimed at heat fluxes ~1000 W/cm^2.

From a fundamental point of view, the micro/nanostructuring could influence the phase change processes from two aspects: geometrical or physical. Most of the previous efforts in this area have been utilizing the geometrical and morphological effects where the fluid (liquid or vapor) is "independent" from the solid structures. The fluid has the same properties as without the structures. The surface structuring only acts as a geometrical confinement. Examples include reduced liquid film thickness which reduces the conduction resistance for evaporation, and smaller departure radius of droplets which reduces the conduction resistance for condensation. A significant portion of this thesis is also attributed to this aspect. However, the micro/nanostructures could influence the phase change behavior from another aspect involving more fundamental physics such as intermolecular interactions between solid and liquid due to the large surface to volume ratio at the nanoscale. The fluid properties are altered with the existence of the solid structures. There has been some works discussing such effects, such as specific heat and phase change point of fluid in nanoscale confinements [111, 112]. While these effects have great potential to drastically improve phase change processes, precise thermal measurement with high spatial resolution would be a prerequisite for detailed investigation, which has yet to be fully demonstrated.

References

1. Bico, J., U. Thiele, and D. Quéré, *Wetting of textured surfaces.* Colloids and Surfaces A: Physicochemical and Engineering Aspects, 2002. **206**(1–3): p. 41-46.
2. Cassie, A.B.D. and S. Baxter, *Wettability of porous surfaces.* Transactions of the Faraday Society, 1944. **40**: p. 0546-0550.
3. Wenzel, R.N., *RESISTANCE OF SOLID SURFACES TO WETTING BY WATER.* Industrial & Engineering Chemistry, 1936. **28**(8): p. 988-994.
4. Chu, K.H., R. Xiao, and E.N. Wang, *Uni-directional liquid spreading on asymmetric nanostructured surfaces.* Nature materials, 2010. **9**(5): p. 413-417.
5. Courbin, L., et al., *Imbibition by polygonal spreading on microdecorated surfaces.* Nature materials, 2007. **6**(9): p. 661-664.
6. Xiao, R., K.H. Chu, and E.N. Wang, *Multilayer liquid spreading on superhydrophilic nanostructured surfaces.* Applied Physics Letters, 2009. **94**(19): p. 193104-193104-3.
7. Ahuja, A., et al., *Nanonails: A simple geometrical approach to electrically tunable superlyophobic surfaces.* Langmuir, 2008. **24**(1): p. 9-14.
8. Tuteja, A., et al., *Robust omniphobic surfaces.* Proceedings of the National Academy of Sciences, 2008. **105**(47): p. 18200-18205.
9. Chiou, N.R., et al., *Growth and alignment of polyaniline nanofibres with superhydrophobic, superhydrophilic and other properties.* Nature Nanotechnology, 2007. **2**(6): p. 354-357.
10. Krupenkin, T.N., et al., *From rolling ball to complete wetting: the dynamic tuning of liquids on nanostructured surfaces.* Langmuir, 2004. **20**(10): p. 3824-3827.
11. Cebeci, F.Ç., et al., *Nanoporosity-driven superhydrophilicity: a means to create multifunctional antifogging coatings.* Langmuir, 2006. **22**(6): p. 2856-2862.
12. Garrod, R., et al., *Mimicking a stenocara beetle's back for microcondensation using plasmachemical patterned superhydrophobic-superhydrophilic surfaces.* Langmuir, 2007. **23**(2): p. 689-693.
13. Wang, J., et al., *Dewetting of conducting polymer inkjet droplets on patterned surfaces.* Nature materials, 2004. **3**(3): p. 171-176.
14. Extrand, C., et al., *Superwetting of structured surfaces.* Langmuir, 2007. **23**(17): p. 8882-8890.
15. Quéré, D., *Non-sticking drops.* Reports on Progress in Physics, 2005. **68**(11): p. 2495.
16. Wayner, P., Y. Kao, and L. LaCroix, *The interline heat-transfer coefficient of an evaporating wetting film.* International Journal of Heat and Mass Transfer, 1976. **19**(5): p. 487-492.
17. Wang, H., S.V. Garimella, and J.Y. Murthy, *Characteristics of an evaporating thin film in a microchannel.* International Journal of Heat and Mass Transfer, 2007. **50**(19): p. 3933-3942.
18. Cai, Q. and A. Bhunia, *High heat flux phase change on porous carbon nanotube structures.* International Journal of Heat and Mass Transfer, 2012.
19. Ćoso, D., et al., *Enhanced Heat Transfer in Biporous Wicks in the Thin Liquid Film Evaporation and Boiling Regimes.* Journal of Heat Transfer, 2012. **134**: p. 101501.
20. Kim, S. and K.J. Kim, *Dropwise Condensation Modeling Suitable for Superhydrophobic Surfaces.* Journal of Heat Transfer, 2011. **133**(8): p. 081502.
21. Le Fevre, E.J. and J.W. Rose, *An experimental study of heat transfer by dropwise condensation.* International Journal of Heat and Mass Transfer, 1965. **8**(8): p. 1117-1133.
22. O'Neill, G.A. and J.W. Westwater, *Dropwise condensation of steam on electroplated silver surfaces.* International Journal of Heat and Mass Transfer, 1984. **27**(9): p. 1539-1549.
23. Rose, J.W., *On the mechanism of dropwise condensation.* International Journal of Heat and Mass Transfer, 1967. **10**(6): p. 755-762.

24. Rose, J.W., *Dropwise condensation theory and experiment: A review.* Proceedings of the Institution of Mechanical Engineers, Part A: Journal of Power and Energy, 2002. **216**(2): p. 115-128.
25. Tanner, D.W., et al., *Heat transfer in dropwise condensation at low steam pressures in the absence and presence of non-condensable gas.* International Journal of Heat and Mass Transfer, 1968. **11**(2): p. 181-190.
26. Pop, E., *Energy dissipation and transport in nanoscale devices.* Nano Research, 2010. **3**(3): p. 147-169.
27. *International Technology Roadmap for Semiconductors, 2009 edn.* Executive Summary. Semiconductor Industry Association, 2009.
28. Thome, J.R., *The new frontier in heat transfer: Microscale and nanoscale technologies.* 2006.
29. Krishnan, S., et al., *Towards a thermal Moore's law.* Advanced Packaging, IEEE Transactions on, 2007. **30**(3): p. 462-474.
30. Dhir, V. and S. Liaw, *Framework a for unified model for nucleate and transition pool boiling.* Journal of Heat Transfer;(USA), 1989. **111**(3).
31. Liter, S.G. and M. Kaviany, *Pool-boiling CHF enhancement by modulated porous-layer coating: theory and experiment.* International Journal of Heat and Mass Transfer, 2001. **44**(22): p. 4287-4311.
32. Kandlikar, S.G., *A theoretical model to predict pool boiling CHF incorporating effects of contact angle and orientation.* TRANSACTIONS-AMERICAN SOCIETY OF MECHANICAL ENGINEERS JOURNAL OF HEAT TRANSFER, 2001. **123**(6): p. 1071-1079.
33. Chen, R., et al., *Nanowires for enhanced boiling heat transfer.* Nano Letters, 2009. **9**(2): p. 548-553.
34. Chu, K.H., R. Enright, and E.N. Wang, *Structured surfaces for enhanced pool boiling heat transfer.* Applied Physics Letters, 2012. **100**(24): p. 241603-241603-4.
35. Forrest, E., et al., *Augmentation of nucleate boiling heat transfer and critical heat flux using nanoparticle thin-film coatings.* International Journal of Heat and Mass Transfer, 2010. **53**(1): p. 58-67.
36. Buongiorno, J., L.W. Hu, and B.H. Truong, *Determination of pool boiling critical heat flux enhancement in nanofluids*. 2007, Massachusetts Institute of Technology.
37. Kosar, A., C.J. Kuo, and Y. Peles, *Suppression of boiling flow oscillations in parallel microchannels by inlet restrictors.* Journal of Heat Transfer-Transactions of the Asme, 2006. **128**(3): p. 251-260.
38. Mudawar, I., *Assessment of high-heat-flux thermal management schemes.* Components and Packaging Technologies, IEEE Transactions on, 2001. **24**(2): p. 122-141.
39. Wang, E.N., et al., *Micromachined jets for liquid impingement cooling of VLSI chips.* Microelectromechanical Systems, Journal of, 2004. **13**(5): p. 833-842.
40. Lin, L. and R. Ponnappan, *Heat transfer characteristics of spray cooling in a closed loop.* International Journal of Heat and Mass Transfer, 2003. **46**(20): p. 3737-3746.
41. Bash, C.E., C.D. Patel, and R.K. Sharma. *Inkjet assisted spray cooling of electronics*. in *International Electronic Packaging Technical Conference and Exhibition (IPACK), Maui, Hawaii*. 2003.
42. Hall, D.D. and I. Mudawar, *Experimental and numerical study of quenching complex-shaped metallic alloys with multiple, overlapping sprays.* International Journal of Heat and Mass Transfer, 1995. **38**(7): p. 1201-1216.
43. Park, K., K.J. Noh, and K.S. Lee, *Transport phenomena in the thin-film region of a micro-channel.* International Journal of Heat and Mass Transfer, 2003. **46**(13): p. 2381-2388.
44. Stephan, P. and C. Busse, *Analysis of the heat transfer coefficient of grooved heat pipe evaporator walls.* International Journal of Heat and Mass Transfer, 1992. **35**(2): p. 383-391.

45. Jiao, A., H. Ma, and J. Critser, *Evaporation heat transfer characteristics of a grooved heat pipe with micro-trapezoidal grooves.* International Journal of Heat and Mass Transfer, 2007. **50**(15): p. 2905-2911.
46. Wong, S.C., J.H. Liou, and C.W. Chang, *Evaporation resistance measurement with visualization for sintered copper-powder evaporator in operating flat-plate heat pipes.* International Journal of Heat and Mass Transfer, 2010. **53**(19): p. 3792-3798.
47. Weibel, J.A., et al., *Design of integrated nanostructured wicks for high-performance vapor chambers.* Components, Packaging and Manufacturing Technology, IEEE Transactions on, 2011. **1**(6): p. 859-867.
48. Ding, C., et al., *A Flat Heat Pipe Architecture Based on Nanostructured Titania.* Microelectromechanical Systems, Journal of, 2010. **19**(4): p. 878-884.
49. Nam, Y., et al., *Characterization and modeling of the heat transfer performance of nanostructured Cu micropost wicks.* Journal of Heat Transfer, 2011. **133**(10).
50. Kim, S.S., et al. *Thermal Performance of Carbon Nanotube Enhanced Vapor Chamber Wicks*. 2010: ASME.
51. Hwang, G.S., et al., *Multi-artery heat pipe spreader: Experiment.* International Journal of Heat and Mass Transfer, 2010. **53**(13–14): p. 2662-2669.
52. Cai, Q. and C.-L. Chen, *Design and Test of Carbon Nanotube Biwick Structure for High-Heat-Flux Phase Change Heat Transfer.* Journal of Heat Transfer, 2010. **132**(5): p. 052403-8.
53. Pérez-Lombard, L., J. Ortiz, and C. Pout, *A review on buildings energy consumption information.* Energy and Buildings, 2008. **40**(3): p. 394-398.
54. Beér, J.M., *High efficiency electric power generation: The environmental role.* Progress in Energy and Combustion Science, 2007. **33**(2): p. 107-134.
55. Khawaji, A.D., I.K. Kutubkhanah, and J.-M. Wie, *Advances in seawater desalination technologies.* Desalination, 2008. **221**(1–3): p. 47-69.
56. Schmidt, E., W. Schurig, and W. Sellschopp, *Versuche über die Kondensation von Wasserdampf in Film- und Tropfenform.* Forschung im Ingenieurwesen, 1930. **1**(2): p. 53-63.
57. Tanner, D.W., et al., *Heat transfer in dropwise condensation—Part I The effects of heat flux, steam velocity and non-condensable gas concentration.* International Journal of Heat and Mass Transfer, 1965. **8**(3): p. 419-426.
58. Chen, C.-H., et al., *Dropwise condensation on superhydrophobic surfaces with two-tier roughness.* Applied Physics Letters, 2007. **90**(17): p. 173108-3.
59. Boreyko, J.B. and C.-H. Chen, *Self-Propelled Dropwise Condensate on Superhydrophobic Surfaces.* Physical Review Letters, 2009. **103**(18): p. 184501.
60. Miljkovic, N., et al., *Jumping-Droplet-Enhanced Condensation on Scalable Superhydrophobic Nanostructured Surfaces.* Submitted, 2012.
61. Miljkovic, N., R. Enright, and E.N. Wang, *Effect of Droplet Morphology on Growth Dynamics and Heat Transfer during Condensation on Superhydrophobic Nanostructured Surfaces.* Acs Nano, 2012. **6**(2): p. 1776-1785.
62. Anand, S., et al., *Enhanced Condensation on Lubricant Impregnated Nanotextured Surfaces.* Acs Nano, 2012.
63. Wong, T.-S., et al., *Bioinspired self-repairing slippery surfaces with pressure-stable omniphobicity.* Nature, 2011. **477**(7365): p. 443-447.
64. Washburn, E.W., *The dynamics of capillary flow.* Physical Review, 1921. **17**(3): p. 273.
65. Nam, Y., et al., *Fabrication and characterization of the capillary performance of superhydrophilic Cu micropost arrays.* Microelectromechanical Systems, Journal of, 2010. **19**(3): p. 581-588.
66. Hasimoto, H., *On the periodic fundamental solutions of the Stokes equations and their application to viscous flow past a cubic array of spheres.* J. Fluid Mech, 1959. **5**(02): p. 317-328.

67. Sangani, A. and A. Acrivos, *Slow flow past periodic arrays of cylinders with application to heat transfer.* International Journal of Multiphase Flow, 1982. **8**(3): p. 193-206.
68. Srivastava, N., et al., *A unified scaling model for flow through a lattice of microfabricated posts.* Lab on a Chip, 2010. **10**(9): p. 1148-1152.
69. Ishino, C., et al., *Wicking within forests of micropillars.* EPL (Europhysics Letters), 2007. **79**(5): p. 56005.
70. Brinkman, H., *A calculation of the viscous force exerted by a flowing fluid on a dense swarm of particles.* Applied Scientific Research, 1949. **1**(1): p. 27-34.
71. Xiao, R., R. Enright, and E.N. Wang, *Prediction and Optimization of Liquid Propagation in Micropillar Arrays.* Langmuir, 2010. **26**(19): p. 15070-15075.
72. Xiao, R. and E.N. Wang, *Microscale Liquid Dynamics and the Effect on Macroscale Propagation in Pillar Arrays.* Langmuir, 2011. **27**(17): p. 10360-10364.
73. Buckingham, E., *On physically similar systems; illustrations of the use of dimensional equations.* Physical Review, 1914. **4**(4): p. 345-376.
74. Sbragaglia, M., et al., *Spontaneous breakdown of superhydrophobicity.* Physical Review Letters, 2007. **99**(15): p. 156001.
75. Pirat, C., et al., *Multiple time scale dynamics in the breakdown of superhydrophobicity.* EPL (Europhysics Letters), 2008. **81**(6): p. 66002.
76. Tanner, L.H., *The spreading of silicone oil drops on horizontal surfaces.* Journal of Physics D: Applied Physics, 1979. **12**(9): p. 1473.
77. Srivastava, N., et al., *A unified scaling model for flow through a lattice of microfabricated posts.* Lab on a Chip, 2010. **10**: p. 1148-1152.
78. Mills, A.F., *Heat and Mass Transfer*. 2 ed. 1999: Prentice-Hall.
79. Wheeler, T.D. and A.D. Stroock, *The transpiration of water at negative pressures in a synthetic tree.* Nature, 2008. **455**(7210): p. 208-212.
80. Carey, V.P., *Liquid-Vapor Phase-Change Phenomena*. 1992: Hemisphere Pub. Corp.
81. Paul, B., *Compilation of Evaporation Coefficients.* American Rocket Society Journal, 1962. **32**: p. 1321.
82. Zhang, T.J., et al., *Two-phase refrigerant flow instability analysis and active control in transient electronics cooling systems.* International Journal of Multiphase Flow, 2011. **37**(1): p. 84-97.
83. Shou-Shing, H. and L. Chih-Yi, *Subcooled convective boiling in structured surface microchannels.* Journal of Micromechanics and Microengineering, 2010. **20**(1): p. 015027.
84. Peles, Y., *Two-phase boiling flow in microchannels - Instabilities issues and flow regime mapping.* First International Conference on Microchannels and Minichannels, 2003: p. 559-566.
85. Kandlikar, S.G. and A.V. Bapat, *Evaluation of jet impingement, spray and microchannel chip cooling options for high heat flux removal.* Heat Transfer Engineering, 2007. **28**(11): p. 911-923.
86. Browne, E.A., et al., *Microjet array single-phase and flow boiling heat transfer with R134a.* International Journal of Heat and Mass Transfer, 2010. **53**(23-24): p. 5027-5034.
87. Jiao, A.J., H.B. Ma, and J.K. Critser, *Evaporation heat transfer characteristics of a grooved heat pipe with micro-trapezoidal grooves.* International Journal of Heat and Mass Transfer, 2007. **50**(15–16): p. 2905-2911.
88. Ranjan, R., J.Y. Murthy, and S.V. Garimella, *A microscale model for thin-film evaporation in capillary wick structures.* International Journal of Heat and Mass Transfer, 2011. **54**(1): p. 169-179.
89. Migliaccio, C., H. Dhavaleswarapu, and S. Garimella. *Microscale Temperature Measurements Near the Contact Line of an Evaporating Thin Film in a V-Groove*. 2009: ASME.
90. Dhavaleswarapu, H.K., et al., *Experimental investigation of evaporation from low-contact-angle sessile droplets.* Langmuir, 2009. **26**(2): p. 880-888.

91. Nam, Y. and Y.S. Ju, *Comparative Study of Copper Oxidation Schemes and Their Effects on Surface Wettability.* ASME Conference Proceedings, 2008. **2008**(48715): p. 1833-1838.
92. Daniel, S., M.K. Chaudhury, and J.C. Chen, *Fast Drop Movements Resulting from the Phase Change on a Gradient Surface.* Science, 2001. **291**(5504): p. 633-636.
93. Kashchiev., D., *Nucleation: Basic Theory with Applications*. 1 ed. 2000: Oxford: Butterworth-Heinemann.
94. Bunker, B.C., et al., *The Impact of Solution Agglomeration on the Deposition of Self-Assembled Monolayers.* Langmuir, 2000. **16**(20): p. 7742-7751.
95. Guo, L.J., X. Cheng, and C.-F. Chou, *Fabrication of Size-Controllable Nanofluidic Channels by Nanoimprinting and Its Application for DNA Stretching.* Nano Letters, 2003. **4**(1): p. 69-73.
96. Park, M., et al., *Block Copolymer Lithography: Periodic Arrays of ~1011 Holes in 1 Square Centimeter.* Science, 1997. **276**(5317): p. 1401-1404.
97. James, P.J., et al., *Interpretation of Contrast in Tapping Mode AFM and Shear Force Microscopy. A Study of Nafion.* Langmuir, 2000. **17**(2): p. 349-360.
98. Raj, R., et al., *A Unified Model for Contact Angle Hysteresis on Heterogeneous and Superhydrophobic Surfaces.* Langmuir, 2012(Submitted).
99. Dimitrakopoulos, P. and J.J.L. Higdon, *On the gravitational displacement of three-dimensional fluid droplets from inclined solid surfaces.* Journal of Fluid Mechanics, 1999. **395**: p. 181-209.
100. Pound, G.M., M.T. Simnad, and L. Yang, *Heterogeneous Nucleation of Crystals from Vapor.* The Journal of Chemical Physics, 1954. **22**(7): p. 1215-1219.
101. Sigsbee, R.A., *Adatom Capture and Growth Rates of Nuclei.* Journal of Applied Physics, 1971. **42**(10): p. 3904-3915.
102. Pocker, D.J. and S.J. Hruska, *Detailed Calculations of the Number of Distinct Sites Visited in Random Walk on Several Two-Dimensional Substrate Lattices.* Journal of Vacuum Science and Technology, 1971. **8**(6): p. 700-707.
103. J.P.Hirth and G.M.Pound, *Condensation and evaporation - nucleation and growth kinetics* 1963: England: Pergamon Press.
104. Thiel, P.A. and T.E. Madey, *The interaction of water with solid surfaces: Fundamental aspects.* Surface Science Reports, 1987. **7**(6–8): p. 211-385.
105. Israelachvili, J.N., *Intermolecular and surface forces*. 2nd ed. 1991, Amsterdam: Academic Press.
106. Ma, Y., A.S. Foster, and R.M. Nieminen, *Reactions and clustering of water with silica surface.* The Journal of Chemical Physics, 2005. **122**(14): p. 144709-9.
107. Gupta, M. and K.K. Gleason, *Initiated Chemical Vapor Deposition of Poly(1H,1H,2H,2H-perfluorodecyl Acrylate) Thin Films.* Langmuir, 2006. **22**(24): p. 10047-10052.
108. Enright, R., et al., *Condensation on Superhydrophobic Copper Oxide Nanostructures.* 3rd Micro/Nanoscale Heat & Mass Transfer International Conference, 2012.
109. Nam, Y. and Y.S. Ju, *Comparative Study of Copper Oxidation Schemes and Their Effects on Surface Wettability.* Imece 2008: Heat Transfer, Fluid Flows, and Thermal Systems, Vol 10, Pts a-C, 2009: p. 1833-1838.
110. Miljkovic, N., et al., *Liquid Evaporation on Superhydrophobic and Superhydrophilic Nanostructured Surfaces.* Journal of Heat Transfer, 2011. **133**(8): p. 080903.
111. Shin, D. and D. Banerjee, *Enhancement of specific heat capacity of high-temperature silica-nanofluids synthesized in alkali chloride salt eutectics for solar thermal-energy storage applications.* International Journal of Heat and Mass Transfer, 2011. **54**(5): p. 1064-1070.
112. Morishige, K., H. Yasunaga, and Y. Matsutani, *Effect of Pore Shape on Freezing and Melting Temperatures of Water.* The Journal of Physical Chemistry C, 2010. **114**(9): p. 4028-4035.